An x-ray spectroscopic study of novel materials for electronic applications

by Michael Räkers

Thesis
presented to the
Department of Physics
University of Osnabrück

Osnabrück
April 2009

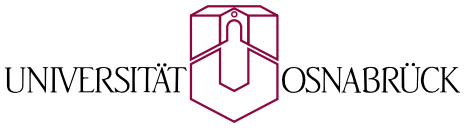

Thesis advisor:
apl. Prof. Prof. h.c. Dr. Dr. h.c. Manfred Neumann

Contents

List of Figures

List of Tables

Introduction

The fast progress in the field of advanced electronics, like data storage devices, is based on the intensive research on materials with special electronic and magnetic properties. Furthermore, the increasing storage density of magnetic storage devices reaches the superparamagnetic limit, where a too small cluster cannot maintain its magnetization. It is necessary to investigate new materials with better or novel properties, to describe the origins of such properties and to characterize the latter so that for for each specific application the most suitable material will be found. With this knowledge new materials can be designed which have special desired properties.

In this work several materials are investigated showing different important effects. The *Giant Magnetoresistance* effect (GMR) was applied at the end of the last decade in read heads for hard drives, resulting in a huge increase of the storage density because of the possibility to build very small read heads. The even bigger *Colossal Magnetoresistance* (CMR) effect was found in manganese oxides like $La_{1-x}Sr_xMnO_3$. Therefore the superparamagnetic limit (today ~ 200 Gbit/in^2) will become the limiting factor for further increase of storage density. New materials and structures, such as nanodots of $La_{1-x}Sr_xMnO_3$, are supposed to push the superparamagnetic limit further to higher densities.

The continuous growing of storage density of random access memory (RAM) devices is due to miniaturization of transistors which nowadays reaches its limit for the traditional gate dielectric SiO_2. With new high-k materials, like rare earth scandates ($REScO_3$), the leakage current through the transistors can be minimized and the miniaturization limit of silicates is lifted. Another application of these materials is the usage as substrates to induce strains in thin films resulting for example in higher transition temperatures of ferroelectric materials like $BaTiO_3$.

Materials which are at the same time ferroelectric and ferromagnetic are called multiferroics. In this materials an electromagnetic coupling can be used to realize the next generation of storage devices by multiferroic data storage. Voltages can be used to store data instead of currents. This might solve cooling problems of miniaturized devices. A promising candidate for such applications is $LuFe_2O_4$.

In the present work the electronic structure and the magnetic properties of $La_{1-x}Sr_xMnO_3$, $REScO_3$ and $LuFe_2O_4$ are investigated by means of x-ray spectroscopies. This work is structured as follows:

- In Chapter 1, the state of the art in the fields of CMR, high-k, strain tailoring and multiferroic materials is given with special attention to the investigated materials.
- In Chapter 2, Basics of X-ray Spectroscopy, the theoretical and experimental

methods of different x-ray spectroscopic techniques are described. Some important effects and interactions are explained additionally.

- In the following part, Chapter 3, the experimental results for the CMR material $La_{1-x}Sr_xMnO_3$ are presented. The total magnetic moment is compared with partial magnetic moments at the manganese site which is separated in magnetic spin and orbital moment.

- Chapter 4 comprises a complete investigation of the electronic structure of occupied and unoccupied states of $REScO_3$ (RE = Sm, Gd, Dy). The resulting band gaps for this compounds and additionally for $NdScO_3$ and $TbScO_3$ are compared with structural properties.

- In Chapter 5, the electronic structure of the occupied and unoccupied states of $LuFe_2O_4$ is presented. Additionally the magnetic spin and orbital moments are compared with the spin arrangement of iron ions and the total magnetic moment.

- The last part, Summary and Outlook, comprises the results of the present work and gives a short outlook to further investigations.

Chapter 1

State of the Art

In this chapter the state of the art in the field of magneto resistance compounds, high–k materials, strain tailoring and multiferroics is given. (Rare earth) transition metal oxides gained an enormous interest in these fields. The transition metal $3d$ states play a key role for these different physical effects.

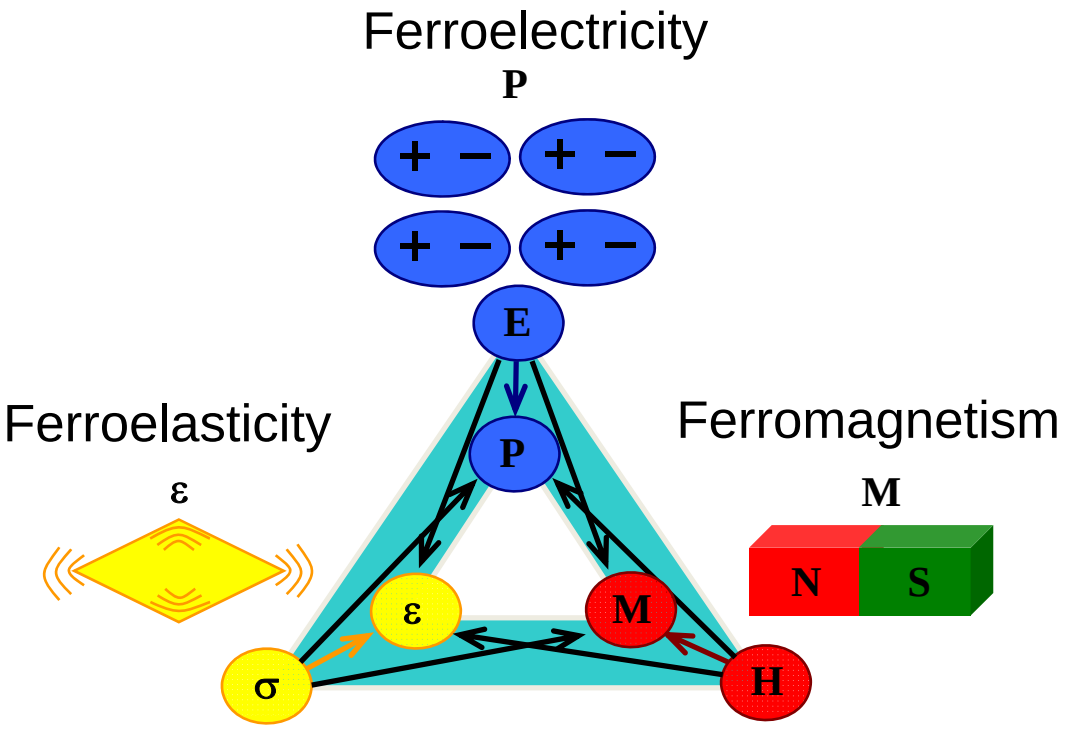

Figure 1.1: Scheme of the interplay of ferroelectricity, ferromagnetism and ferroelasticity.

The competition between magnetic, electric and structural properties can lead to enormous changes of the physical properties. These changes often take place close to the phase transition temperatures. A schematic plot of the interplay between the physical properties is shown in figure 1.1. Physical pressure can induce strain to a

structure, which can influence also magnetic or electric properties. An example for this mechanism is the Piezo effect, where electric voltage is induced to a crystal by physical pressure. This effect works also in the opposite direction, when an applied voltage changes the structure (length) of a crystal. This is an example where an electric field polarizes a sample with influence on the structure (electrostriction). Structural changes can also lead to magnetic ordering. Magnetic phase transitions are usually accompanied by structural phase transitions. In electromagnetic multiferroics the magnetization can be influenced by the electric polarization and vice versa. These all are just some examples for the coupling of structural, electronic and magnetic properties.

Now we want to turn to the effects appearing in advanced materials which are examined in the present work. The colossal magnetoresistance appearing in manganites, like $La_{1-x}Sr_xMnO_3$, is associated with half metallic ferromagnetism, where one spin channel is metallic and the other spin channel is insulating (Pickett and Moodera, 2001; Park *et al.*, 1998). This magnetic behaviour is strongly correlated to the structure of this compounds. One of the most famous ferroelectric materials is $BaTiO_3$ where the ferroelectric transition temperature is below 200 K for single crystals. In thin films of $BaTiO_3$ prepared on substrates like rare earth scandates, strains are induced due to a mismatch of the lattice parameters. These strains can lead to an enhancement of the ferroelectric transition temperature of more than 600 K (Choi *et al.*, 2004). A similar effect was found for $SrTiO_3$ thin films (Haeni *et al.*, 2004). The rare earth scandates are also promising candidates for the next generation semiconductor components to replace the SiO_2 gate dielectric due to their high dielectric constant and thin film properties in contact with silicon (Kim *et al.*, 2006). In magnetoelectric multiferroics like $LuFe_2O_4$, the interplay between magnetic and electric properties is very interesting for future applications in microelectronics. This material exhibits giant room temperature magnetodielectric response (Subramanian *et al.*, 2006). Nowadays the magnetic storage devices are switched by electric currents which can be accompanied by a critical heating of the device. In multiferroic materials one might switch the magnetic state by an applied electric field which would result in a reduction of the heat production.

In the following sections the state of the art for colossal magneto resistance compounds ($La_{1-x}Sr_xMnO_3$), high–k and strain tailoring materials ($REScO_3$) and multiferroics ($LuFe_2O_4$) is sketched.

1.1 Colossal Magneto Resistance Compounds

Colossal Magneto Resistance (CMR) at room temperature was firstly investigated by von Helmolt *et al.* (1993) in perovskite-like $La_{2/3}Ba_{1/3}MnO_x$ ferromagnetic films. A huge negative change in the electrical resistance was induced by an applied magnetic field. This effect can be used in applications like magnetic sensors, magnetic storage devices and spin electronics. The Giant Magneto Resistance (GMR) effect, which is smaller than the CMR effect, is already used in read heads of modern hard discs. Peter Grünberg and Albert Fert gained the Nobel price 2007 in physics for the discovery of the GMR effect. Because of the reduction of the read head size,

the limiting factor of the increase of storage density will become the superparamagnetic limit (today $\sim$ 200Gbit/in^2), which can be pushed to higher density by use of new materials and structures, such as Nanodots of $La_{1-x}Sr_xMnO_3$ (Ruzmetov *et al.*, 2005). Another application is the field of spinelectronics, where $La_{1-x}Sr_xMnO_3$ is a promising candidate for ferromagnetic layers in magnetic tunnel junctions and other spin–injection devices, since it has nearly 100% spin polarization and a high Curie temperature $T_C \approx 350$ K (Park *et al.*, 1998; Bowen *et al.*, 2003).

Hole doped manganese oxides in the perovskite structure, $R_{1-x}A_xMnO_3$, where R and A represent a trivalent rare earth ion and a divalent ion, respectively, show a very rich phase diagram as a function of temperature, magnetic field and doping. An example for such a phase diagram is given by Dabrowski *et al.* (1999) for $La_{1-x}Sr_xMnO_3$ ($0.1 \leq x \leq 0.2$). The resulting phase diagram is presented in figure 1.2, in which transitions found by magnetic measurements are displayed by circles and transitions found by resistivity measurements are displayed by triangles and crosses. This variety of phases is due to competing structural, magnetic and

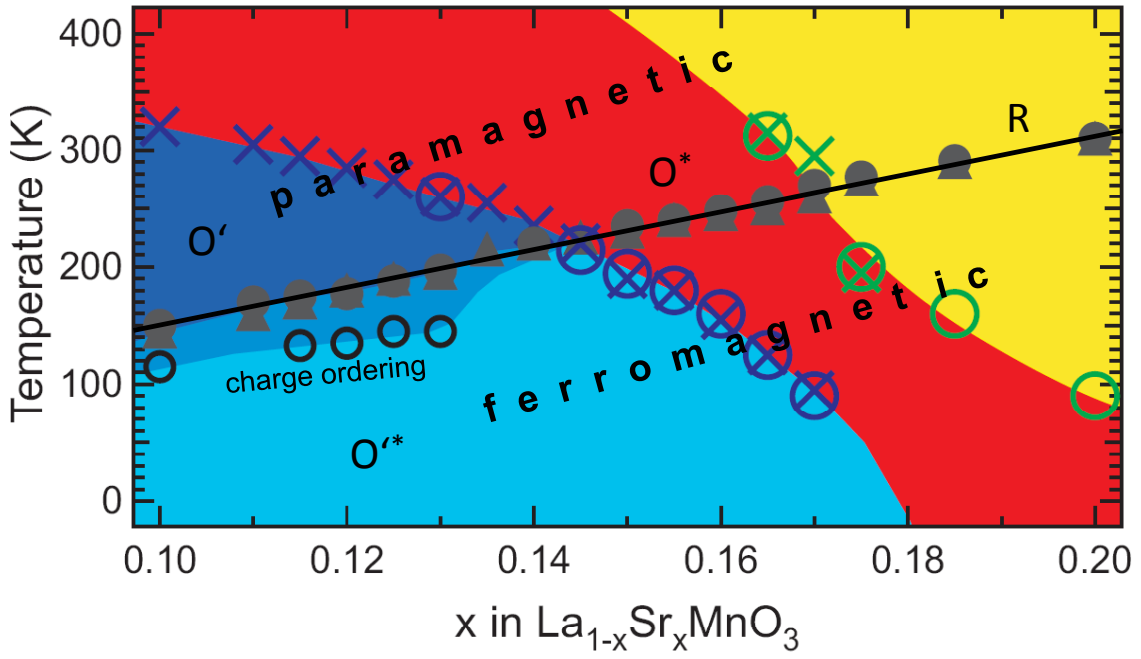

Figure 1.2: Phase diagram of $La_{1-x}Sr_xMnO_3$ ($0.1 \leq x \leq 0.2$) based on results from Dabrowski *et al.* (1999) with different structural transitions: orthorhombic phase with small coherent Jahn-Teller distortion (O*: red), with large coherent Jahn-Teller distortion (O': dark blue) and suppressed coherent Jahn-Teller distortion (O'*: light blue) and rhombohedral phase (R: yellow).

electric properties. The behaviour of the Mn 3*d* electrons is influenced by the structure when the occupation of different orbitals is preferred due to the distortion of the oxygen octahedron (Jahn-Teller distortion). This leads to an orbital ordering which was investigated in $La_{7/8}Sr_{1/8}MnO_3$ by Kuepper *et al.* (2005). A comparable ordering was found in the layered manganite $La_{0.5}Sr_{1.5}MnO_4$ by Huang *et al.* (2004). Tebano

et al. (2008) found orbital ordering at interfaces in ultrathin $La_{0.67}Sr_{0.33}MnO_3$ films suppressing the double exchange mechanism. A very recent publication by Li *et al.* (2009) investigated the crystal and magnetic structure of $La_{7/8}Sr_{1/8}MnO_3$. They found a breathing–mode distortion, which is a sign for a very strong cooperative Jahn–Teller distortion. Furthermore the magnetization direction turned for temperatures above ~ 100 K from the b to the c axis in the crystallographic $b-c$ plane. The mother compound $LaMnO_3$ is an antiferromagnetic insulator with $t_{2g}^3 e_g^1$ configuration of Mn^{3+} ions. The occupied e_g orbitals, $d_{3x^2-r^2}$ or $d_{3y^2-r^2}$, order alternating in the (001) plane. Such an ordering produces ferromagnetic ordering within the (001) plane and antiferromagnetic coupling along the c-axis (a-type antiferromagnetic). Collective Jahn-Teller distortions are influenced by this orbital ordering found by Kanamori (1959), which transforms the compound to a ferromagnetic insulator with Sr substitution at $x \approx 0.1$ and further on to a ferromagnetic metal at $x \approx 0.16$ (Urushibara *et al.*, 1995; Kawano *et al.*, 1996; Zhou *et al.*, 1997; Moritomo *et al.*, 1997). In the ferromagnetic insulating phase the double exchange carrier is subject to Anderson localization, resulting in the absence of diffusion of waves in random media. The Curie temperature increases with Sr substitution from $\sim$150 K for $x \approx 0.1$ to $\sim$300 K for $x \approx 0.2$ (Dabrowski *et al.*, 1999). Other atoms were substituted at the A-site with comparable effects, like $La_{1-x}Ca_xMnO_3$ (van Aken *et al.*, 2003). Also the B-site was substituted for $La_{0.6}Sr_{0.4}MnO_3$ with different metal ions (Li^{1+}, Mg^{2+}, Al^{3+}, Ti^{4+}, Nb^{5+}, Mo^{6+} and W^{6+}) by Vijayanandhini and Kutty (2008) resulting in lower transition temperatures, different magnetotransport properties and charge stripe ordering.

Despite the intense investigation of the CMR oxides, the mechanism of CMR is still not completely understood. A qualitatively correct description of the effect is given by the double exchange model of Zener (1951). This model alone, however, cannot account for the large magneto resistance (Millis *et al.*, 1995, 1996). Theoretical and experimental approaches suggest a more complex mechanism like short range ordered Jahn-Teller distortion in the local environment of the magnetic atom resulting in electron localization and polaron formation (Millis *et al.*, 1995, 1996; De Teresa *et al.*, 1997; Booth *et al.*, 1998; Louca *et al.*, 1997), charge and orbital ordering (Murakami *et al.*, 1998a,b) and phase separation (Moreo *et al.*, 1999; Mathur and Littlewood, 2003). The Jahn-Teller coupling energy is large ($\sim$1 eV; Imada *et al.* (1998)) while the exchange splitting of the conduction band depends on Sr doping and ranges from $\sim$1.7 eV ($x = 0.175$) to $\sim$0.9 eV ($x = 0.3$; Okimoto *et al.* (1997)).

1.2 High-k Materials

The rapid progress of complementary metal-oxide-semiconductor (CMOS) integrated circuit technology since the late 1980s has enabled the Si-based microelectronics industry to simultaneously meet several technological requirements to fulfil market expansion. These requirements comprise performance (speed), low static (off-state) power, and a wide range of power supply and output voltages. Additionally the scaling of the circuit takes place, which is the ability to perform a calculated reduction of the dimensions of the fundamental active device in the circuit, the *field effect transistor* (FET). The result has been a dramatic expansion in technology and

communications markets including the market associated with high performance microprocessors as well as low static-power applications, such as wireless systems (Wilk *et al.*, 2001).

The key element, which enables the scaling of the Si-based metal-oxide-semiconductor field effect transistor (MOSFET), is the material and the resulting electrical properties associated with the dielectric silicon dioxide, which is employed to isolate the transistor gate from the Si channel in CMOS devices. The use of amorphous, thermally grown SiO_2 as a gate dielectric offers several key advantages for CMOS processing. Two of these advantages are a stable (thermodynamically and electrically), high-quality Si-SiO_2 interface and superior electrical isolation properties. In modern CMOS processing, defect charge densities are in the order of $10^{10}/cm^2$, midgap interface state densities are $\approx 10^{10}/cm^2$ eV, and hard breakdown fields of 15 MV/cm are usually reached and are also therefore expected for devices with smaller dimensions (Wilk *et al.*, 2001). These challenging electrical properties have to be met by any alternative gate dielectric candidate.

It is essential to distinguish between the requirements for memory and transistor applications.

Memory capacitors require extremely low leakage currents ($J < 10^{-8}$ A/cm^2) and very high capacitance density for charge storage, but the interface quality is not that critical. Memory capacitor applications require control of the interface, primarily to limit interfacial reactions to keep the total capacitance high. The main requirement is that the capacitors store charge while current transport along the dielectric interface is not important. Furthermore electric field penetration is not required below the bottom electrode. Therefore the bottom electrode is often metal or nitrided poly-Si (heavily doped). All of the requirements lead to the important difference between memory capacitor and transistor application of high–k materials that the bottom dielectric interface quality is not as critical for capacitor performance.

In contrast, a key requirement of a FET is that the electric field penetrates into the Si channel to modulate carrier transport, and that the dielectric channel interface is of very high quality. The channel is used to be Si, so any potential high-k dielectric must be compatible with Si. Transistors have more forgiving leakage requirements ($< 10^2$ A/cm^2 for high-performance processors, and $\approx 10^3$ A/cm^2 for low–power applications), although high capacitance densities are still needed. The most critical distinction between high-k materials requirements for capacitors versus gate dielectrics is the interface and materials compatibility: gate dielectrics must form an extremely high-quality interface with Si, and also be able to withstand CMOS processing conditions while in contact (or near contact) with Si.

1.2.1 Memory Capacitor Applications

In the end of the 20th century, many of the materials initially chosen as potential alternative gate dielectric candidates were inspired by memory capacitor applications and the resultant semiconductor manufacturing tool development infrastructure (Wilk *et al.*, 2001).

Intensively studied high-k gate dielectric materials are systems such as Ta_2O_5

(Nishioka *et al.*, 1987; Chaneliere *et al.*, 1998; Fleming *et al.*, 2000), $SrTiO_3$ (McKee *et al.*, 1998; Yu *et al.*, 1999; Eisenbeiser *et al.*, 2000; Yu *et al.*, 2000a,b), and Al_2O_3 (Klein *et al.*, 1999; Gusev *et al.*, 2000; Kolodzey *et al.*, 1997; Michaelson, 1977). Their dielectric constants are in the range from 10 to 80. With the exception of Al_2O_3, these materials are not thermodynamically stable in direct contact with Si. This thermodynamic stability is not a requirement for memory capacitors because the dielectric is in contact with the electrodes, which are typically nitrided poly-Si or metal.

Interfacial reaction was observed for the case of Ta_2O_5 on Si (Alers *et al.*, 1998), as is expected from thermodynamic arguments and in agreement with previous work in dynamic random-access-memory capacitor applications (Nishioka *et al.*, 1987). This work reveals that the modification of the gate electrode and the channel interfaces is required reduce the reaction between adjacent phases. Interface engineering schemes have been developed to form oxynitrides and oxide/nitride reaction barriers between the high-k metal oxide material and Si to minimize the reaction with the underlying Si. Additionally to the reduction of reaction between the high-k dielectric and Si, these barrier layers help to maintain a high channel carrier mobility. However, it should be noted that an interfacial layer of SiO_2 or another low permittivity material limits the highest possible gate stack capacitance, which is equivalent to the limiting of the lowest achievable oxide thickness with respect to the dielectric constant. Furthermore the increased process complexity of the deposition and control of additional ultrathin dielectric layers, as well as scalability to later technology nodes, become more problematic.

This effect of reduced capacitance can be seen when the structure contains several dielectrics in series, the lowest capacitance layer will dominate the overall capacitance and sets a limit on the minimum achievable oxide thickness with respect to the dielectric constant. For example, the total capacitance of two dielectrics in series is given by

$$1/C_{tot} = 1/C_1 + 1/C_2 \ , \tag{1.1}$$

where C_1 and C_2 are the capacitances of the two layers, hence the result is dominated by the lowest capacitance. This leads to a lower total capacity. Therefore, much of the expected increase in the gate capacitance associated with the high-k dielectric is compromised.

The largest benefit of using SiO_2 as the underlayer of a stack at the Si channel interface is that the unparalleled quality of the SiO_2-Si interface will help to maintain a high channel carrier mobility. The usage of such SiO_2 interface layers was examined by Roy and Kizilyalli (1998) and Kizilyalli *et al.* (1998). In these works, a Ta_2O_5 film was sandwiched between SiO_2 layers located at the substrate and gate (poly-Si) interfaces.

Recent developments in employing high dielectric layers have centered on hafnium based dielectrics (Robertson, 2006). The main limitation of Hf-based dielectrics is that they require either a significantly thick (> 0.5 nm) SiO_2 interlayer or must be alloyed with SiO_2 to form silicates that have lower dielectric constants, thereby limiting the future scalability.

1.2.2 Field Effect Transistor Applications

The complementary metal oxide semiconductor (CMOS) field effect transistor (FET) made from silicon is the most important electronic device. This is due to its low power consumption and its performance improvement over forty years according to Moore's Law of scaling. This law says that the number of devices on an integrated circuit increases exponentially, doubling over a 23 year period. The minimum feature size in a transistor decreases exponentially each year. The *International Technology Roadmap for Semiconductors* (ITRS; http://www.itrs.net) defines how each design parameter will scale in future years to continue this trend.

Commonly it is said that the scaling will limit Moore's law when in lithography very short wavelengths of light to pattern the minimum feature size are needed. Nowadays it turns out that materials are now a key constraint. First, the maximum current density in interconnects between transistors led to copper replacing aluminium as the conductor. Then, RC time delays led to the replacement of SiO_2 inter-metal dielectric by materials of lower dielectric constant such as SiO_2:F or porous SiOCH alloys. But the most serious problem in logic circuits is now the FET *gate stack*, which is the gate electrode and the dielectric layer between the gate and the silicon channel.

The thickness of the SiO_2 layer presently used as the gate dielectric is now so thin (under 1.4 nm) that the gate leakage currents due to direct tunnelling of electrons through the SiO_2 becomes too high, exceeding 1 A cm^{-2} at 1 V (Lo *et al.*, 1997), so that power dissipation increases to unacceptable values (Wilk *et al.*, 2001). In addition it becomes more difficult to make and measure accurately such thin films. Finally, the reliability of SiO_2 films against electrical breakdown decreases in thin films. These reasons lead to a desire to replace SiO_2 as a gate oxide. Tunnelling currents decrease exponentially with increasing barrier gate oxide thickness. A FET is a capacitance operated device, where the source drain current of the FET depends on the gate capacitance

$$C = \frac{\epsilon_0 k A}{t} \ , \tag{1.2}$$

where ϵ_0 is the permittivity of free space, k is the relative permittivity, A is the area and t is the oxide thickness. Hence, the solution to the tunnelling problem is to replace SiO_2 with a physically thicker layer of new material of higher dielectric constant k. This maintains the capacitance at a high level and results in the reduction of the tunnelling current. These new gate oxides are called *high–k oxides*.

For the electrical design of a device, the precise material is not important. Therefore it is convenient to define an *electrical thickness* of the new gate oxide regarding to its equivalent silicon dioxide thickness or *equivalent oxide thickness* (EOT) as

$$\mathrm{EOT} = \frac{3.9}{k} t_{high-k} \ . \tag{1.3}$$

Here 3.9 is the static dielectric constant of SiO_2. The aim is to develop high-k oxides which allow further scaling to continue to even lower values of EOT.

The gate leakage problem is known since the late 1990s (Lo *et al.*, 1997), but in this time the criteria for the choice of oxide were not yet clear. It was discussed whether to use high-k oxides or to circumvent the problem by using novel device

designs. However, the increasing importance of the low-power electronics, in mobile phones, laptops, etc. leads to the confrontation with this problem (Wilk *et al.*, 2001). Low standby power CMOS requires leakage currents of below 1.5×10^{-2} A cm^{-2} rather than just 1 A cm^{-2}.

As mentioned before hafnium based dielectrics were investigated in recent developments. Nevertheless, this candidate requires either a significantly thick (> 0.5 nm) SiO_2 interlayer or must be alloyed with SiO_2 to form silicates that have lower dielectric constants, which limits the future scalability (Robertson, 2006).

In this respect ternary rare earth oxides such as lanthanum aluminate have gained interest as possible candidates for the next generation of high-k materials. Among these oxides, rare earth scandates have been studied intensively because of their promising properties. Recent reports on thin films of $GdScO_3$ deposited by pulsed layer deposition (Zhao *et al.*, 2005) and electron beam evaporation (Wagner *et al.*, 2006) demonstrate that amorphous $GdScO_3$ films possess a dielectric constant comparable to HfO_2 (k ∼22-23) and low leakage currents. It was also shown that the films remain amorphous after annealing under conditions similar to those of the conventional source/drain dopant activation process for Si MOSFETs. $GdScO_3$ films were deposited by *atomic laser deposition* (ALD) with minimal interlayer thickness ($\approx$ 0.15 nm) while maintaining their desirable electrical and structural properties (Kim *et al.*, 2006). The films were pure and amorphous, both as-deposited and after a 5 min annealing at 950 ℃ and formed a sharp, smooth interface to Si. The amorphous $GdScO_3$ films have a high dielectric constant ($k \approx 22$), low fixed charge density, and low interface trap density. A film with 1 nm EOT also demonstrated that the leakage current density is less than 2 mA/cm^2 at 1 V gate bias.

These reports illustrate many of the desirable properties of $GdScO_3$ as a gate dielectric, and motivate the development of the electronic properties of the rare earth scandates.

1.2.3 Leakage Current

Device scaling will require the use of even smaller EOTs. Hence a major problem of leakage currents in high-k gate dielectrics is the tunnelling leakage current through the thin layer. Therefore an overview about leakage currents is given in this section.

Leakage currents at the gate J_G increase exponentially with decreasing barrier height and thickness for electron direct tunnelling transport. Yeo *et al.* (2002) defined a theoretical figure of merit, f, for direct tunnelling, based on the barrier height Φ, tunnelling mass m^* and dielectric constant k

$$J_G \propto \exp(-2f \times t),\ f = (2m^*\Phi)^{1/2} \left(\frac{k}{3.9}\right), \tag{1.4}$$

where t is the EOT. Leakage currents also depend on other factors, including the structure of the layer. Polycrystalline gate dielectrics may be problematic because grain boundaries serve as high-leakage paths, and this may lead to the need for an amorphous interfacial layer to reduce leakage currents. In addition, grain size and orientation changes within a polycrystalline film can cause significant variations in k, leading to irreproducible properties. There are some counter-examples where very

encouraging properties for ZrO_2 produced by *atomic layer chemical vapour deposition* (ALCVD) are reported by Houssa *et al.* (2000). In this study a gate dielectric stack is used, with the ZrO_2 film on top of an amorphous SiO_2 layer. However, the amorphous SiO_2 layer may influence electrical properties. This issue will become important, as the SiO_2 layer presents a limit to the minimum achievable EOT value for these structures.

The work by van Dover (1999) used lanthanide dopants in TiO_x films to create and maintain an amorphous film for capacitor applications, even though TiO_2 is typically crystalline already at low temperatures. Very encouraging results were obtained, as both high permittivities and low leakage currents were achievable with Nd, Tb, and Dy dopants, but these particular films are not stable on Si.

Single crystal oxides grown by *molecular beam epitaxy* (MBE) methods (Eisenbeiser *et al.*, 2000; Kwo *et al.*, 2000) can in principle avoid grain boundaries while providing a good interface, but these materials also require submonolayer deposition control, which may only be obtainable by MBE approaches. Kwo *et al.* (2000) formed capacitors with single-domain, crystalline Gd_2O_3 films on Si by MBE, which had no apparent interfacial layer according to infrared absorption spectroscopy. Leakage currents for these films was 10^{-3} A/cm^2 at 1 V bias, and CV (capacitance versus voltage) analysis showed $k \approx 14$, while some frequency dependence was observed and the permittivity decreased with decreasing film thickness (Kwo *et al.*, 2000). For perovskite materials such as $SrTiO_3$, where the structure consists of alternating SrO and TiO_2 planes, each single atomic-height step edge, which always exist on the surface of Si wafers, may possibly serve as a nucleation site for an antiphase boundary and possibly a grain boundary. Any of these dielectrics which require interfacial layers on the Si channel, to avoid reaction between the high-k material and Si, will also require a metal gate, or perhaps a buffer layer at the poly-Si gate interface. In contrast to that, amorphous films will exhibit isotropic electrical properties, will not suffer from grain boundaries, and can easily be deposited by manufacturable techniques.

Robertson (2006) made six conditions for the new oxides to be acceptable as gate dielectrics, a high enough k value, thermal stability, kinetic stability, band offsets, good interface quality with Si and low bulk defect density. Robertson stated that HfO_2 and Hf silicate have emerged as the preferred oxides. The necessary deposition and processing to produce working devices have been achieved. However, there are still problems with these oxides in order to achieve high performance devices. This requires improvement of flat band voltage and lower defect densities. The flat band voltage shift may be due to interface defects and interface behaviour at the gate oxide/gate electrode interface. The main defects in the oxides are oxygen vacancies and interstitials. The oxygen vacancies are most problematic as they give rise to defect levels close to the Si conduction band. Flat band voltage instability is due to electron trapping at the O vacancy. Mobility degradation is largely due to remote charge scattering by charged defects in the oxide. DC flat band voltage shifts tend to be due to interaction and reaction of the gate electrode and the high-k oxide.

A promising class of materials for high-k applications are the rare earth scandates ($REScO_3$) because of their favourable material properties. For single crystals of these ternary oxides, Schlom and Haeni (2002) found dielectric constants of 20-35 depending on the lattice direction. Lim *et al.* (2002) determined an optical band gap larger than

5 eV, and Afanas'ev *et al.* (2004) confirmed this value for thin amorphous films grown by pulsed laser deposition (PLD). In addition, these authors found conduction and valence band offsets to silicon of 2-2.5 eV. The thermal stability of $LaScO_3$, $GdScO_3$ and $DyScO_3$ thin films deposited with off-axial pulsed laser deposition was investigated by Zhao *et al.* (2005). They showed that in contact with silicon the amorphous phase of $LaScO_3$ is stable up to 800 ℃, while $DyScO_3$ and $GdScO_3$ thin films remain amorphous up to 1000 ℃. Thin layers of $GdScO_3$ on *n*-type or *p*-type silicon were prepared by Kim *et al.* (2006) with a thickness of 4.9 nm which is equal to EOTs of around 1 nm. The interface was smooth and abrupt. The leakage current density was smaller than 2×10^{-3} A/cm^2 at 1 V gate voltage bias. Another candidate as gate dielectric material is $LaLuO_3$ which was grown as 6 nm thin film on *p*-type silicon by Lopes *et al.* (2006). This material has similar properties as the rare earth scandates and a dielectric constant of about 32.

1.3 Substrates for Strain Tailoring

Enormous strains can exist in thin films when one material is deposited on another (Nix, 1989), resulting from differences in crystal lattice parameters and thermal expansion behaviour between the film and the underlying substrate or arising from defects formed during film deposition (Speck *et al.*, 1995; Nix and Clemens, 1999). Although such strain often leads to degraded film properties, if suitable substrates and growth parameters are used, strain offers the opportunity to enhance particular properties of a chosen material in thin film form, namely strain engineering. As a result, the properties of thin films can be markedly different from the intrinsic properties of the corresponding unstrained bulk materials. Enormous strains induced to thin films have previously been used to alter the T_C of ferromagnetic (Beach *et al.*, 1993; Gan *et al.*, 1998) and superconducting (Lock, 1951; Sato and Naito, 1997; Bozovic *et al.*, 2002) materials. For such phenomena, strain-induced enhancements in T_C as large as tens of degrees have been observed (Beach *et al.*, 1993). Owing to the strong coupling between strain and ferroelectricity, much larger T_C shifts are expected (Devonshire, 1954; Pertsev *et al.*, 1998), and have been observed (Abe *et al.*, 1998; Streiffer, 2002), in ferroelectric materials.

Prominent examples for strain tailoring are room temperature ferroelectricity in strained $SrTiO_3$ (Haeni *et al.*, 2004) and the enhancement of ferroelectricity in strained $BaTiO_3$ thin films (Choi *et al.*, 2004). In strontium titanate T_C was increased by hundreds of degrees and room temperature ferroelectricity was produced. This material is usually not ferroelectric at any temperature. A thin film of $BaTiO_3$ was grown by molecular beam epitaxy on $GdScO_3$ and $DyScO_3$ with the result that the ferroelectric transition temperature was nearly 500 ℃ higher and remanent polarization at least 250% higher than for bulk $BaTiO_3$ single crystals. More recently $DyScO_3$ was used as substrate to tailor the ferroelectric properties of the multiferroic $BiFeO_3$ by Chu *et al.* (2006) and Pabst *et al.* (2007). They found self–oriented 1D periodic ferroelectric domain structures in $BiFeO_3/SrRuO_3/DyScO_3$ heterostructures. This ferroelectric domain structure depends on the growth mechanism.

In practice, the synthesis of uniformly strained ferroelectric films is challenging. Epitaxial ferroelectric films are usually grown to thicknesses greatly exceeding their

critical values, resulting in undesirable relaxation towards a zero-strain state by the introduction of dislocations. Dislocation densities of $\sim 10^{11}$ cm^{-2} are typical in epitaxial $Ba_xSr_{1-x}TiO_3$ films (Canedy *et al.*, 2000), and the resulting inhomogeneous strain further smears the phase transition, in addition to the effects of chemical heterogeneity mentioned above. The approach to controlling the properties of ferroelectric $SrTiO_3$ or $BaTiO_3$ films centers on the development of new substrates that enable the growth of uniformly strained films below, or at least closer to, the critical thickness for relaxation. Depending on the choice of substrate, films may be grown under compressive or tensile strain. For $BaTiO_3$ films the chosen substrates are $GdScO_3$ and $DyScO_3$ single crystal substrates, because they are structurally (Schubert *et al.*, 2003), chemically (Schubert *et al.*, 2003), and thermally (Biegalski *et al.*, 2005) compatible with $BaTiO_3$, and they have appropriate lattice constants to impart a strain ϵ_s of about 1.0% and 1.7%, respectively, on coherent (001) $BaTiO_3$ films (Choi *et al.*, 2004). For thin films of $SrTiO_3$, $DyScO_3$ was taken as a substrate because of the lattice mismatch of +1.0% at room temperature and $DyScO_3$ is not ferroelectric down to 4 K (Haeni *et al.*, 2004).

1.4 Multiferroics

Multiferroic materials show at least two order parameters among ferroelectricity, ferromagnetism (or antiferromagnetism) and ferroelasticity. The huge interest in this materials during the last decade is due to their potential applications including multiple-state memory elements, magnetic-field sensors and electric-field-controlled ferromagnetic resonance devices with magnetically modulated piezoelectricity (Smolenskii and Chupis, 1982; Hill, 2000).

The existence of ferromagnetism and ferroelectricity in the same phase in the conventional form is a contradiction. The usual mechanism for ferroelectricity is the cation-offcentering which requires empty d orbitals. The formation of magnetic moments results normally from partially filled d orbitals. This contradiction can be overcome if the offcentered ions are different from the magnetic ions. Multiferroism in magnetic perovskites and related materials is achieved by use of different sites. The large A-site cation can provide ferroelectricity, while the small B-site cation is magnetic. This mechanism was used in Bi-based ferroelectrics like $BiFeO_3$ (Wang *et al.*, 2003). Meikeljohn and Bean (1956) found such a coupling for the first time. Therefore the magnetoelectric effect is not new, but the promising application is of future interest. Very recently Chu *et al.* (2008) have coupled a ferromagnetic $Cu_{0.9}Fe_{0.1}$ with antiferromagnetic and ferroelectric $BiFeO_3$ resulting in the control of magnetism with an electric field. This indirect switching gives first possibilities for the application. As mentioned before (section 1.3) the ferroelectric properties of $BiFeO_3$ can be tailored by the choice of the substrate, like $DyScO_3$ (Chu *et al.*, 2006; Pabst *et al.*, 2007). Another possibility for multiferroic behaviour can be achieved with geometrically driven ferroelectricity, like in the antiferromagnetic ferroelectrics $YMnO_3$ (van Aken *et al.*, 2004; Fennie and Rabe, 2005) and $BaNiF_4$ (Ederer and Spaldin, 2006). Kimura *et al.* (2003) found that in $TbMnO_3$ ferroelectricity is induced by the formation of a symmetry-lowering magnetic ground state without inversion symmetry, where the polarization is small, but the magnetoelectric interactions may be strong. Finally

charge ordering can cause ferroelectricity in magnetic materials, which is the case in $LuFe_2O_4$ (Ikeda *et al.*, 2005b; Subramanian *et al.*, 2006). van den Brink and Khomskii (2008) focus in their work materials in which charge ordering induces ferroelectricity. They sort the multiferroics in two groups. In 'type–I' multiferroics ferroelectricity and magnetism have different origins and occur at different temperatures. The multiferroelectricity in the 'type–II' materials is completely due to magnetism and charge ordering plays a big role. $LuFe_2O_4$ belongs to the 'type–I' multiferroics.

$LuFe_2O_4$ (LFO) is a candidate for room temperature multiferroics. The room temperature magnetodielectric effects were observed by Subramanian *et al.* (2006). The anomalous dielectric and charge ordering behaviour has been investigated in detail (Yamada *et al.*, 1997; Ikeda *et al.*, 1998, 2000). The key factor of the multiferroic properties in this material is the mixed valence state of Fe. The formal iron valence state is +2.5. The iron sites are equal from the structural point of view, but the Fe^{2+} and Fe^{3+} ions are ordered on a triangular lattice. This valence ordering in a charge frustrated system leads to ferroelectricity (Ikeda *et al.*, 2005b, 2007). Ikeda *et al.* (2005a) presented a spin and charge order model (Siratori *et al.*, 1992) where the Fe^{2+} spin contributes to the majority spin and Fe^{3+} contributes with 1/3 to the majority and with 2/3 to the minority spin. The charge is stripe like ordered in this model. This charge and spin ordering was confirmed theoretically by Nagano *et al.* (2007). Usual ferroelectric crystals have a spontaneous electric polarization arising from the coherent arrangement of electric dipoles where a polar displacement of anions and cations is present. The covalent bond between the anions and cations, or the orbital hybridization of electrons on both ions, plays a key role for the dipolar arrangement in this usual off-centering ferroelectrics (Cohen, 1992; Sághi-Szábo *et al.*, 1998; Kuriowa *et al.*, 2001). Portengen *et al.* (1996) have proposed an alternative model, namely electronic ferroelectricity, in which the electric dipole depends on electron correlations, rather than on the covalency. This would offer the attractive possibility of ferroelectric materials that could be controlled by the charge, spin and orbital degrees of freedom of the electron. These materials offer, in contrast to the before mentioned $BiFeO_3$ coupled with $Cu_{0.9}Fe_{0.1}$, a direct magnetoelectric switching.

Magnetic properties of LFO stemming from 2D ferrimagnetic ordering have also been investigated using neutron diffractions, magnetization, and Mössbauer measurements (Iida *et al.*, 1993). The 2D ferrimagnetism parallel to the c-axis occurs below 210 K and remains even at 4.2 K. Ferrimagnetic clusters of various sizes are frozen below 210 K and lead to a spontaneous magnetic moment of approximately 1.4 μ_B per formula unit where the easy axis is along the c-axis of the crystal (Iida *et al.*, 1993). Above this temperature smaller clusters need higher magnetic fields to polarize in the direction of the field against thermal fluctuation. Neutron diffraction reveals that the magnetic correlation along the c-axis does not change with temperature. Ferromagnetic correlation between two layers in a W-layer and weak antiferromagnetic coupling between adjacent W-layers was found. The Curie temperature was determined to 250 K by Bang *et al.* (2008). They found the three dimensional charge ordering to be stable up to 330 K. At higher temperatures the charge ordering is two dimensional (Yamada *et al.*, 1997) until it finally breaks down completely at 370 K due to electron hopping. The frequency of this electron hopping decreases with the

reciprocal temperature (Ikeda *et al.*, 2007). At room temperature the hopping frequency is in the range of 10^6 Hz and at around 200 K the frequency is around 10^4 Hz. This electron hopping is the elementary process of the dielectric relaxation. Very recently Qin *et al.* (2009) investigated the influence of substitution from Fe^{2+} with Mg^{2+} which has an effect on the electron hopping and the magnetic properties. Also the lattice parameters change progressively with increasing Mg content. At low temperatures (down to 20 K) TEM measurements clarified the charge ordering to be a charge-stripe phase which can explain the ferroelectricity in LFO (Zhang *et al.*, 2007).

Chapter 2

Basics of X-ray Spectroscopy

To characterize the electronic, magnetic and chemical structure of solids there are some x-ray spectroscopic methods which are used in the present work. These are x-ray photoelectron spectroscopy (XPS), x-ray absorption spectroscopy (XAS) and x-ray emission spectroscopy (XES). By dint of these methods one can reveal information about the chemical state of different elements, magnetic properties and stoichiometry of solid materials.

The XPS method is based on the photoelectric effect where an x-ray photon excites an electron of the core level, which can leave the solid, if it has enough kinetic energy. The resulting free electrons can be detected, resolved in their exit angles and energies. The binding energies of the detected electrons provide information about the elements within the sample, the valence states and the magnetic properties. The peak intensities corresponding to the elements contained in the compound give information about the stoichiometry of the sample. The XPS method gives the total density of states (tDOS). The XES method is based upon the recombination of a core hole with an electron of a higher level, e.g., originating from the valence band. If one knows the binding energies of the core levels, it is possible to determine the partial density of states (pDOS) of this element in the valence band. The partial density of states of the unoccupied states in the conduction band can be probed by XAS. Here an electron of a core level is excited to an unoccupied state of the conduction band.

The methods XPS, XES and XAS are complementary to each other and provide information about the electronic structure of the samples. There are more specific methods of absorption and emission spectroscopy. X-ray magnetic circular dichroism (XMCD) and x-ray magnetic linear dichroism (XMLD) are absorption methods excited with circular polarized light and linear polarized light, respectively. In XMCD, different circular helicities of light give a difference in the absorption signal for paramagnetic materials in a magnetic field (see chapter 2.3.2). For XMLD linearly polarized light is used, which is parallel or perpendicular to the magnetization of an antiferro- or ferromagnetic sample, resulting in different absorption spectra (see chapter 2.3.3). The resonant x-ray emission spectroscopy (RXES) is an XES method where the core level is resonantly excited. Then the electron is excited just to the conduction band instead of leaving the material completely. If the excited electron is recombining with the created core hole this transition is called elastic. If the core hole is filled with an electron of the valence band this transition is called inelastic. The inelastic part

of the resonant excited emission spectrum is observed in the resonant inelastic x-ray scattering (RIXS).

2.1 Theoretical Models

The theoretical description of the electronic structure of transition metal and rare earth oxides is a difficult task. For our discussion, a reference to two different approaches will be useful. On the one hand there is the *band model* which can describe delocalized electrons in the valence band region. The hybridization between metal atoms and ligand atoms is well reproduced and the interatomic interaction plays a major role. On the other hand this approach faces problems in describing localized core level excitations, like the XAS of the metal L edge. Such experiments are often better described within the *multiplet model* where a separated atom is modelled and the interatomic interaction is included by the crystal field of the ligand atoms. An example is the localized $3d$ electrons in transition metal compounds. During a direct transition from $2p$ to $3d$ levels in the course of an L edge XAS process, the partly filled d band interacts with the $2p$ core level and this is leading to multiplet splitting in the spectra. These multiplet effects have smaller influence on the more delocalized valence electrons of ligand atoms, i.e. in the K edge XAS of oxygen.

To get a complete theoretical description of transition metal and rare earth oxides, both models have to be applied, because there is a competition between different interactions in such compounds, which leads to a more localized or to a more delocalized behaviour of the electrons at different atoms and levels.

2.1.1 Band Models

The band model is often implemented by use of the density functional theory (DFT) which was introduced by Hohenberg and Kohn (1964). A good review about the application and prospects of the density functional formalism is given by Jones and Gunnarsson (1989). The Born-Oppenheimer approximation is used in which the slow movement of heavy atomic cores is decoupled from that of much lighter electrons (Kohn, 1999). The eigenfunctions $\phi_i(\mathbf{r})$, which define the electron density can be found from solving the Kohn-Sham equations (Kohn and Sham, 1965):

$$\left[-\frac{\hbar^2}{2m}\nabla_i^2 + V_{eff}(\mathbf{r})\right]\phi_i(\mathbf{r}) = \epsilon_i\phi_i(\mathbf{r}) \ . \tag{2.1}$$

Here V_{eff} is the effective periodic potential of the crystal lattice

$$V_{eff} = \frac{e^2}{4\pi\epsilon_0}\int d\mathbf{r}^{'}\frac{\rho(\mathbf{r}^{'})}{|\mathbf{r}-\mathbf{r}'|} + V_{ext}(\mathbf{r}) + V_{xc}(\mathbf{r}). \tag{2.2}$$

This potential comprises the classical Coulomb field due to electron density $\rho(\mathbf{r})$, the external Coulomb potential due to the lattice of ions V_{ext} and the so–called exchange and correlation potential V_{xc}

$$V_{xc}(\mathbf{r}) = \frac{\delta E_{xc}[\rho]}{\delta\rho(\mathbf{r})} \ , \tag{2.3}$$

where E_{xc} is the exchange correlation energy. The ground state density $\rho(\mathbf{r})$ of an N-electron system, after Kohn and Sham (1965), is expressed in terms of the above eigenfunctions:

$$\rho(\mathbf{r}) = \sum_i \phi_i(\mathbf{r})^* \phi_i(\mathbf{r}). \tag{2.4}$$

The summation is over the N lowest occupied eigenstates.

There is a theorem by Hohenberg and Kohn (1964) which states that the total energy of an electron system in its ground state (and hence all properties related to it) is uniquely defined by the electron density. In practice, some approximations are necessary to describe the exchange–correlation potential V_{xc} which comprises the complexity of interactions in the whole electron system.

The exchange–correlation potential is that created by the "exchange–correlation hole" $\rho_{xc}(\mathbf{r}, \mathbf{r}')$, which is carried around each electron and accounts for the reduction of the density of other electrons in the vicinity of it due to the effects of exchange (Pauli principle, excluding the electrons of the same spin) and correlation (Coulomb interaction, excluding all other electrons independently of spin). The exchange–correlation energy then appears as purely electrostatic interaction of the electron density with the exchange–correlation hole around each electron:

$$E_{xc} = \frac{e^2}{2} \int\int d\mathbf{r} d\mathbf{r}' \frac{\rho(\mathbf{r})\rho_{xc}(\mathbf{r}, \mathbf{r}')}{|\mathbf{r} - \mathbf{r}'|} \equiv \int d\mathbf{r} \rho(\mathbf{r}) \epsilon_{xc}(\mathbf{r}) \ , \tag{2.5}$$

with $\epsilon_{xc}(\mathbf{r})$ the exchange energy density.

A crucial and historically important step is the *local density approximation* (LDA) (Kohn and Sham, 1965), according to which $\epsilon_{xc}(\mathbf{r})$ is not a general function of $\mathbf{r}$, hence depending on $\rho_{xc}(\mathbf{r}, \mathbf{r}')$ in the whole space, but a function of ρ only in point $\mathbf{r}$:

$$\epsilon_{xc}(\mathbf{r}) = \epsilon_{xc}[\rho(\mathbf{r}, \mathbf{r}')] \rightarrow \epsilon_{xc}[\rho(\mathbf{r})] \ . \tag{2.6}$$

This approximation, and corresponding parametrization for the ϵ_{xc} function, comes from the results obtained for the homogeneous electron gas.

In practical terms it turns out that for an electron gas having a certain spin polarization it is easier, and numerically more accurate, to construct a parametrization of ϵ_{xc} in terms of two components of the spin density, $\rho^+(\mathbf{r})$ and $\rho^-(\mathbf{r})$, rather than in terms of their sum only. Note that the Heisenberg–Kohn theorem says nothing about an importance of two spin components separately, and the exchange–correlation energy must be (somehow) expressible via just the summary density. This updated approximation (Hedin and Lundqvist, 1971; von Barth and Hedin, 1972) is called that of *local spin density* (LSDA).

Further improvements in the parametrization of the exchange–correlation potential, especially important for correct description of magnetic systems, include various flavours of the *generalized gradient approximation* (GGA), which includes the dependence on the gradients of electron density.

A priori the straightforward L(S)DA nor similar calculations cannot be expected to directly provide the band gap in semiconductor or dielectric systems as the difference between the Kohn–Sham eigenvalues of the lowest unoccupied and the highest

occupied orbitals. This is so because the DFT approach is, strictly speaking, formulated for the ground state only, whereas optical excitation brings the system out of the ground state. Special more complicated methods (e.g., the GW approximation) exist, which allows a systematically good calculation of excitation spectra and hence band gaps. For a special case when the band gap is of Mott–Hubbard type. However, a symplified and yet reasonably accurate approach, known as LDA+U (Anisimov *et al.*, 1991, 1992) can be used. This method imitates the variation of the occupation numbers of relevant (sufficiently localized) orbitals, hence (approximately) an effect of electronic correlations within the corresponding shell, insufficiently accounted for in the standard LDA. Technically, the LDA+U formalism introduces a correction to the nominal LDA exchange–correlation energy, adding to it an orbital- and occupation-dependend part ($n_d = \sum_{m,\sigma} n_{im\sigma}$) as in the Hubbard model, and substracting the averaged description of interactions ($n^0 = n_d/10$) within the localized shell in question, according to LDA:

$$V_{LDA+U}(\mathbf{r}) = V_{LDA}(\mathbf{r}) + U \sum_{m'} (n_{m'-\sigma} - n^0) + (U - J) \sum_{m'(\neq m)} (n_{m'\sigma} - n^0). \qquad (2.7)$$

This modified exchange–correlation potential applies to a selected shell only, and is orbital (occupation)-dependent. It depends on the parameters U and J, which play the role of Coulomb and exchange integrals, but they do not inherently come from inside the approach. Hence they are usually introduced as external (adjustable) parameters. The choice of the shell for which the correction will be applied occurs ad hoc; these are typically TM $3d$ and RE $4f$ shells.

Practical solution of the Kohn–Sham equations proceeds numerically, by expanding the wavefunctions $\phi_i(\mathbf{r})$ over appropriately chosen basis functions. In the band structure calculations discussed in the present work, the *linearized augmented plane waves* method with *local orbitals* (LAPW + lo) is used. The basis functions of this method are hybrid, composed of numerical solutions within atom–centered non–overlapping spheres (region I in figure 2.1, smoothly matched with plane waves in the region between the spheres (region II in figure 2.1). The numerical in–sphere part of the basis is adjusted from one iteration to the next in the course of self–consistent calculation, and the plane wave cutoff parameter controls the (usually of the order of several thousands) dimension of the basis. So–called local orbitals provide adequate description of the "semicore states" (i.e. those deeply lying yet potentially contributing to the chemical bonding, like e.g. $3s$, $3p$ in $3d$ transition metals). Taken together, this accounts for a generally recognized numerical precision of the LAPW method, the details of which are well described by Singh (1994). The calculations have been done using the implementation of the LAPW + lo method in the WIEN2k computer package (Blaha *et al.*, 2001).

2.1.2 Multiplet Models

In many x-ray and electron spectroscopies, the multiplet effects play an important role. If a core hole is present in the final state of an x-ray excitation process, the wave function of the core hole is overlapping with the wave functions of the unpaired

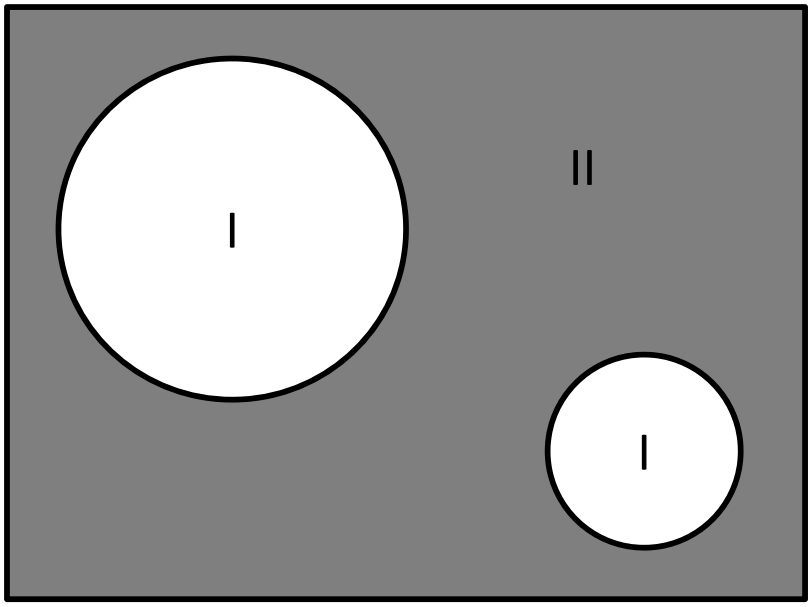

Figure 2.1: Separation of the unit cell in muffin tin regions (I) and the interstitial region (II), in case of two unequal atoms.

valence electrons. The spectroscopic experiments do not show anymore the ground state of the system which is implied in the band structure calculations. Hence for core hole excitations where the multiplet effects are important, other models are necessary to describe the experimental results in a proper way. Such models concentrate on the atomic effects, but neglect, to some extent, the interatomic interaction, which is included as an additional perturbation. The multiplet splitting is described in the section 2.5.3.

Hubbard and Anderson impurity models In rare earth and transition metal oxides, the electrons can be transferred from one site to another by using the correlation energy U, which accounts for the interaction between the electrons. This energy can be found in the comparison of *X-ray Photoelectron Spectroscopy* (XPS) and *Bremsstrahlung Isochromat Spectroscopy* (BIS) as the energy difference between the state with $N-1$ electrons and the state with $N+1$ electrons (Hüfner *et al.*, 1991). In the case of transition metals this correlation takes place between $3d$ states and then the correlation energy is called U_{dd}. The core level spectra of this correlated systems can be described with the Hubbard model (Hubbard, 1963, 1964a,b). In this model the repulsion of electrons at different sites is neglected. The correlation between electrons at the same atom is given by the on–site Coulomb interaction U_{dd}. The Hubbard model usually is applied for the TM $3d$ and the O $2p$ states.

In the single Anderson impurity model (Andersen, 1961) the interaction around the metal site is included. Beside the correlation energy U_{dd} also the energy positions of the localized and delocalized states ϵ_d and ϵ_p are included as well as the hopping terms t_{pd} and t_{pp} (Fujimori *et al.*, 1984; Fujimori and Minami, 1984). This model was applied to $4f$ systems (Kotani and Shin, 2001), but for the $3d$ systems of transition

metal compounds a strong hybridization between the metal and the oxygen ligand is present, which makes the description of such systems more complex.

Crystal field and charge transfer multiplet calculations In the crystal field multiplet model a single atom is described which is influenced by the crystal field of the ligand atoms. The crystal field theory has a long history. It was developed by Becquerel (1929), Bethe (1929, 1930), Kramers (1929, 1930) and van Vleck (1932) in order to describe the electronic and chemical properties of d-metal ions in crystals. The ligand ions are treated as a point charge. For example the $3d$ states ($l = 2$) of a free atom are five fold degenerated ($2l + 1 = 5$). In a non spherical crystal field the point charges of the ligands interact with the $3d$ orbitals of the metal ion and the dengenerated states will split with respect to the symmetry of the ligands as presented in the splitting pattern scheme in figure 2.2. It should be noted that due to distorted ligand fields more splittings can occur or the order can change. In an octahedral crystal field the five $3d$ orbitals are energetically split in two groups (t_{2_g} and e_g), which is described with one splitting parameter $10Dq$. The more complex splitting in a trigonal bipyramidal or a distorted octahedral crystal field is described with the three parameters, namely $10Dq$, Dt and Ds. A good overview about the crystal field theory is given by Moffit and Ballhausen (1956).

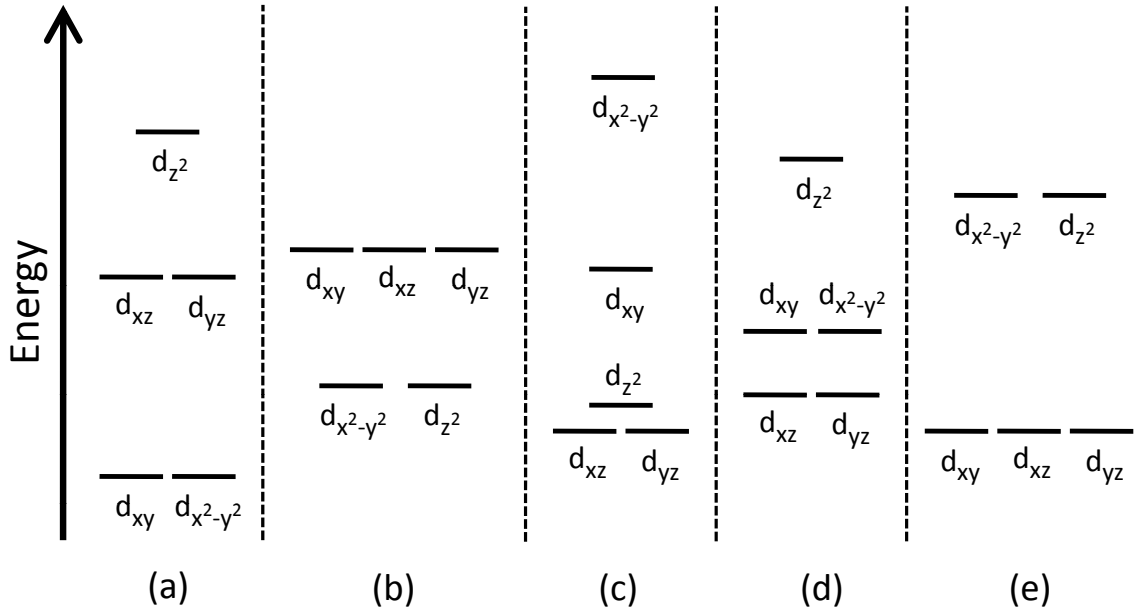

Figure 2.2: Splitting patterns of d orbitals in ligand fields for (a) linear ML_2, (b) tetrahedral ML_4, (c) square-planar ML_4, (d) trigonal-bipyramidal ML_5 and (e) octahedral ML_6.

For crystal field multiplet calculations one starts with the atomic Hamiltonian of a free atom

$$H_{atom} = \sum_N \frac{p_i^2}{2m} + \sum_N \frac{-Ze^2}{r_i} + \sum_{pairs} \frac{e^2}{r_{ij}} + \sum_N \xi(r_i) l_i \cdot s_i. \tag{2.8}$$

This Schrödinger equation comprises the kinetic energy of the electrons ($p^2/2m$), the electrostatic interaction of the electrons with the nucleus (Ze/r), the electron electron repulsion (e^2/r) and the spin–orbit coupling of each electron ($l \cdot s$). The first two terms in equation 2.8 are the same for all electrons in a given atomic configuration. They can be summarised in the average energy of the configuartion (H_{av}). The different terms within a configuration are defined by the electron electron repulsion and the spin–orbit coupling. The average of the spherical part of the electron electron repulsion is added to H_{av}. The energies of different terms is then given by the modified electron electron Hamiltonian H'_{ee} and the spin–orbit Hamiltonian H_{ls}. The general formulation of the matrix element of the effective electron electron H'_{ee} is given by the Slater–Condon parameter $F^i(f_i)$ (radial part of the direct Coulomb repulsion) and $G^i(g_i)$ (Coulomb exchange interaction):

$$\left\langle {}^{2S+1}L_J \left| \frac{e^2}{r_{12}} \right| {}^{2S+1}L_J \right\rangle = \sum_k f_k F^k + \sum_k g_k G^k \ . \tag{2.9}$$

The exchange interaction g_i is only present for electrons of different shells. If one now takes into account the crystal field, the atomic Hamiltonian is extended with an electrostatic field. This field is described by the electronic charge e and the potential $\Phi(r)$ which represents the surroundings

$$\Phi(r) = \sum_{L=0}^{\infty} \sum_{M=-L}^{L} r^L A_{LM} Y_{LM}(\Psi, \Phi) \ . \tag{2.10}$$

The crystal field is treated as a perturbation to the atomic Hamiltonian. Hence the matrix elements of the potential $\Phi(r)$ have to be determined with respect to the atomic orbitals, $\langle 3d \left| \Phi(r) \right| 3d \rangle$ in the case of $3d$ orbitals. The spherical and the radial part of the matrix elements can be separated. The radial part represents the strength of the crystal field interaction and the spherical part can be written in Y_{LM} symmetry. Then the crystal field potential for $3d$ electrons is given by:

$$\Phi(r) = A_{00} Y_{00} + \sum_{M=2}^{2} r^2 A_{2M} Y_{2M} + \sum_{M=-4}^{4} r^4 A_{4M} Y_{4M} \ . \tag{2.11}$$

Here the first term $A_{00}Y_{00}$ is constant and will only shift the atomic states. It can be neglected if one is interested in the spectral shape.

As mentioned before the transition metal oxides show strong hybridization between the metal and the ligand states. This can be included in the calculations if one implements the Anderson impurity model in the multiplet calculations which can be comprehended in the publication of de Groot (2004). This results in the Hamiltonian H_{AIM} of the charge transfer multiplet calculations for transition metal oxides:

$$\begin{aligned} H_{AIM} = \epsilon_{3d} a^\dagger_{3d} a_{3d} + \epsilon_v a^\dagger_v a_v + t_{v3d}(a^\dagger_{3d} a_v + a^\dagger_v a_{3d}) \\ + \sum_{\Gamma_1,\Gamma_2,\Gamma_3,\Gamma_4} g_{dd} a^\dagger_{3d1} a_{3d2} a^\dagger_{3d3} a_{3d4} \\ + \sum_{\Gamma_1,\Gamma_2} l \cdot s a^\dagger_{3d1} a_{3d2} + H_{CF} \end{aligned} \ . \tag{2.12}$$

Here the first three terms represent the $3d$ state, the valence band states and the coupling between the $3d$ states and the valence band. The g_{dd} term describes all two–electron integrals and includes the Hubbard U as well as the effects of the Slater–Condon parameters F^2 and F^4. The last term represents the $3d$ spin–orbit coupling. This charge transfer multiplet model was applied to several transition metal compounds like NiO and $NaCuO_2$ (Okada *et al.*, 1991; van der Laan *et al.*, 1992).

2.2 X-ray Photoelectron Spectroscopy (XPS)

X-ray photoelectron spectroscopy (XPS) is based upon the photoelectric effect, which is schematically depicted in figure 2.3.

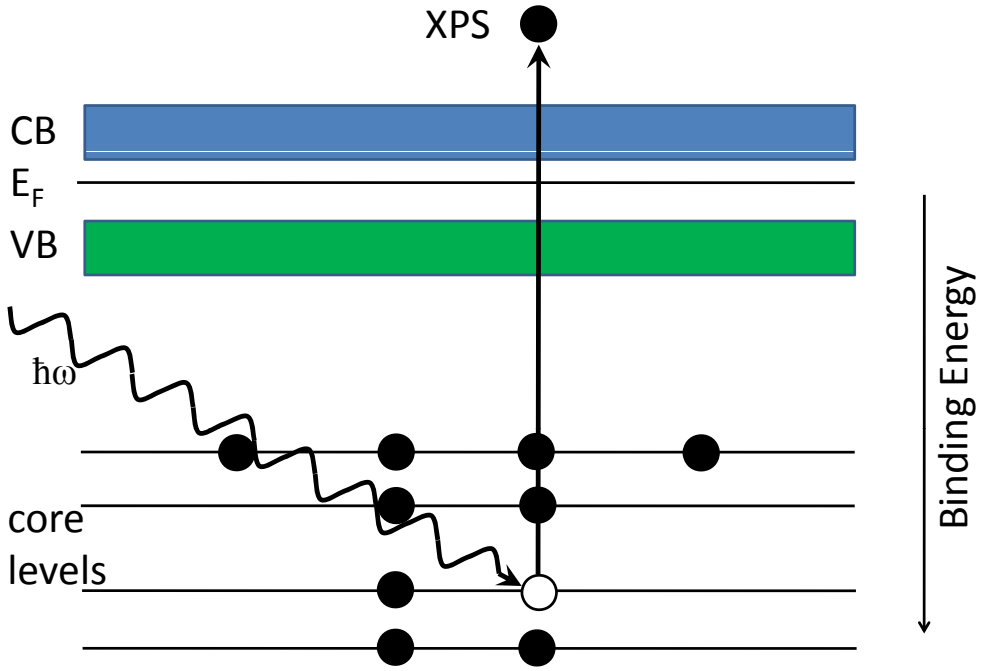

Figure 2.3: Scheme of x-ray photoelectron spectroscopy.

The effect was first discovered by Hertz (1887) who showed that a metal plate discharges faster when it is irradiated with light. Hallwachs (1888) correlated the velocity of discharge with the used material, wavelength and intensity of the light. The interpretation of this effect was given by Einstein (1905) with the light quantum hypothesis. In 1921 he was awarded with the Nobel prize for this work. The quantization of light leads to the formula with the maximum kinetic energy of a photoelectron:

$$E_{kin,max} = h\nu - \phi \ . \tag{2.13}$$

Here h is Planck's constant, ν is the frequency of light and ϕ is the work function which is the energy an electron has to overcome to leave the atom.

The equation 2.13 applies only for electrons at the Fermi level. For electrons with higher binding energy one can expand equation 2.13 with its effective binding energy $E_{B,eff}$. This leads to the equation:

$$E_{kin} = h\nu - E_{B,eff} - \phi \ . \tag{2.14}$$

Thus the binding energy can be determined by photoelectron spectroscopy. The measured parameter is the kinetic energy. The work function is given by the spectrometer if the sample is conductive and connected to it. The energy of the light depends on the anode material or is determined by a tuneable light source. So only the binding energy is variable in equation 2.14. This allows determining the binding energy by measuring the kinetic energy of the electron leaving the sample. The binding energies of the electrons and their quantity give a lot of information about the chemical and electronic properties of the sample. The binding energy is important because it is characteristic for each element.

As x-ray source in XPS, the characteristic x-ray radiation of metal anodes or synchrotron radiation is used. In the first (traditional) way, the electrons accelerated in an electron gun fall onto a metal anode, and as a result of their interaction therein the Bremsstrahlung (continuous spectrum) or characteristic for the anode (monochromatic) x-rays are emitted. The energy of such radiation is in the range of hundreds to ten thousands of electron volts (eV). Synchrotron radiation, wich is of limited availability in special equipped synchrotron sites, but has very high intensity, is often used for XPS because it is variable in frequency, allowing high resolution experiments provided by the usage of a good monochromator. The variable excitation energy is also used for resonant XPS.

2.2.1 Theoretical Approaches to the Photoemission Process

The photoemission process can be described within the *sudden approximation* where the electron emission is faster than the relaxation of the system. The transition probability ω between the initial state Ψ_i and the final state Ψ_f is given by Fermi's Golden Rule:

$$\omega = \frac{2\pi}{\hbar} \left|\langle \Psi_f \left| H \right| \Psi_i \rangle\right|^2 \delta(E_f - E_i - h\nu) \ . \tag{2.15}$$

The δ function certifies the energy conservation. The perturbation operator H is expressed as

$$H = \frac{e}{2m_e c}(\mathbf{A}\cdot\mathbf{P} + \mathbf{P}\cdot\mathbf{A}) - e\Phi + \frac{e^2}{2m_e c^2}|\mathbf{A}|^2 \ , \tag{2.16}$$

where m_e is the electron mass, e the electron charge and c the speed of light. $\mathbf{A}$ is the vector potential operator and Φ is the scalar potential of the exciting electromagnetic field. $\mathbf{P}$ is the momentum operator of the electron. If the two–photon process ($|\mathbf{A}|^2$) is neglected and it is moreover assumed that the radiation wave length $\gg$ atomic distances, then the perturbation Hamiltonian becomes more simple:

$$H = \frac{e}{m_e c}\mathbf{A_0}\mathbf{P} \ . \tag{2.17}$$

$\mathbf{A_0}$ is the constant amplitude of the electromagnetic wave. The vector potential operator can be expressed as $\mathbf{A}(\mathbf{r},t) = \mathbf{A}_0 \exp(\mathbf{kr} - \omega t)$ (Borstel, 1985). The interaction between the emitted electron and the remaining $(N-1)$ electron system can be neglected in the sudden approximation. Then the final state can be split into two configurations:

$$|\Psi_i(N); E_i(N)\rangle \rightarrow \left|\Psi_f^k(N-1); E_f^k(N-1)\right\rangle \cdot \left|\xi^k(1); E_{kin}^k\right\rangle . \tag{2.18}$$

$\left|\xi^k(1)\right\rangle$ is the wave function of the emitted photoelectron. The energy conservation during the photoemission process leads to the binding energy with respect to the Fermi level as

$$E_B^k = E_f^k(N-1) - E_i(N). \tag{2.19}$$

The *frozen orbital approximation* assumes the orbitals to be unmodified during the photoemission process. This approximation is based on Koopmans' theorem (Koopmans, 1933). Then the binding energy is given by the negative one–electron energy of the orbital where the electron is excited from:

$$E_B^k \simeq \epsilon^k. \tag{2.20}$$

It should be noted that this approximation does not consider that there is an intraatomic relaxation after the photoelectron process, and due to charge flow from the crystal also an extraatomic relaxation occurs.

Three-step and one-step models Berglund and Spicer (1964) considered in the *three–step model* the photoelectron process consisting of three independent events:
(1) the local absorption of the photon and the photo excitation of the electron,
(2) the propagation of the electron through the sample to the surface and
(3) the penetration of the photoelectron through the surface and emission into the vacuum.

The first process, namely the optical excitation of the electron, is following Fermi's Golden rule (equation 2.15).

During the second process, the propagation to the surface, some excited electrons lose part of their energy. For high energies these losses are due to electron electron interaction, and for low energies the electron plasmon interaction is dominant. The inelastic mean free path λ is the distance between two inelastic impacts of the electron which propagates through the crystal (Tanuma *et al.*, 1987):

$$\lambda(E) = \frac{E}{E_{plas}^2 \beta \ln(\gamma E)}. \tag{2.21}$$

β and γ are parameters, E is the kinetic energy of the electron and E_{plas} is the plasmon energy of a free electron gas, which is described by $E_{plas} = 28.8\sqrt{N_\nu \rho / M}$ where N_ν is the number of valence electrons per molecule, ρ is the density and M is the molecular mass. The mean free path can be reduced to the formula $\lambda = E^p$ where p is in the range from 0.6 to 0.8 (Jablonski, 1993). With this approximation, resonable results for the mean free path of electrons can be achieved in the soft x-ray

energy range ($\sim$ 100-1000 eV). The information depth for electrons is a few nm for x-ray photoelectron spectroscopy depending on the measurement geometry.

The third step of the three step model is the escape of the photoelectron into the vacuum. The kinetic energy of these electrons has to be high enough to overcome the potentital barrier. Electrons with too low energies are reflected at the surface. Since the energy projected to the normal of the surface is decisive, the information depth becomes smaller the more the detection angle deviates from the surface normal. Hence the measurement is more bulk sensitive for the geometry where the analyzer detects photoelectrons coming in the surface normal. Nevertheless XPS is always surface sensitive.

While the *three–step model* is more descriptive and illustrative, the *one–step model* is preferred for computational simulations of XPS spectra (Borstel, 1985). In this model the whole photoelectron process is treated as a single process. With specific crystal potentials as input data the one step model delivers theoretical simulations of the XPS spectra (Matzdorf *et al.*, 1999; Schlathölter, 1999).

2.3 X-ray Absorption Spectroscopy (XAS)

In the x-ray absorption spectroscopy (XAS) a core electron is excited to an unoccupied state above the Fermi level. A schematic illustration of XAS can be seen in figure 2.4.

The required energy E_{exc} is:

$$E_{exc} = h\nu = E_{final} - E_{initial} \ . \tag{2.22}$$

Here E_{final} is the energy of the final state with the core electron excited into the conduction band. $E_{initial}$ is the energy of the not excited initial state.

Due to the dipole selection rules only transitions which change the angular momentum quantum number l by one occur in the process ($\Delta l = \pm 1$). While the spin s is conserved ($\Delta s = 0$), the z-component of the orbital momentum m has to change by zero or one ($\Delta m = \pm 1, 0$). In particular, $\Delta m = \pm 1$ for left and right hand circularly polarized light and $\Delta m = 0$ for linear polarized light. There are quadrupole transitions which allow $\Delta L = \pm 2, 0$, but these transitions are hundred times weaker than the dipole transitions.

With XAS one probes site specifically the unoccupied density of states. This means that the electrons are excited from a specific core level to the unoccupied states, whereby only one atom sort is excited because each element has individual excitation energies for its levels.

To determine different states in the conduction band one has to use a tuneable source, e.g. the radiation of a synchrotron. The transition intensity can only be determined indirectly. In transmission or reflection experiments one measures the remaining intensity and calculates the absorption. For the metals one can measure the drain current from the sample which is proportional to the XAS signal. This is called *total electron yield* (TEY). If the sample is an insulator one can measure the intensity of radiant recombination which is called *partial* or *total fluorescence yield* (PFY- or TFY-mode).

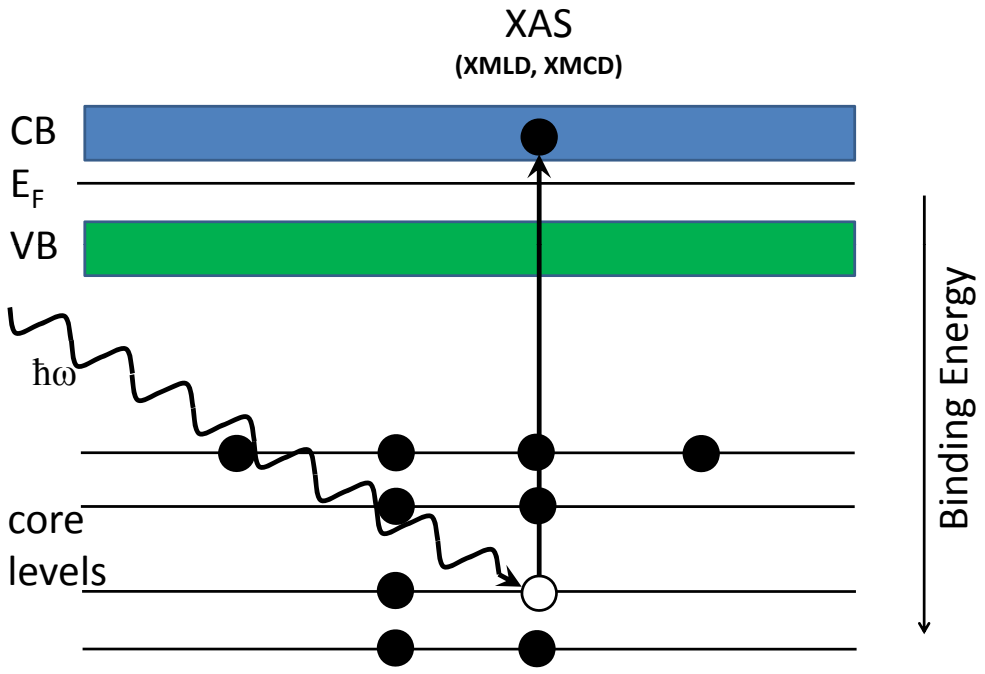

Figure 2.4: Scheme of the x-ray absorption process.

The XAS can be divided into two spectral regions, the so called near edge x-ray absorption fine structure (NEXAFS) which reflects excitations of the photoelectron into the unoccupied states, and the so called extended x-ray absorption fine structure (EXAFS). Here the photoelectron treated as a wave is excited into the continuum, and its superposition of backscattered waves from neighbouring atoms leads to characteristic features in the XAS, usually at photon energies well above the corresponding NEXAFS threshold.

2.3.1 Theoretical Description of the Absorption of X-rays

The x-ray absorption spectroscopy process is an excitation of a system, initially in a ground state Ψ_i, into a final state Ψ_f. The theoretical description of this process by Fermi's Golden Rule (see equation 2.23) is analogous to the XPS process

$$\omega = \frac{2\pi}{\hbar} \left| \langle \Psi_f \left| \hat{e}\vec{r} \right| \Psi_i \rangle \right|^2 \delta(E_f - E_i - h\nu) \ , \tag{2.23}$$

where $|\langle \hat{e}\vec{r} \rangle|$ is the dipole matrix element coupling initial and final state. The electric quadrupole transition is some hundred times smaller than the dipole transition and is therefore neglected (dipole approximation). The wave functions Ψ_i and Ψ_f are not exactly known, and for practical calculations of the x-ray absorption cross section one can make an approximation of a one–electron process (see equation 2.24). This

means an assumption that all other electrons do not participate in the transition from initial to final state. Then the initial state wave function can be rewritten as a core wave function c, and the final wave function as a free electron wave function ϵ. It is possible to rewrite the matrix element to a single electron matrix element M, which often is constant or slowly varying in energy:

$$\left|\langle \Psi_f \left|\hat{e}\vec{r}\right| \Psi_i\rangle\right|^2 = \left|\langle \Psi_i \underline{c}\epsilon \left|\hat{e}\vec{r}\right| \Psi_i\rangle\right|^2 \approx \left|\langle \epsilon \left|\hat{e}\vec{r}\right| c\rangle\right|^2 \equiv M^2. \tag{2.24}$$

One observes the density of empty states (ρ) which is implied by the delta function. This leads together with the one–electron approximation to the following intensity:

$$I_{\mathrm{XAS}} \sim M^2 \rho \ . \tag{2.25}$$

The dipole selection rules dictate that the dipole matrix element is non zero if the orbital quantum number of the final state differs by 1 from the initial state ($\Delta L = \pm 1$) and the spin is conserved ($\Delta S = 0$). That means that for example transitions like $s \rightarrow p$ and $p \rightarrow s$, $p \rightarrow d$, etc. are allowed when additionally the spin is conserved. The neglected quadrupole transitions follow other selection rules ($\Delta L = \pm 2$ or 0) where transitions $s \rightarrow d$, $p \rightarrow f$, $s \rightarrow s$ and $p \rightarrow p$, etc. are allowed.

2.3.2 X-ray Magnetic Circular Dichroism (XMCD)

The excitation with circular polarized light in XAS measurements leads to different absorption probabilities for different spin directions. This difference is measured by the spin dependent absorption coefficients μ^+ and μ^- for circular polarized light with parallel (+) and antiparallel (−) helicity with respect to the majority and minority spin, respectively. For example for the $2p_{3/2}$ state excited with right–hand circular polarized light, just taking into account the core hole excitation, the ratio between the excitation of spin up (majority) and spin down (minority) electrons is 62.5% to 37.5%. The ratio for the $2p_{1/2}$ state is 25% to 75%.

By means of x-ray magnetic circular dichroism (XMCD) one can analyse the magnetic moments element specifically and moreover separated into their spin and orbital moments. It was first verified by Schütz *et al.* (1987). In the following decade it became an often used method for the characterization of magnetic materials. For the XMCD effect it is assumed that the spin dependent dichroism in the absorption process corresponds to the difference between the number of spin up and spin down holes of the conduction band, which gives the magnetic moment. For a maximum XMCD effect in the experiment, the photon angular momentum L_{ph} has to be collinear to the magnetization direction M. The dichroism is then given by the difference spectra of a measurement with the right–hand polarized light ($q = +1$, L_{ph} points in the direction of wavevector k) and the left–hand polarized light ($q = -1$, L_{ph} points in the direction of wavevector $-k$). The same effect can be achieved with a fixed light helicity, when the magnetization is switched in the opposite direction. The XMCD is described as a linear combination of the absorption of circular polarized light $I^{\mathrm{right}} - I^{\mathrm{left}} = I^+ - I^-$.

In figure 2.6 the XMCD process is schematically presented. The d-band is split into spin up and spin down bands. Firstly the absorption of circularly polarized x-ray photons leads to a spin polarization of the photoelectrons due to the spin orbit

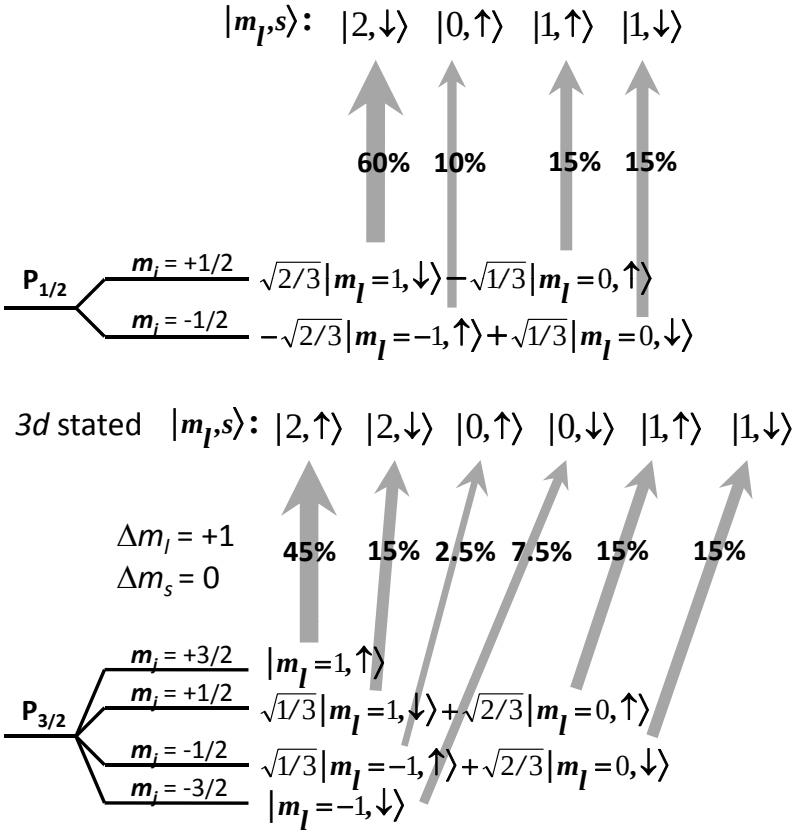

Figure 2.5: Absorption of a right–hand circular polarized photon by $p_{1/2}$ and $p_{3/2}$ multiplets. The excitation probability is given by Clebsch-Gordan coefficients.

coupling ($j = l \pm s$). In a second step the d valence band acts as a spin detector. At the L_3 edge ($j = l + s$) left hand circularly polarized x-rays mainly probe the unoccupied spin up d states with respect to the direction of the magnetization. The effect reverses at the L_2 edge due to the opposite sign of the spin–orbit coupling ($j = l - s$).

For $2p \rightarrow 3d$ transitions the magnetic moments can be calculated by applying the so called *XMCD sum rules* (equations 2.26 and 2.27) found by Thole *et al.* (1992) and Carra *et al.* (1993). These equations were modified by Chen *et al.* (1995).

$$m_{orb} = - \frac{4\int_{L_3+L_2}(\mu_+ - \mu_-)\,d\omega}{3\int_{L_3+L_2}(\mu_+ + \mu_-)\,d\omega}(10 - n_{3d}) \tag{2.26}$$

$$m_{spin} = - \frac{6\int_{L_3}(\mu_+ - \mu_-)\,d\omega - 4\int_{L_3+L_2}(\mu_+ - \mu_-)\,d\omega}{\int_{L_3+L_2}(\mu_+ + \mu_-)\,d\omega} \times (10 - n_{3d})\left(1 + \frac{7\langle T_z\rangle}{2\langle S_z\rangle}\right) \tag{2.27}$$

Here m_{orb} is the orbital magnetic moment and m_{spin} is the spin magnetic moment in units of μ_B/atom. The indices L_3 and L_2 of the integrals refer to the integration

over the whole L_3 and L_2 peaks. $(\mu_+ - \mu_-)$ is the XMCD spectrum and $(\mu_+ + \mu_-)$ is the sum of the XAS spectra excited with left and right circularly polarized light. n_{3d} is the number of $3d$ electrons in the corresponding ion. $\langle T_z \rangle$ is the ground state expectation value of the magnetic dipole term originating from the expectation value of the magnetic dipole operator and $\langle S_z \rangle$ is the corresponding spin operator. Usually for bulk cubic crystals $\frac{7\langle T_z \rangle}{2\langle S_z \rangle} \ll 1$ and can be neglected.

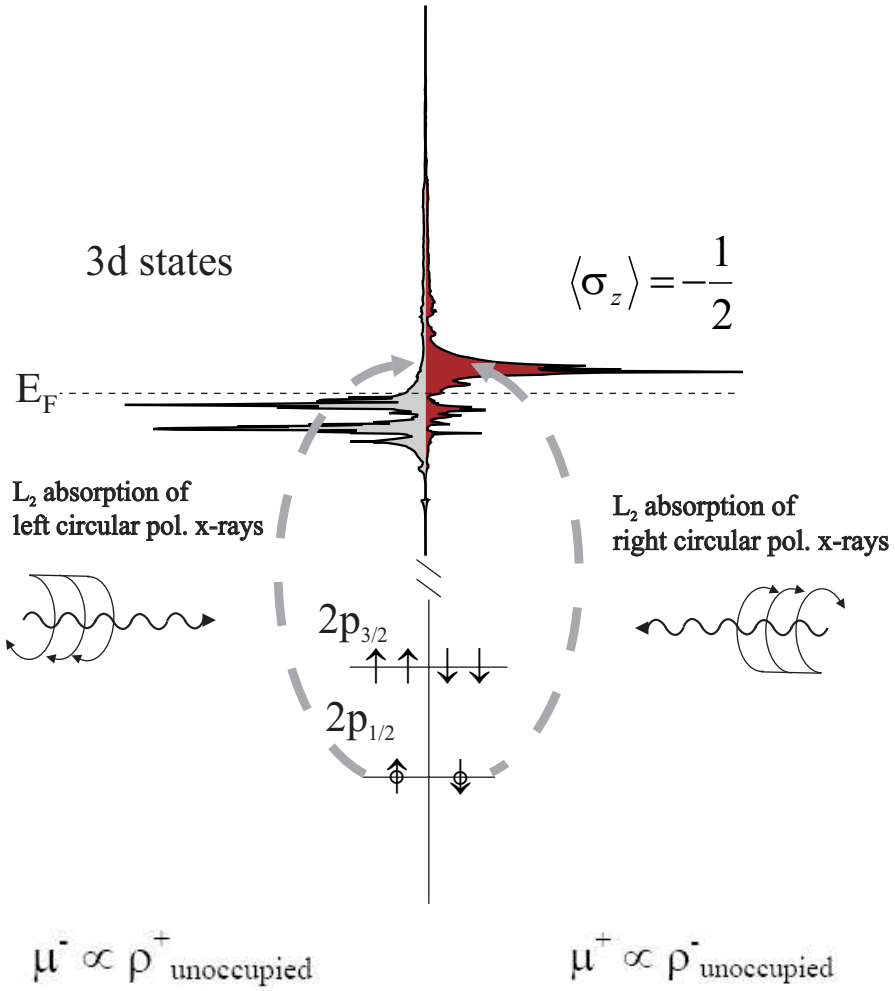

Figure 2.6: Schematic representation of the XMCD process in the one electron picture (Plogmann, 1999).

There were some simplifications made during the derivation of the sum rules. It is considered that the $2p \rightarrow 3d$ transitions take place between free atoms. Secondly the L_3 and L_2 edges should have a complete energetic separation for the purpose of getting exact results for the integrals. Problems occur for less–than–half–filled band of $3d$ transition metals. The sum rules can be used for the late $3d$ transition metal ions with a small deviation, but for the earlier transition metals a correction factor is needed to handle the mixing of the TM L_2 and L_3 edge. This factor was found by Teramura *et al.* (1996) for different valence states of Ni, Co, Fe and Mn. For the less

influenced Ni ions the factor is around 0.92, but for the Mn^{4+} ion a factor of around 0.59 was found. Without this correction the magnetic spin moments extracted from XMCD experiments by the sum rules are underestimated for early and intermediate transition metals.

A two–step model describes the XMCD effect (Schlachter and Wuilleumier, 1994). In the first step a photoelectron with a spin and an orbital momentum from a localized atomic inner shell is generated by circularly polarized light. In the second step, the $3d$ shell acts as a detector of the spin and the orbital momentum of this photoelectron. The amount of dichroism depends on three important parameters: the degree of circular polarization P_{circ}, the expectation value of the magnetic moment of the $3d$ shell $\langle m \rangle$ and the angle Θ between the directions of the photon angular momentum L_{ph} and the magnetic moment m. Then the XMCD intensity is casted to the following dependence:

$$I_{\mathrm{XMCD}} \propto P_{\mathrm{circ}} m L_{\mathrm{ph}} \propto P_{\mathrm{circ}} \langle m \rangle \cos\Theta \ . \tag{2.28}$$

With this dependence the effects of partly polarized light and experimental geometries deviating from the ideal case can be taken into account.

2.3.3 X-ray (Magnetic) Linear Dichroism (XMLD)

The x-ray absorption of linear polarized light changes with the geometry of the experiment. This gives a dichroic signal for different orientations of the polarization of the light. Two types of linear dichroism can be distinguished. The first is the x-ray natural linear dichroism (XNLD) which is also abbreviated with XLD. Here the polarization plane is either perpendicular or parallel to the crystal axis of a not magnetized single crystal. The second is the x-ray magnetic linear dichroism (XMLD) where the geometry is similar to the XNLD, but the magnetization of the sample is either perpendicular or parallel to the polarization plane. There is a complex angle dependence between magnetization, crystal axis and polarization plane, which is examined in detail by Arenholz *et al.* (2007) for Ni^{2+} $L_{2,3}$ XMLD in cubic lattices.

For linear polarized light the electric field vector **E** acts like a searchlight for the occupation of orbitals because the transition intensity of the absorption process is directly proportional to the number of empty valence states in the direction of **E**. That means that orbitals lying perpendicular to the electric field vector are not excited. For spherical orbitals, no natural linear dichroism appears. For example the split $3d$ states, e_g and t_{2g}, of an octahedral crystal field are spherical, but if the suborbitals d_{xy}, d_{xz} and d_{yz} (t_{2g}) or $d_{x^2-y^2}$ and $d_{z^2-r^2}$ (e_g) are differently occupied, a natural linear dichroism will appear. With this technique an orbital ordering can be observed. This was made for example by Kuepper *et al.* (2005) for the CMR manganite $La_{7/8}Sr_{1/8}MnO_3$.

For the magnetic linear dichroism the sample is magnetized by an external magnetic field. In this case the charge density is distorted and elongated along the spin axis. This is due to spin–orbit interaction, whereby the atomic spins are axially aligned by the exchange interaction. This effect is present for ferromagnetic, ferrimagnetic and antiferromagnetic configuration. This is the advantage of XMLD with respect to XMCD. The XMLD effect does not vanish for antiferromagnetic coupling.

The XMLD spectra can be described as a combination of the absorption of circularly and linear polarized photons $I^{|||} - I^{\perp} = I^0 - (I^+ + I^-)/2$.

It is important to note that the natural linear dichroism is additionally present in the magnetic linear dichroism experiment. Both linear dichroism effects are due to a charge asymmetry. A detailed theoretical description of all (magnetic) x-ray absorption spectroscopies can be found in a book of Stöhr and Siegmann (2006).

2.4 X-ray Emission Spectroscopy (XES)

The basic effect of the x-ray emission spectroscopy (XES) is the recombination of a previously created core hole, as shown in figure 2.7.

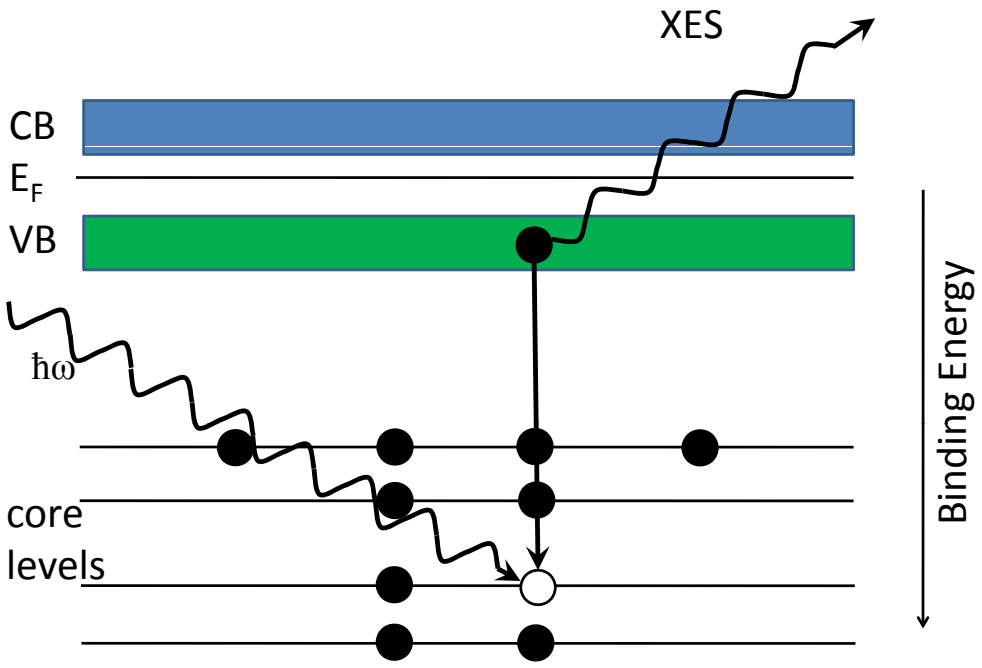

Figure 2.7: Scheme of x-ray emission spectroscopy.

The system from which a core electron was ejected, tries to get in a state of minimum energy. So the hole in the core level will be filled with an electron of an energetically higher lying state, e.g., from the valence band. The energy which the recombining electron loses can be send out as a photon. The energy of the emitted light is:

$$E_{em} = E_{B,eff} - E_{B,VB} \ . \tag{2.29}$$

Here E_{em} is the energy of the emitted photon, $E_{B,eff}$ is the effective binding energy of the hole and $E_{B,VB}$ is the binding energy of the electron in the valence band.

This emitted light can be detected for example by a CCD camera. So one can measure the intensity of the emitted light. The x-ray emission is dominated by dipole selection rules: $\Delta l = \pm 1$ and $\Delta j = \pm 1$; 0 if one only considers the electric dipole vector of the radiation. The probability of ion relaxation via dipolar emission is much larger than the probability corresponding to the electric quadrupoles, which can be often neglected, particularly in the case of *normal x-ray emission spectroscopy* (NXES). With XES one can probe the partial density of occupied states (pDOS). It is partial because the excitation energy depends on the element and it is dominated by the dipole selection rules. This means that it is a site specific and symmetry specific technique. Occupied states are probed because the recombining electrons are coming from occupied states of the valence band. An important advantage of this method is that it is not as surface sensitive as XAS or XPS, because the mean free path of photons is longer than that of electrons. In figure 2.8 the emission lines are presented, while the same dipole selection rules as for the absorption process are applied.

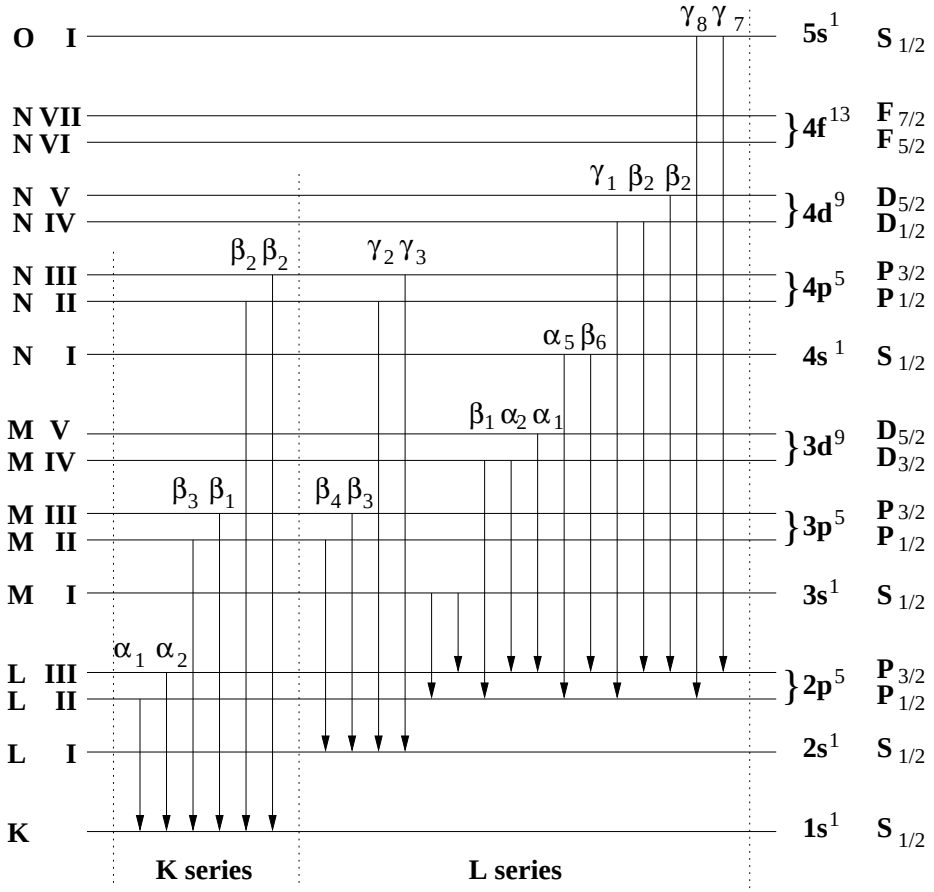

Figure 2.8: Allowed dipole transitions in x-ray emission of the K and L series (Brundle and Baker, 1979).

In the *Resonant X-ray Emission Spectroscopy* (RXES) the excitation energy is close of the binding energy of the core level. This spectroscopy is divided in two parts. In the first process, namely *Resonant Elastic X-ray Scattering* (REXS), the

excited electron recombines with the core hole. Here the emitted energy is equal to the incident energy, but due to small excitations at the Fermi level some energy–loss features can appear which remain in constant distance to the elastic peak while the excitation energy is tuned. The second process is the *Resonant Inelastic X-ray Scattering* (RIXS) where the exited electron stays in the conduction band, and the core hole is filled with an electron of the valence band. Here the conservation of the impulse leads to the possibility of a band mapping, as made by citetsok04.

2.5 Effects in X-ray and Electron Spectroscopy

2.5.1 Double Exchange and Superexchange

For transition metal oxides broadly known are two important indirect magnetic exchange mechanisms, namely the double exchange and the superexchange, which favour ferromagnetic and antiferromagnetic coupling, respectively. These interactions are named in analogy with the direct exchange interaction, which is normally a short–range one.

In figure 2.9 a scheme of the superexchange is depicted. This interaction was firstly mentioned by Kramers (1934). The theory of superexchange was developed by Anderson (1950). For the superexchange process the metal atoms are assumed to

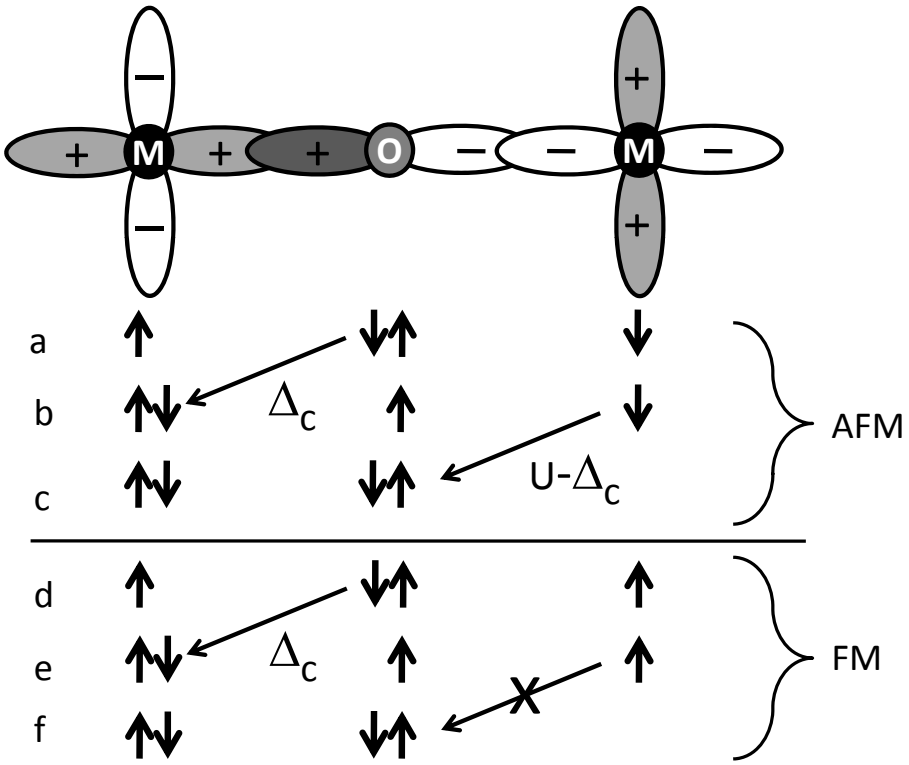

Figure 2.9: Scheme of the superexchange interaction as described by Stöhr and Siegmann (2006).

have unpaired electrons. One electron from the intermediate nonmagnetic ligand is transferred to one metal atom using the charge transfer energy Δ_C (step a–b and d–e in figure 2.9). In the next step the unpaired electron of the other metal atom can be transferred to the ligand hole using the energy $U - \Delta_C$ (see step b–c). This is only possible if spin of the unpaired electrons from the metal atoms in of opposite sign (see step e–f). Therefore the superexchange leads to antiferromagnetic coupling.

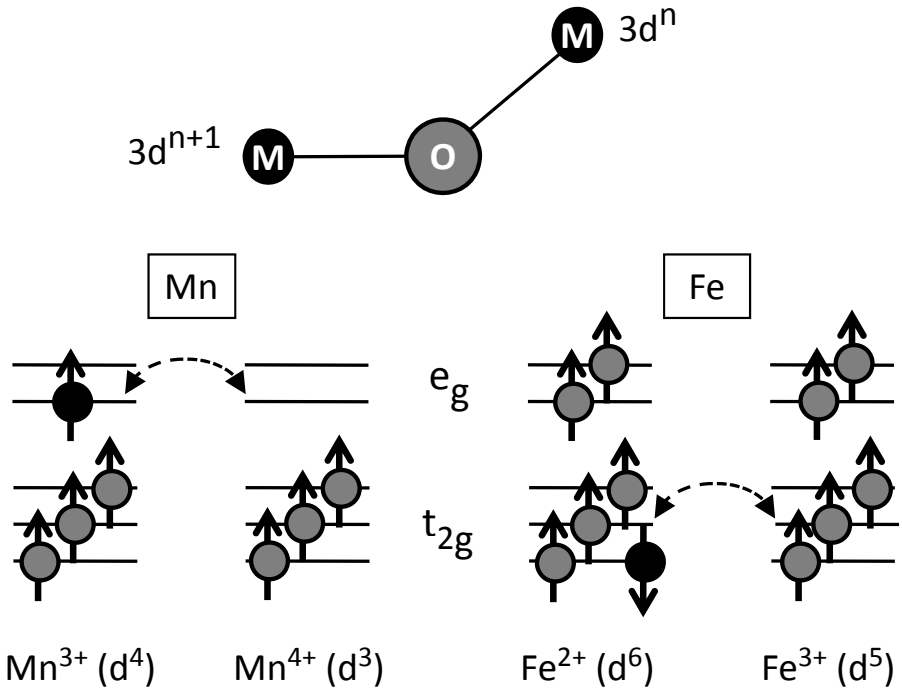

Figure 2.10: Scheme of the double exchange interaction as described by Stöhr and Siegmann (2006).

In figure 2.10 the double exchange process is depicted. This effect was introduced by Zener (1951) to explain magnetoconductive properties of mixed–valent solids. Important for this interaction is that the valence state of the metal atoms differs by one. In this example $Mn^{3+/4+}$ and $Fe^{2+/3+}$ are used. The metal ion with higher valence state gets an electron from the intermediate ligand which fills the orbitals according to the Hund's rule. Then one electron of the other metal ion is transferred to the ligand hole. The initial energetic state of the system is equal to the final energetic state. The resulting coupling is ferromagnetic.

The advantage of the superexchange is that the valence states of the metal atoms have not to differ by one, but the advantage of the double exchange is that no energy is needed to transfer an electron.

2.5.2 Spin-orbit Coupling

The interaction between the spin and the angular momentum of an electron is called *spin–orbit coupling*. The sum of the electronic spin s and the angular momentum l is the total angular momentum j of the electron ($j = l + s$). Here $s = \pm 1/2$ and

$l = 0, 1, 2, \ldots$. Hence every core level line is a doublet because of two possible cases $j = l + s$ or $j = l - s$. Only for $l = 0$ there is a singlet because j cannot be negative. The states are named after the main quantum number n, the angular momentum l and the total angular momentum j, whereby s, p, d, f stand for $l = 0, 1, 2, 3$, respectively. A level with $l = 1$, $s = +1/2$ and $n = 2$ is denoted as $2p_{3/2}$. For an s level ($l = 0$) it is not necessary to indicate the total angular momentum because in every case $j = 1/2$. Hence an s level with $n = 3$ is called $3s$.

The relative intensity of the two levels of a doublet is given by:

$$\frac{I_{(l+1/2)}}{I_{(l-1/2)}} = \frac{l+1}{l} \tag{2.30}$$

For p levels ($l = 1$) the relative intensities are $I_{3/2}/I_{1/2} = 2/1$. The splitting of the doublets increases with the atomic number for fixed main quantum number and total angular momentum.

2.5.3 Multiplet Splitting

Beside the spin orbit coupling one can observe another interaction between spins for systems with unpaired electrons in the valence levels. This interaction is called multiplet (exchange) splitting. During the photoemission process from $3s$ core levels of transition metal compounds, the spin (s=1/2) of the generated hole in the core level can interact with the total spin of the valence electrons (S). This coupling is antiparallel or parallel. Hence there is another splitting in addition to the spin–orbit splitting. According to the van Vleck theorem (van Vleck, 1934) the exchange splitting (ΔE_s) can be written as:

$$\Delta E_s = \frac{2s+1}{2l+1} G^2(3s, 3d) \ . \tag{2.31}$$

$G^2(3s, 3d)$ is the Slater exchange integral and l is the orbital quantum number (l=2). The binding energy of the state with spin ($S + 1/2$) is lower than that of the state with spin ($S - 1/2$). The intensity ratio between this two peaks is:

$$\frac{I_{S+1/2}}{I_{S-1/2}} = \frac{S+1}{S} \ . \tag{2.32}$$

Fadley and Shirley (1970) found that there are spectra for which the van Vleck theorem is not fulfilled. The intensity ratio (equation 2.32) was about two times smaller than expected. Bagus *et al.* (1973) associated this to intraatomic near-degeneracy correlation effects. It turned out that this deviation from equation 2.32 is due to a satellite in this energy region, which is a contribution from shakeup and plasmon loss processes (Uhlenbrock, 1994; Sangaletti *et al.*, 2000). Nowadays the treatment of the $3s$ multiplet splitting is based upon full multiplet calculations (Sangaletti *et al.*, 1995). For the other core levels ($l \neq 0$), the multiplet splitting is more complex because an additional spin-orbit splitting occurs in the spectra.

2.5.4 Chemical Shift

When an atom is bound to another atom, the binding energy does not only change for the valence electrons but also for the core electrons. This happens because of the deformation of the valence charge density and the resulting change of electric potentials. The energetic shift of the core electrons depends on the type of binding and the electronegativity of other atoms. Referring to benchmark measurements, one can characterize chemical bonding in the material under study. Theoretical calculations for the analysis of the chemical shift are difficult, because the influence of several factors cannot be determined correctly. In general the equation 2.14 is extended by two terms that describe the effective binding energy of the electrons if the atom is participating in a chemical bonding. The resulting equation becomes:

$$E_{B,eff} = E_B(\text{atom}) + \Delta(E_{chem} + E_{Mad}) \ . \tag{2.33}$$

$\Delta E_{chem} = K\, q_A$ denotes the shift of charge in atom A relating to a reference. q_A is the difference of the valence state to the reference and K describes the interaction of valence electrons with the core electrons. The influence of the other atoms of the molecule or the bulk is considered by the Madelung term E_{Mad}. This is the sum of effective charge q_B divided by the distance r_{AB} to the atom A where $A \neq B$. The whole influence on the effective binding energy $E_{B,eff}$ can be expressed as:

$$E_{B,eff} = E_B(atom) + K\, q_A + \sum_{B \neq A} \left(\frac{q_B}{r_{AB}} \right) \tag{2.34}$$

Equation 2.34 takes only electrostatic considerations into account. In practice K is an empirical parameter.

2.5.5 Satellites

During the photoemission process the atom has $N - 1$ electrons. There is an interaction between this relaxed states and the photoelectron. Because of this interaction, in addition to the main line, other lines (so–called satellites) appear in the XPS spectra. Satellites which are due to interatomic excitations are called extrinsic satellites. Intrinsic satellites originate from intraatomic relaxations.

During the photoemission process a second electron of the atom can be excited to higher energy levels bound to this atom. This is called a shake-up process. If the second electron is released into the continuum this is called a shake-off process.

For many transition metal oxides additional peaks appear because of charge transfer. These charge transfer satellites are due to a transfer of one electron from the ligand $2p$ to the metal $3d$ shell: $3d^n L \rightarrow 3d^{n+1} L^{-1}$. For this transfer the energy Δ (see equation 2.35) is required.

$$\Delta = E\left(3d^{n+1}L^{-1}\right) - E\left(3d^n L\right) \ . \tag{2.35}$$

2.5.6 Auger Electrons

After the photoemission process, a hole in the core level is left behind. An electron with lower binding energy can decay in this hole by exciting another electron into the

continuum. This second photoelectron is called Auger electron. It has a lower kinetic energy than the first photoelectron, whereby the kinetic energy of the Auger electron is independent of the incoming photon energy and, instead, is determined exclusively by a differences between the involved electronic states. The timescale of this two–electron process is in the range of 10^{-14} seconds (Auger, 1925). Equation 2.36 gives the approximated kinetic energy of the Auger electron. Relaxation effects and the reconfiguration of the excited state are not taken into account.

$$E(\mathrm{KL_1L_{23}}) \approx E(\mathrm{K}) - E(\mathrm{L_1}) - E(\mathrm{L_{23}}) - \Phi \ . \tag{2.36}$$

The Auger electrons are labelled like (XYZ) after the shell the first photoelectron was removed from (X), the shell an electron is decaying from (Y) and the shell in which the Auger electron was before its excitation (Z). For example an Auger electron is called KL_1L_{23} when an electron of the K shell ($1s$ level) was removed, an electron of the L_1 ($2s$) level recombines with the hole in the K shell and the secondly excited electron comes from the L_{23} ($2p_{1/2}$ or $2p_{3/2}$) level.

The Auger lines appear in the XPS measurements and can make the interpretation of the photoelectron peaks more difficult. This difficulty can be resolved by using different excitation energies (e.g. Al K_α and Mg K_α), because the kinetic energy of photoelectrons only, and not of Auger electrons, changes with the excitation energy. Hence one can identify the hindering Auger lines overlapping with the XPS binding energy spectrum. With the right choice of x-ray source, one can get rid of hindering Auger lines.

2.6 Experimental Details

2.6.1 The Photoelectron Spectrometer PHI 5600ci

The XPS measurements of the present work were performed with a PHI 5600ci multitechnique spectrometer produced by the Perkin Elmer Cooperation. In the figure 2.11 a schematic diagram of the PHI 5600ci multitechnique spectrometer is shown. Furthermore a preparation chamber is necessary for experiments with in situ prepared samples. This chamber was made by the fine mechanical workshop of the department of physics. In the preparation chamber one can integrate a wobblestick equipped with a diamond file in order to clean the samples. Alternatively one can cleave the samples in the vacuum. This allows measurements on very clean surfaces which is necessary because XPS is a surface sensitive technique and the samples should not be contaminated with particles. Another point is that the ultra high vacuum (UHV) is required so that the electrons are not scattered on their way from the sample to the analyser. The vacuum is achieved by rotation pumps down to a pressure at which turbomolecular pumps can work, resulting in the pressure of about 1×10^{-8} mbar. For better vacuum conditions, 1×10^{-9} mbar, an ion getter pump and a titanium sublimation pump are used. Beside scraping and fracturing there is another method to get clean surfaces. One can sputter the samples in the mainchamber with an ion gun. The maximum acceleration voltage is 4.5 kV. Usually argon ions are used for the sputtering. It is important to know that sputtering is a good method to

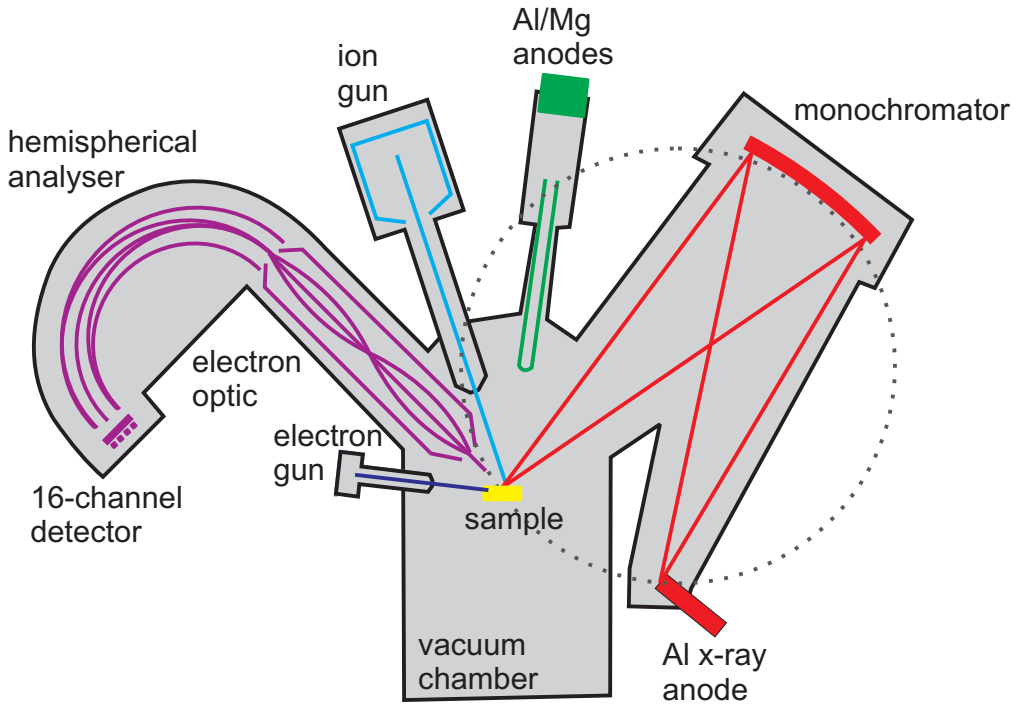

Figure 2.11: Schematic diagram of the PHI 5600ci multitechnique spectrometer.

clean metallic surfaces, but the structure of many compounds, especially oxides, can be damaged very easily. Already a short time of sputtering with a low acceleration voltage can cause surface damages which falsify the measurements: chemical bondings get broken and the stoichiometry on the surface may change. With an electron gun one can flood the sample with electrons, which can be tuned in kinetic energy and amount. This device allows the investigation of isolating samples by reducing charges at the surface.

There are two x-ray excitation sources. First there is a dual Mg/Al x-ray anode. For the Al K_α and the Mg K_α the radiation energies are 1486.6 eV and 1253.6 eV and the half widths for the unmonochromatized radiation are 0.85 eV and 0.7 eV, respectively. K_α radiation means that the emitted x-rays arise from the transition of an electron from the L shell to a hole in the K shell which was created during a photoemission process. The second excitation source is a single Al K_α anode which is used for most of the measurements. This K_α radiation is monochromatized with a quartz crystal to a half width of 0.3 eV, the monochromatization being achieved on the basis of the Bragg equation $n\lambda = 2d \sin\theta$. Monochromator, source and sample are placed on a Rowland circle. The Rowland circle has half of the diameter of the grating circle, whereby the center of the grating circle and the grating itself are placed on the Rowland circle. In order to align the compound in question into the focus of the x-ray source, the sample and the grating should be arranged on the Rowland circle. The photo electrons are analysed by an 11–inch hemispherical analyser. The electrons are focused by an electronic lens system, then the kinetic energy of the electrons is reduced to the pass energy E_p to guarantee a constant absolute resolution

for the whole spectrum. In the constant analyser transmission (CAT) mode only electrons with the energy $E_p \pm \Delta E$ can pass the analyser. ΔE indicates the absolute resolution: a smaller pass energy means a better absolute resolution of the spectrum, but the intensity of the signal is reduced.

2.6.2 Synchrotron Radiation

In order to perform XAS, XES, and RXES experiments one needs high intensity tuneable x-ray sources. NXES experiments may also be performed by using strong electron excitation sources, the x-rays created by the Bremsstrahlung are characteristic for the anode material, and the emission from the sample may be analysed by different types of crystal monochromators and multichannel detectors. However, this technique is limited by the fact that the major part of the kinetic energy of the exciting electrons is dissipated as heat rather than x-ray photon flux. State of the art XAS and (R)XES are usually performed with the high brilliant and tuneable light produced at synchrotron radiation facilities (Attwood, 1999).

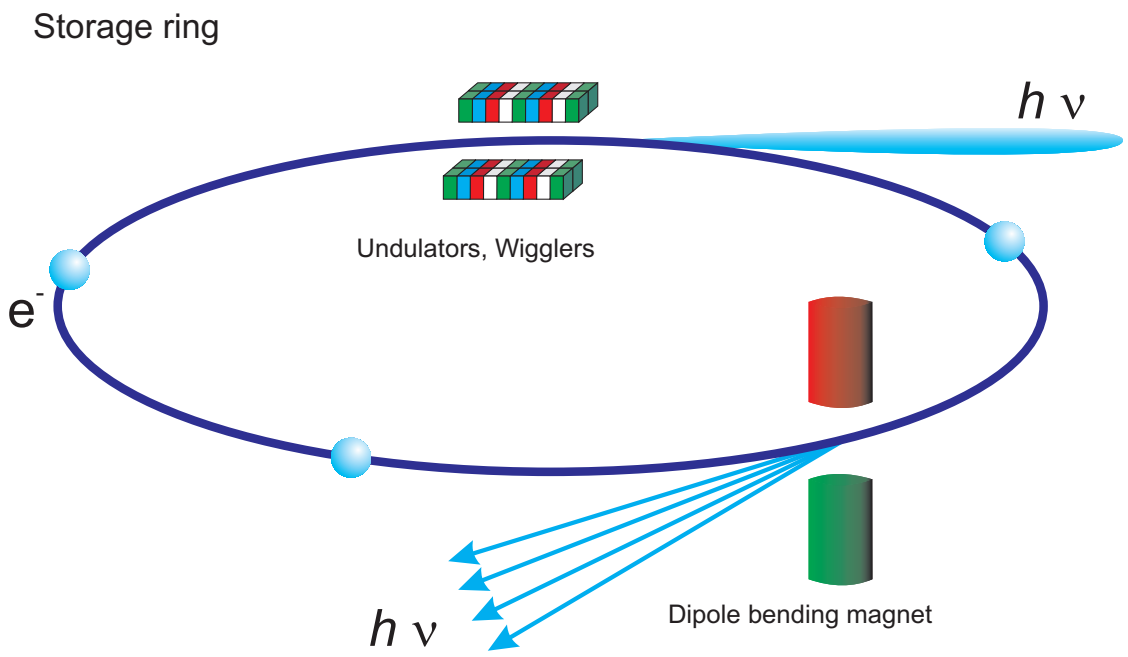

Figure 2.12: Schematic plot of a storage ring with different insertion devices: a bending magnet and an undulator.

2.6.3 Storage Ring and Insertion Devices

Synchrotron radiation is produced by accelerating electrons to almost the speed of light, because at relativistic velocities charged particles emit electromagnetic radiation in form of a narrow intense cone tangentially to the path of the particles. The electrons with nearly speed of light are forced by a series of magnets into a circular path in

the so called *storage ring*. The energy loss of the electrons, which is due to the emitted radiation, can be compensated by using an oscillating electric field in a *radio frequency* cavity, which is placed on the circle of the storage ring. This device is also forming bunches of electrons. Different types of magnet structures are available to bend the electron beam and subsequently to deviate the synchrotron radiation into the beamlines and experiments which are tangentially placed to the storage ring. The two most common insertion devices are the *bending magnets* and the *undulators*. Figure 2.12 shows a schematic plot of a storage ring and the two different types of insertion devices.

A dipole bending magnet simply bends the electrons in a single curved trajectory, whereby a rather narrow cone of radiation is produced. Its spectrum is continuous over a wide energy range, e.g. 100-1000 eV. In contrast to that, an undulator comprises alternating strong permanent magnets of opposite polarity. The electrons oscillate through this periodic magnetic structure, and at each pole coherent x-ray pulses are emitted by the oscillating electrons, which leads to constructive interference. The overall emitted radiation is a very intense and narrow cone with small angular and spectral widths (the latter usually ranging over a region of a few electron volts). Thus, the undulator spectrum consists of sharp peaks, called harmonics. The desired energy for the experiment can be chosen by varying the magnetic field strength between the poles. This is realized by changing the distance, or gap, between the upper and lower row of permanent magnets. Such a setup of an upper and lower row of permanent magnets leads to an almost 100% linearly and horizontally polarization. In order to perform experiments in dependence of the polarized radiation, especially if circular polarized radiation is required, a combination of two undulators can be applied.

In contrast to a standard planar undulator, the so called APPLE-type elliptical polarizing insertion device comprises horizontally separated magnet rows (see figure 2.13). The shifting of these rows produces a helical field at the position of the electron beam, causing an elliptical or circular trajectory. Consequently, elliptically or circularly polarized radiation is emitted. To change the polarization while staying at a fixed photon energy, both gap and shift have to be varied.

2.6.4 Beamline and Endstation

After the radiation has been generated by the insertion device, it has to be guided to the experiment. Firstly the desired excitation energy has to be chosen. In case of an undulator this is already done by choosing the right gap, but further monochromatization is achieved by using a series of high precision optical elements, like monochromators. In order to reflect the x-rays, these gratings have to be aligned in very grazing incidence angles. For the XAS and (R)XES experiments performed in this work, two different types of x-ray monochromators have been used, the plane grating monochromator (PGM) and the spherical grating monochromator (SGM) (Peatman, 1997). The monochromator of a beamline is usually followed by a further exit slit and a refocusing unit which focuses the incoming light onto the sample surface. In figure 2.14 a typical beamline layout is presented.

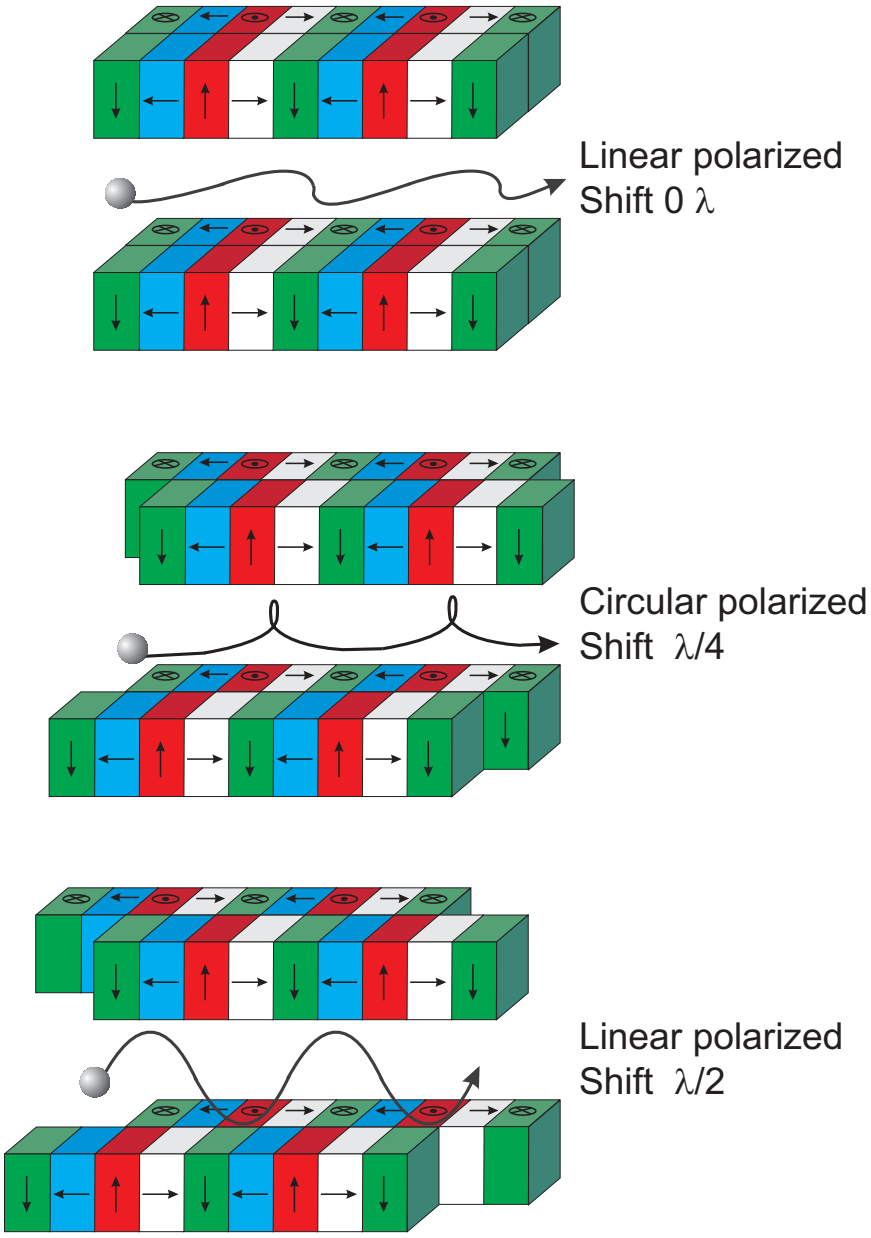

Figure 2.13: Schematic drawing of an APPLE insertion device at different settings. Upper panel: linear mode without shift (linearly horizontally polarised light). Middle panel: circular mode. The shift ($\lambda/4$) is set to the position with equal amplitudes of the horizontal and vertical magnetic fields (quarter period of the magnetic structure). Lower panel: linear mode with shift set to half period ($\lambda/2$) (linearly vertically polarised light) of the magnetic structure. Adapted from (www.hmi.de/bereiche/SF/SF2/arbeitsg/bessy/sf204ab.html).

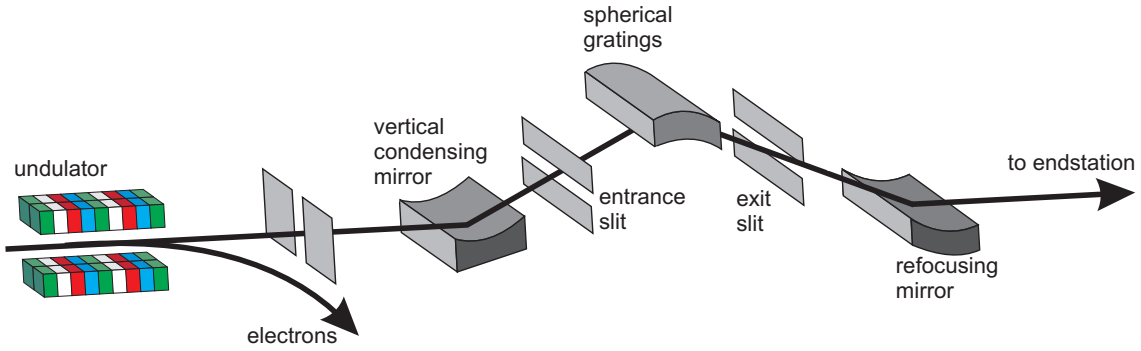

Figure 2.14: Typical example of an undulator beamline layout: the beamline 8.0.1 at the Advanced Light Source (ALS) at the Lawrence Berkeley Lab, Berkeley, USA.

During this work, several synchrotron facilities with different beamlines and endstation were visited. At the synchrotron facility *Advanced Light Source* (ALS), Berkeley, the beamlines 4.0.2 (http://www-als.lbl.gov/als/techspecs/bl4.0.2.html) and 8.0.1 (http://www-als.lbl.gov/als/techspecs/bl8.0.1.html) were used. The *Soft X-ray Fluorescence* (SXF) of the University of Tennessee in Knoxville and the Tulane University in New Orleans (Jia *et al.*, 1995) endstation of beamline 8.0.1 provides the R(XES) and XAS techniques with horizontally polarized light with excitation energies in the range from 65 eV to 1400 eV produced by an 50 mm period length undulator via a spherical 925 lines mm grating monochromator. Very special is the possibility to measure the absorption with an channeltron in *Total Fluorescence Yield* (TFY) additionally to the sample current measurement in *Total Electron Yield* (TEY). The emission is measured by four interchangeable gratings which are in a Rowland geometry with a multichannel plate detector. The spectral resolution of $E/\Delta E$ is set to around 1000-3000 by the entrance and exit slits around the grating.

The Beamline 4.0.2 (Young *et al.*, 2002) at the ALS has two interchangeable endstations and is based on a 50 mm period elliptical polarization undulator (EPU5) which produces linear polarized light continuously variable from horizontal to vertical and light in left and right circular or elliptical polarization in the energy range of 50 to 1900 eV. One endstation comprises a fluid helium cooled cryostat which can reach very low temperatures of around 2 K. This endstation provides XAS and XMCD techniques in TEY at relatively high magnetic fields of up to 6 T. TFY is also possible with a grating spectrometer. The other endstation provides also XAS and XMCD techniques, but in addition the XMLD technique as well. The latter becomes possible thanks to an octopole resistive magnet which can create a magnetic field of 0.8 T tuneable in every spatial direction (Arenholz and Prestemon, 2005).

Chapter 3

$La_{1-x}Sr_xMnO_3$

3.1 Introduction

Hole doped manganese oxides with the perovskite structure and formula unit $RE_{1-x}A_xMnO_3$, where RE and A denote a trivalent rare earth atom and a divalent atom, respectively, display a remarkably rich phase diagram (see figrue 1.2 section 1.1) as a function of temperature, magnetic field and doping that is due to the complex interplay of charge, spin, orbital and lattice degrees of freedom. This competition of different phases on the nanoscale has been the subject of many studies during the last decade (Millis, 1998; Salamon and Jaime, 2001; Chuang *et al.*, 2001). The variety of properties is often due to different behaviour of $3d$ electrons, which may be more or less localized, giving rise to intraatomic correlation effects of varying strength. Moreover they may either experience the orbital degeneracy compatible with a given crystal space group or lift this degeneracy, due to the Jahn-Teller distortion. These types of behaviour are to a large extent mediated by Mn $3d$ − O $2p$ hybridization, thus establishing a link to the chemistry of the compound in question. In a cubic crystal the Jahn-Teller distortion leads to a lowering of the symmetry and thus a splitting of the e_g level. Its occupation, influenced by doping and energetic position, strongly influences the hybridization between the Mn $3d$ and the O $2p$ states, which is crucial for understanding the family of colossal magnetoresistance compounds. In the last few years, studies of these compounds were stimulated by the discovery of colossal magnetoresistance (CMR), a huge negative change in the electrical resistance induced by an applied magnetic field (von Helmolt *et al.*, 1993; Jin *et al.*, 1994). This behaviour has been associated with half metallic ferromagnetism, meaning that one spin channel is metallic while the other is insulating (Pickett and Moodera, 2001; Park *et al.*, 1998). The spin polarized Mn $3d$ electrons are the charge carriers.

A number of spectroscopic techniques, mostly x-ray photoelectron spectroscopy (XPS) and x-ray absorption spectroscopy (XAS) have been applied to $La_{1-x}A_xMnO_3$ with A=Ca,Sr (Park *et al.*, 1996; Saitoh *et al.*, 1995). The band structure of $LaMnO_3$ and $La_{1-x}A_xMnO_3$ (A=Ca,Sr,Ba) has been also studied theoretically by several local spin density approximation (LSDA) studies (Saitoh *et al.*, 1995; Hamada *et al.*, 1995; Youn and Min, 1997; Ravindran *et al.*, 2002). The long-standing double exchange (DE) model provides a qualitatively correct description of the CMR effect

and is commonly adopted as the main ingredient to explain the physics of the manganites (Zener, 1951). However, it has been pointed out that the DE model alone cannot quantitatively account for the observed large magnetoresistance (Millis *et al.*, 1995, 1996). One author comes to the conclusion that the stabilization of the cubic phase is more important for ferromagnetism in hole doped compounds than the double exchange mechanism (Ravindran *et al.*, 2002). Several theoretical and experimental results suggest that more complex mechanisms such as short range ordered Jahn-Teller distortions (JTD) in the local environment of the magnetic atom, with resulting electron localization and polaron formation (Millis *et al.*, 1995, 1996; De Teresa *et al.*, 1997; Booth *et al.*, 1998; Louca *et al.*, 1997), charge and orbital ordering (Murakami *et al.*, 1998a,b) and phase separation (Moreo *et al.*, 1999; Mathur and Littlewood, 2003), are needed to quantitatively explain the properties of these materials.

3.2 Experimental Details

The $La_{1-x}Sr_xMnO_3$ ($x = 0.125$, 0.17 and 0.36) single crystals were grown at the Moscow State Steel and Alloys Institute, Russia, in the floating zone method. The structural quality and single phase nature were probed with x-ray diffraction (XRD).

The magnetization data were measured by M. Uhlarz of Forschungszentrum Dresden-Rossendorf by means of a Superconducting Quantum Interference Device (SQUID). The single crystals were measured along the crystallographic c direction. The measurements were performed field dependent at different temperatures from 1.8 K to 300 K.

The x-ray magnetic circular dichroism (XMCD) spectra were recorded at the beamline 4.0.2 at the ALS at the endstation with the octopole magnet (see section 2.6.4). The samples were cooled with liquid nitrogen. The magnetic field was constant at 0.7 T. The spectra were measured in TEY and in normal incidence along the crystallographic c axis of the samples.

3.3 Magnetometry

In the top panel of figure 3.1 the results for $La_{0.875}Sr_{0.125}MnO_3$ are presented. For temperatures of 150 K and below a steep decrease of the magnetization from 0 T to $\sim$0.4 T (M=2.75 μ_B/f.u.) appears. The saturation magnetization of $\sim$3.3 μ_B/f.u. at 1.8 K is reached at a field of approximately 2 T. For temperatures of 200 K and above the magnetization is much smaller and the saturation is not reached even at magnetic fields of 5 T.

In the second panel of figure 3.1 the results for $La_{0.83}Sr_{0.17}MnO_3$ are plotted. The increase of magnetization until 0.4 T at 1.8 K is steeper than for $La_{0.875}Sr_{0.125}MnO_3$ and the magnetization is 3.4 μ_B/f.u.. The saturation magnetization of $\sim 3.6\mu_B$/f.u. is reached at 5 T. Even at room temperature higher magnetic moments ($\sim 2\mu_B$/f.u.) can be reached than for the $La_{0.875}Sr_{0.125}MnO_3$ sample.

The results for $La_{0.64}Sr_{0.36}MnO_3$ in the lowest panel in figure 3.1 show the steepest increase of magnetization with the applied field until 0.4 T and at 1.8 K with a value

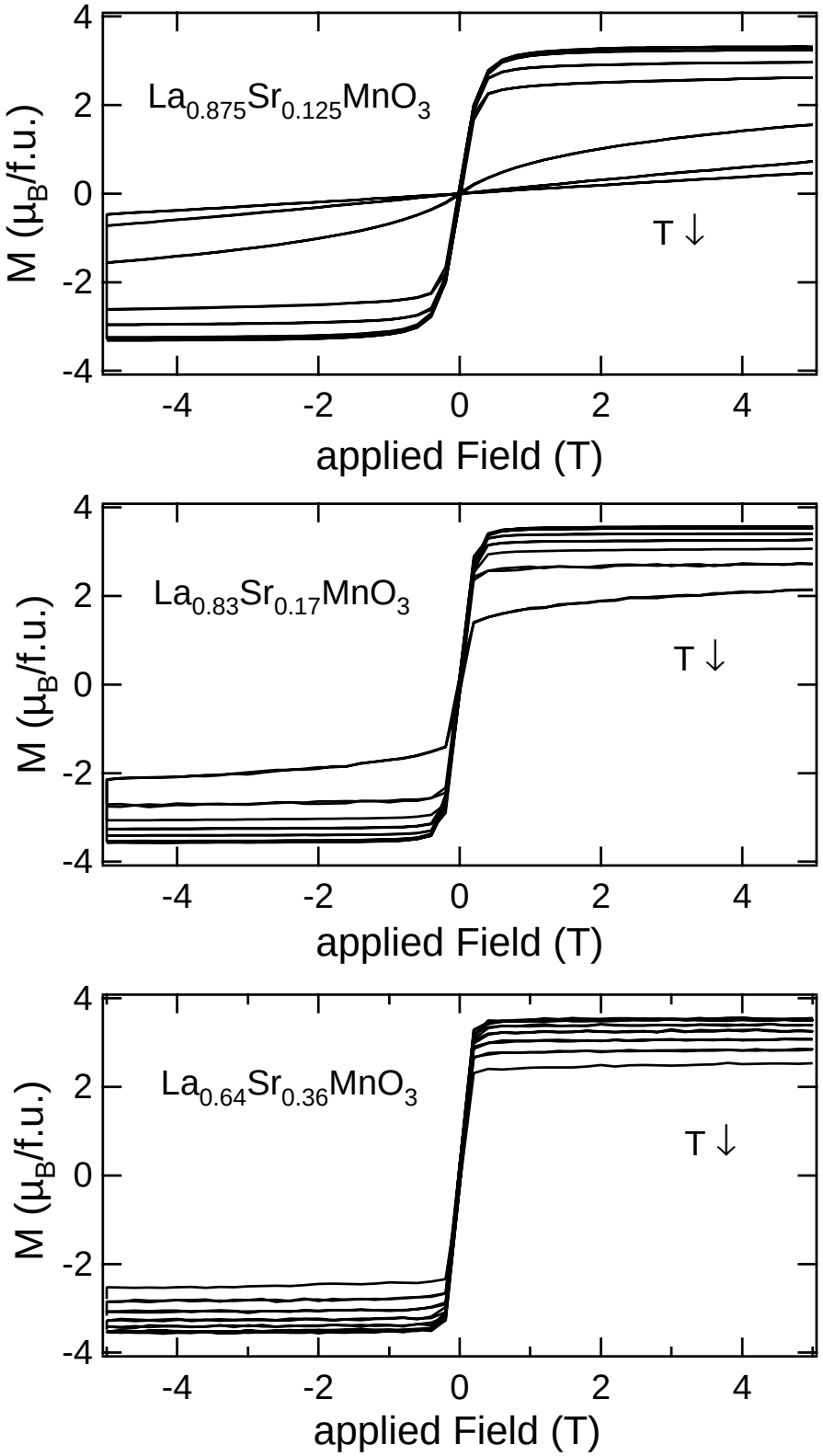

Figure 3.1: Magnetization measurements by means of SQUID of $La_{0.875}Sr_{0.125}MnO_3$ (upper panel), $La_{0.83}Sr_{0.17}MnO_3$ (middle panel) and $La_{0.64}Sr_{0.36}MnO_3$ (lower panel) single crystals. The magnetic field was tuned from -5 to 5 T. All samples were measured at the temperatures 1.8 K, 4.2 K, 30 K, 100 K, 150 K, 200 K, 250 K and 300 K.

of ∼3.4 μ_B/f.u., while the saturation magnetization is 3.5 μ_B/f.u.. Even at room temperature a relatively high saturation magnetization of ∼2.5μ_B/f.u. is reached with magnetic fields of 0.4 T.

In table 3.1 the total magnetic moment from SQUID measurements are presented at different temperatures and applied magnetic fields. In the first column the temperature and the applied magnetic field are most likely to the experimental parameters for the XMCD measurements from section 3.4, in the second column the maximal moment for lowest temperature and highest applied magnetic field are shown. In the last column the formal magnetic moment calculated in the assumption of La^{3+}, Sr^{2+} and O^{2-} formal charges and the maximal possible magnetization within the resulting Mn 3*d* configuration, is presented for comparison with experimental results.

Table 3.1: Total magnetic moments from SQUID measurements of $La_{1-x}Sr_xMnO_3$ compounds at different temperatures and applied magnetic fields. In the last column the theoretical magnetic moment from the formal valence state of manganese ions is presented.

	magnetic moment (μ_B/f.u.)		
	(T=100 K, B=0.8 T)	(T=1.8 K, B=5.0 T)	formal moment
$La_{0.875}Sr_{0.125}MnO_3$	3.06	3.31	3.875
$La_{0.83}Sr_{0.17}MnO_3$	3.37	3.57	3.83
$La_{0.64}Sr_{0.36}MnO_3$	3.38	3.53	3.64

3.4 XMCD and Multiplet Calculations

In this section the x-ray magnetic circular dichroism (XMCD) spectra are presented. With help of this technique and corresponding sum rules (see section 2.3.2) one can determine element specific spin and orbital magnetic moments. The experiments are compared with charge transfer multiplet calculations, in order to get an impression of the value of charge transfer in the $La_{1-x}Sr_xMnO_3$ compounds.

Table 3.2: Parameters for the charge transfer multiplet calculations at the *L*-edge of Mn in D_{4h} symmetry.

crystal field splitting	D_{4h} splitting		charge transfer	
10Dq	Ds	Dt	4+→3+	3+→2+
1.4 eV	0.01 eV	−0.01 eV	47.7%	29.0%

In the figures 3.2, 3.3 and 3.4, the XMCD results at a temperature of 80 K and an applied magnetic field of 0.7 T of $La_{0.875}Sr_{0.125}MnO_3$, $La_{0.83}Sr_{0.17}MnO_3$ and $La_{0.64}Sr_{0.36}MnO_3$, respectively, are presented in comparison with charge transfer multiplet calculations. Jahn-Teller distorted octahedral symmetry (D_{4h}) was used for the calculations. It should be noted that the negative Dt value corresponds to a compression of the octahedra in c direction. A detailed theoretical investigation of crystal field distorted electronic structures is given by Moffit and Ballhausen (1956). The parameters for the calculations are summarized in table 3.2. For all samples the

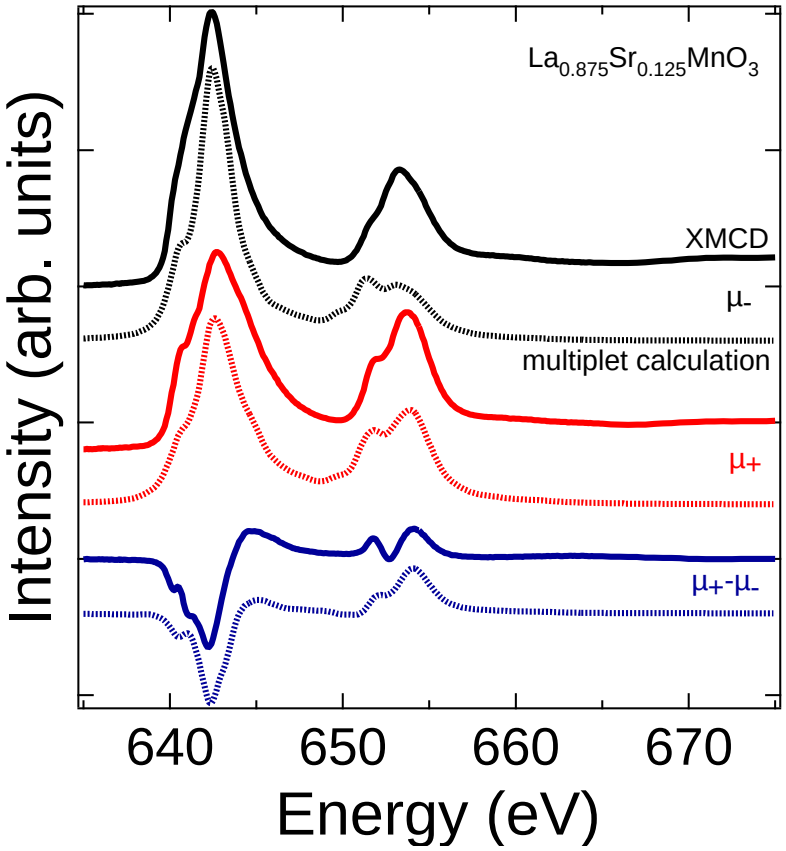

Figure 3.2: XMCD spectra of $La_{0.875}Sr_{0.125}MnO_3$ with 0.7 T applied magnetic field at 80 K in comparison with charge transfer multiplet calculations.

same parameters were used because of the very similar shape of the XMCD spectra, but the weights of the Mn^{3+} and Mn^{4+} within the calculations corresponds to the formal Mn valence derived from the amount of Sr doping. Charge transfer amounts of 47.7% and 29.0% for Mn^{4+} and Mn^{3+}, respectively (see table 3.2) gave the best result in comparison with the experiment.

The XMCD spectra comprise the Mn L_3-edge at ∼643 eV and the L_2-edge at ∼654 eV. The L_3-edge main feature at 642.5 eV has two shoulders to lower photon energy (641.5 eV and 640.5 eV). To higher photon energy a broad shoulder is present (∼645 eV). The main feature of the L_2-edge at 653.0 eV has one shoulder at 654.0 eV and another at 541.5 eV. A very small shoulder appears at 650.5 eV. This structure is very similar for all three samples, but the intensities are slightly different. The feature at 654.0 eV is higher for the sample with $x = 0.125$ than for the sample with $x = 0.36$. The shoulder at 640.5 eV is slightly bigger for the sample with $x = 0.36$ than for the other two.

The calculations generally are in very good agreement with the experiments, yet some notable differences remain. In the right handed circularly polarized spectra, the peak at 653.5 eV at the Mn L_2-edge is underestimated for all samples. This leads to a too small dip at ∼653 eV in the calculated XMCD spectra. The small prepeak of the

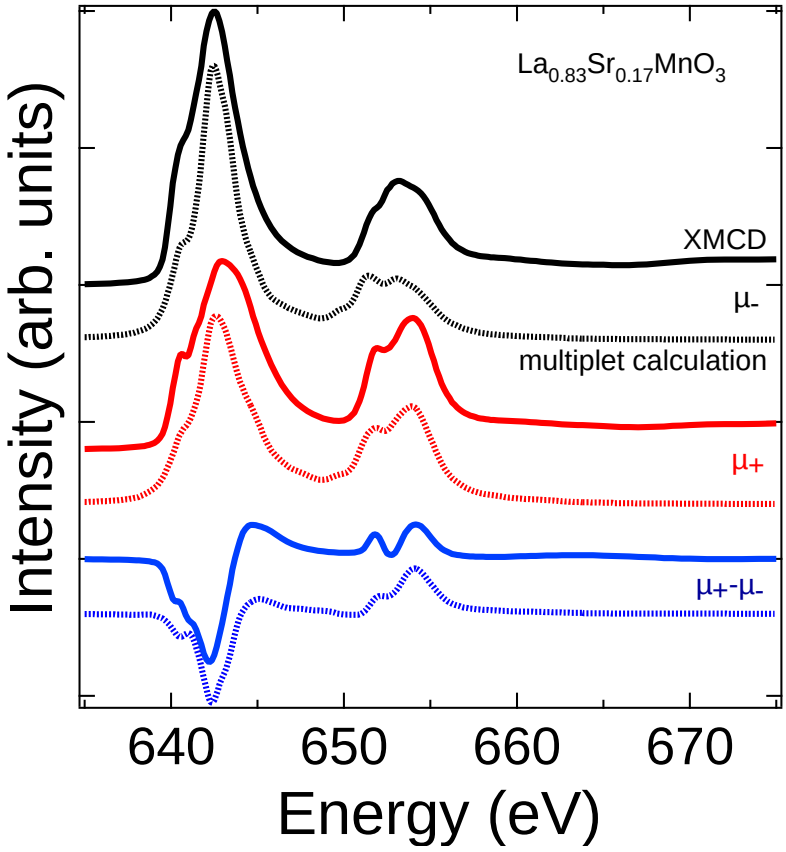

Figure 3.3: XMCD spectra of $La_{0.83}Sr_{0.17}MnO_3$ with 0.7 T applied magnetic field at 80 K in comparison with charge transfer multiplet calculations.

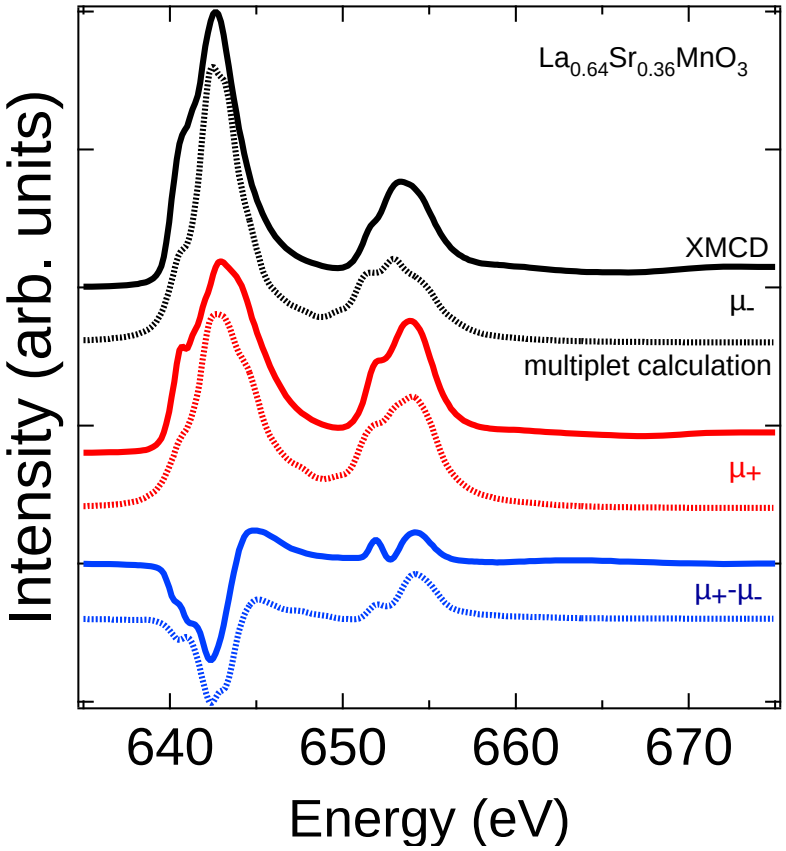

Figure 3.4: XMCD spectra of $La_{0.64}Sr_{0.36}MnO_3$ with 0.7 T applied magnetic field at 80 K in comparison with charge transfer multiplet calculations.

calculated Mn L_2-edge at 650 eV is hardly visible in the experiments. The prepeak structure of the Mn L_3-edge at 641 eV is not completely rendered by the calculation. The different mixing of Mn valence states has more influence on the structure in the calculations than in the experiment. Despite these differences, the calculation give a hint to some structural and electronic properties. The in the calculation included crystal field (1.4 eV) and Jahn-Teller distortion (Dt=-0.01 eV, Ds=0.01 eV) and the charge transfer amount (Mn^{4+}: 47.7%, Mn^{3+}: 29.0%) give the best agreement with the experiment.

For $La_{0.875}Sr_{0.125}MnO_3$ a series of XMCD spectra was measured with different temperatures from 80 K to 300 K. The applied magnetic field was 0.7 T during the whole experiment. The dichroic signals of the series are plotted in figure 3.5. From 180 K on, the dichroism becomes rapidly smaller and is nearly vanishing at 220 K. The shape of the dichroic signal is not changing. In table 3.3 the spin and orbital magnetic moments extracted from the sum rules (see section 2.3.2) are summarized for all samples. The orbital magnetic moments are very small in the whole temperature range, but do not vanish completely.

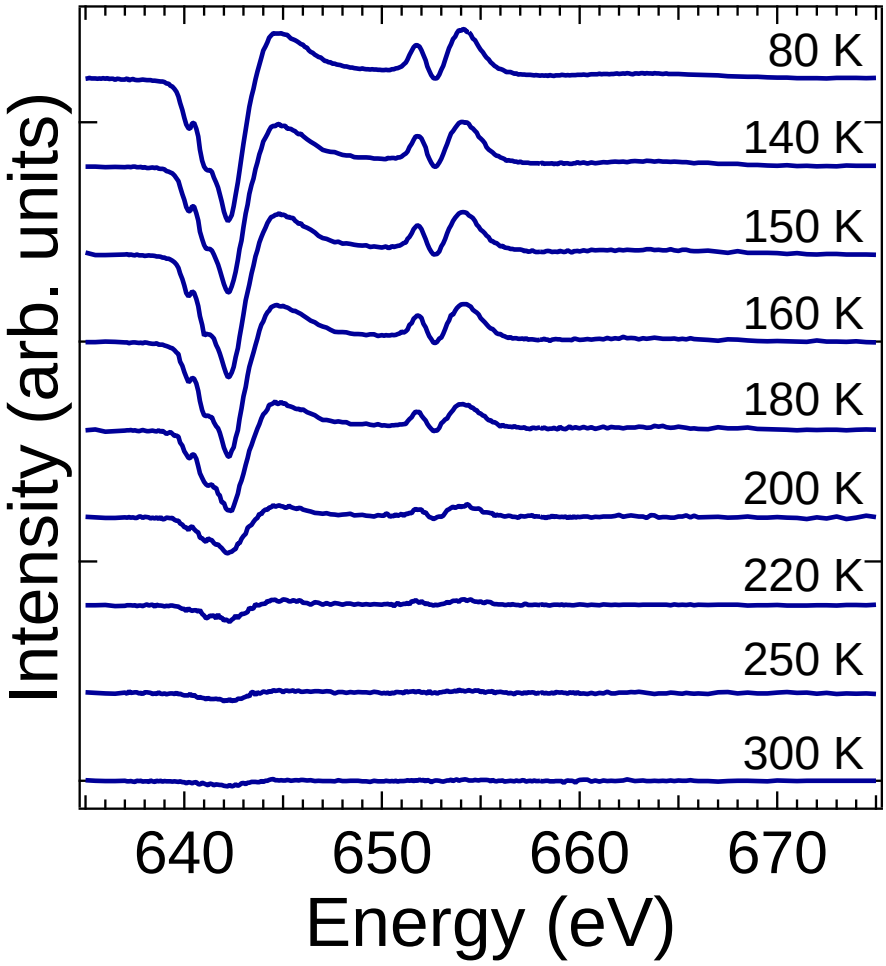

Figure 3.5: XMCD signals of $La_{0.875}Sr_{0.125}MnO_3$ with 0.7 T applied magnetic field at various temperatures from 80 K to 300 K.

Table 3.3: Spin and orbital magnetic moment of $La_{1-x}Sr_xMnO_3$ at various temperatures and at 0.7 T applied magnetic field, as extracted from XMCD spectra.

	temperature (K)	m_{spin} (μ_B)	m_{orb} (μ_B)
$La_{0.64}Sr_{0.36}MnO_3$	80	1.91	0.03
$La_{0.83}Sr_{0.17}MnO_3$	80	2.21	0.02
$La_{0.875}Sr_{0.125}MnO_3$	80	1.82	-0.019
	140	1.54	-0.023
	150	1.50	-0.003
	160	1.38	0.011
	180	0.91	0.034
	200	0.36	0.011
	220	0.18	0.003
	250	0.08	0.006
	300	0.05	0.019

3.5 Discussion

In figure 3.6 the magnetometry data is compared with the magnetic moments at the Mn atoms determined by XMCD and the sum rules. The magnetic spin moment determined by XMCD has to be multiplied with the factor found by Teramura *et al.* (1996) to get an excellent agreement between both methods. This factor for Mn L-edge XMCD is used successfully in literature to achieve the magnetic moment in a Mn–based magnetic molecule (Khanra *et al.*, 2008). The factors for Mn^{4+} and Mn^{2+} are 0.68 and 0.587, respectively. We have approximated the factor for Mn^{3+} as a linear combination of the factors for 2+ and 4+. This correction deals with the mixing of L_3 and L_2-edges due to a too small energy separation between them. This effect becomes more important for earlier transition metal ions (Cr,Mn,Fe) and is smaller for later transition metals (Co, Ni, Cu). We have also taken into account the charge transfer for Mn^{4+} and Mn^{3+} as used in the multiplet calculations in section 3.4.

In the top panel of figure 3.6 the magnetization of $La_{0.875}Sr_{0.125}MnO_3$ is shown for temperatures from 1.8 K to 300 K at 0.7 T and at 5 T. The magnetic moment at the Mn atoms determined from XCMD at temperatures from 80 K to 300 K at 0.7 T is also presented for comparison. With the corrections mentioned above, a perfect agreement between magnetometry and XMCD could be achieved. The Curie temperature T_C=188 K determined by Dabrowski *et al.* (1999) is also in agreement with our results. The comparison between magnetometry and XMCD at 80 K and 0.7 T for $La_{0.83}Sr_{0.17}MnO_3$ and $La_{0.64}Sr_{0.36}MnO_3$ is presented in figure 3.6 in the middle and bottom panel, respectively. Here also a very good agreement was achieved between magnetometry and XMCD by the corrections mentioned above. The Curie temperature of $La_{0.83}Sr_{0.17}MnO_3$ is T_C ≈280 K (Dabrowski *et al.*, 1999), but our measurements have a too short temperature range to determine the transition temperature. For higher Sr doping the Curie temperature is increasing and is for $La_{0.7}Sr_{0.3}MnO_3$ already at T_C=365 K (Mannella *et al.*, 2008). Therefore the transition temperature is out of range of our measurements for $La_{0.64}Sr_{0.36}MnO_3$.

The maximal magnetization is 3.31 μ_B/f.u. for our $La_{1-x}Sr_xMnO_3$ samples at a temperature of 1.8 K and an applied field of 5.0 T with Sr doping of $x = 0.125$. This value seems to be too small in comparison with theoretical value for a completely ferromagnetic orientation of the spins, which gives 3.875 μ_B/f.u. with 12.5% Mn^{4+} (3 μ_B) and 87.5% Mn^{3+} (4 μ_B). For $x = 0.17$ we found for the same conditions 3.57 μ_B/f.u. which is bigger than for $x = 0.125$, but again smaller than the theoretical value of 3.83 μ_B/f.u.. For $x = 0.36$ the experiment is with 3.53 μ_B/f.u. much closer to the theory with 3.64 μ_B/f.u.. The too small values could be explained with a too high oxygen content which leads to lower magnetic moments (Bukowski *et al.*, 2000), but also to a change of the Curie temperature. With 3.1 oxygen atoms/f.u. and ∼3.6 μ_B/Mn Bukowski *et al.* found T_C decreasing by more than 20 K for a sample with $x = 0.185$. In the case of our sample with $x = 0.17$ we would achieve a transition temperature T_C <260 K, which would be observed by our magnetization measurements (see figure 3.6 middle panel). Another explanation is given by Pinsard *et al.* (1997) finding a spin canting in a sample with $x = 0.125$ by means of neutron powder diffraction. This effect is explained with a strong coupling of Jahn-Teller distortion, ferromagnetic ordering and transport properties. For bigger Sr concentration

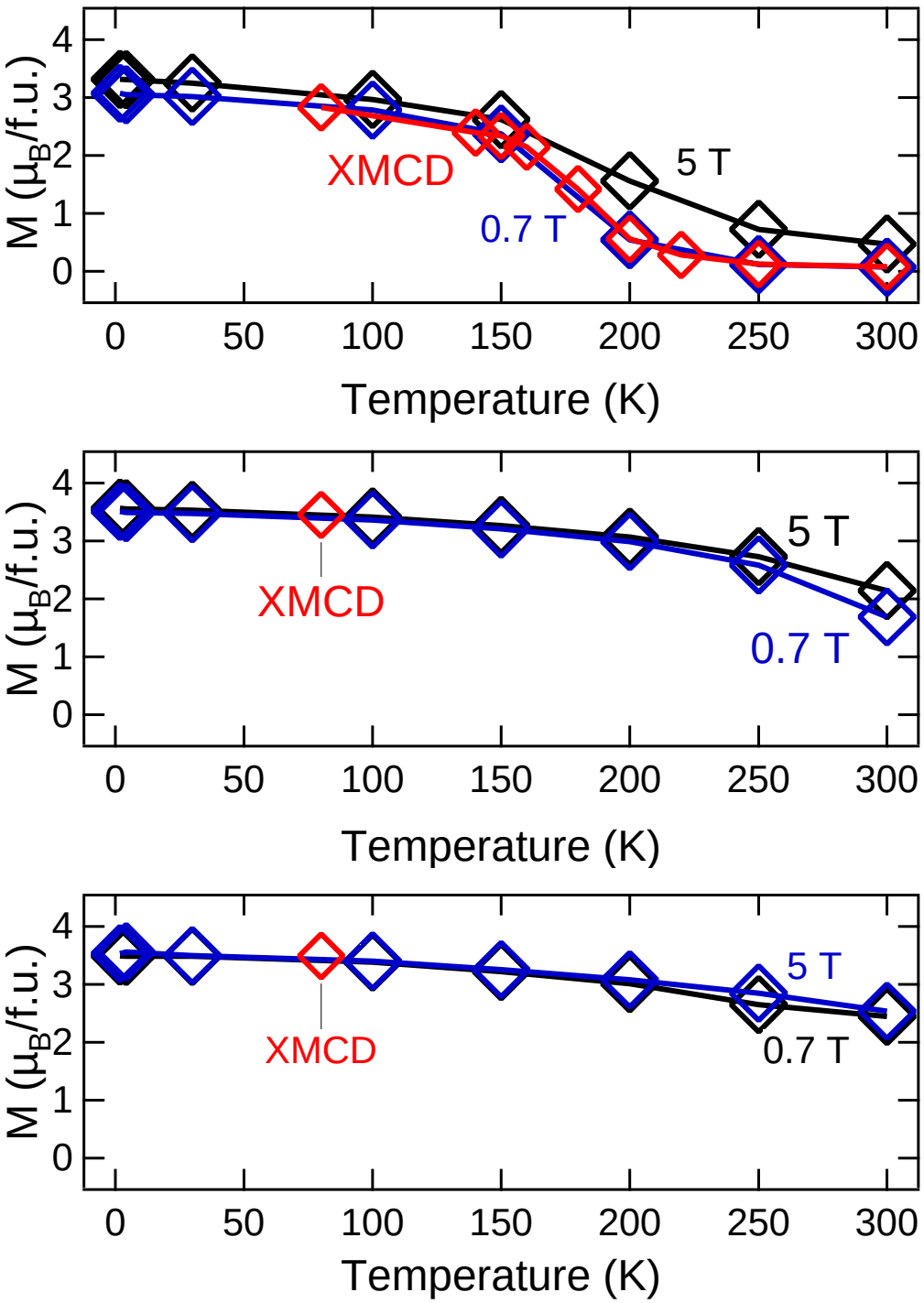

Figure 3.6: Comparison of magnetic moments of $La_{0.875}Sr_{0.125}MnO_3$ (upper panel), $La_{0.83}Sr_{0.17}MnO_3$ (middle panel) and $La_{0.64}Sr_{0.36}MnO_3$ (lower panel) determined by SQUID and XMCD. The XMCD results were corrected as found by Teramura *et al.* (1996).

the Jahn-Teller distortion becomes smaller and the difference of the magnetization to the theoretical completely ferromagnetic ordered magnetization disappears. Such a spin canting was also observed by neutron powder diffraction by Xiong *et al.* (1999) in this Sr concentration range. They found the angle between spin and *c*-axis for $x = 0.11$ to be $\sim 77°$. For $x = 0.165$ an angle of $\sim 40°$ and for $x = 0.185$ an angle of $\sim 15°$ were determined. Our samples with low Sr concentration are in the range of the coupling between structural and magnetic properties ($0.11 \leq x \leq 0.185$) and the canted spin configuration leads to lower magnetizations than expected for a completely ferromagnetic spin orientation aligned parallel to the applied magnetic field. The resulting spin canting in our samples is $\sim 31°$ for $x = 0.125$ and $\sim 21°$ for $x = 0.17$. The angles from our results are somewhat smaller than those determined by neutron powder diffraction. This is due to the applied magnetic field in our measurements which aligns the magnetic moment in the direction of the magnetic field.

For $La_{1-x}Sr_xMnO_3$ with $x = 0.3$ to 0.4 Mannella *et al.* (2008) found a ~ 200 K wide temperature hysteresis centered at T_C of the local magnetic moment of the Mn ions. The low temperature magnetic moment at Mn is determined to $\sim 3\ \mu_B$ and at high temperatures $\sim 4\ \mu_B$ were found from the $3s$ splitting of photoemission spectra. The localization of the Mn e_g electron takes place in the rhombohedral phase above the Curie temperature. This was also found by LSDA calculations of Banach and Temmerman (2004) and was mentioned in other publications for different Sr concentration (Kawano *et al.*, 1996; Dabrowski *et al.*, 1999). In contradiction to these results, our XMCD experiment for the LSMO samples shows a local Mn moment. Especially for the sample with Sr doping $x = 0.36$ the local Mn moment is $\sim 3.5\ \mu_B$/f.u. at 80 K. This is in direct contradiction to a delocalization of Mn e_g electron. This can be explained if one keeps in mind the essential differences of these experiments. On the one hand, the $3s$ splitting is not correlated with magnetization of the sample, but with the local spin configuration of the Fe ions. That means that the localization of e_g electrons at temperatures above T_C cannot be observed by XMCD and magnetometry due to the missing magnetization. On the other hand, the magnetic field which is applied during the XMCD experiment is not present in the XPS experiment. Therefore the magnetic field is the reason for the localization of the Mn e_g electron. This might play a key role in the CMR effect where the magnetic field leads to a better conductivity. This can be understood as the hole conductivity is disturbed by the delocalization of e_g electrons. The magnetic field localizes the e_g electrons and more hole charge carriers are available. The big influence of the magnetic field agrees with the finding of Asamitsu *et al.* (1995) where for a sample with $x = 0.17$ the transition from the orthorhombic to the rhombohedral structure was induced by a magnetic field. This shows the influence of magnetic fields and hence the strong coupling between spin, charge and structural properties. The shift of T_C with magnetic fields agrees also with magnetization measurements in figure 3.6 where for the samples with $x = 0.125$ and 0.17 the magnetic transition is shifted to higher temperatures with the applied magnetic field. This difference is most significant for the magnetization curves for $x = 0.125$ with 0.7 T and 5 T.

In figure 3.7 the phase diagram of LSMO, which is already presented in section 1.1 in figure 1.2, is compared with the orbital moments of Mn ions determined from XMCD measurements at 0.7 T applied magnetic field. The change of the orbital

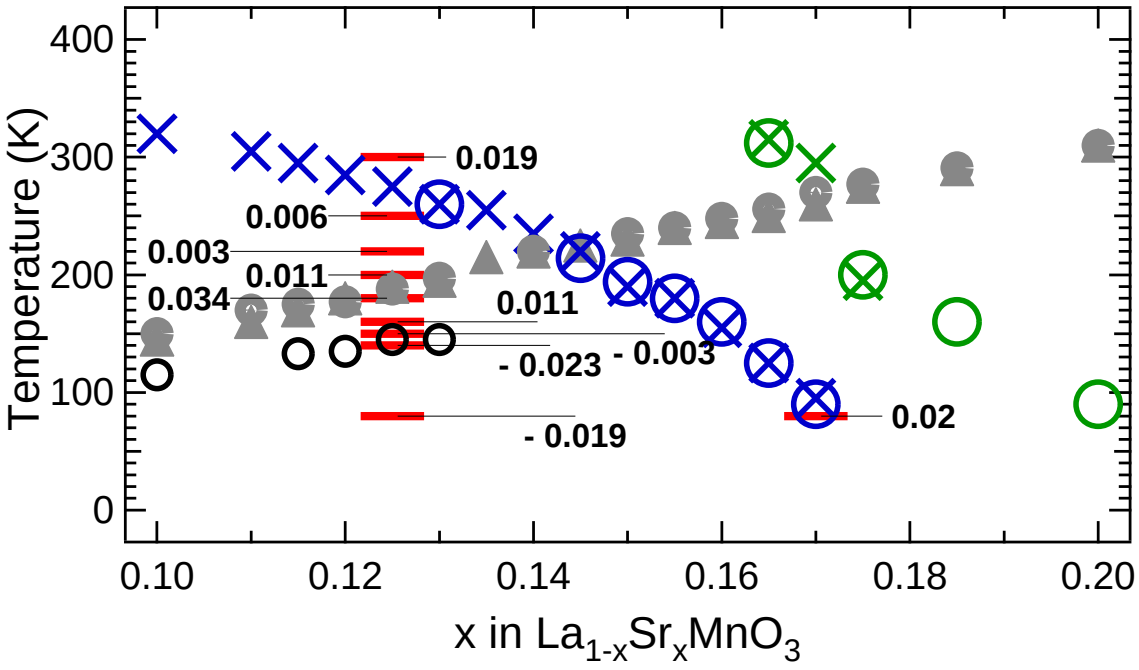

Figure 3.7: $La_{1-x}Sr_xMnO_3$ phase diagram from Dabrowski *et al.* (1999) (see figure 1.2). The magnetic orbital moment m_{orb} determined from XMCD measurements is marked with red lines and their value in μ_B/f.u..

moment corresponds to the structural transitions. In the orthorhombic phase with small coherent Jahn-Teller distortion (JTD) O* the orbital moment is 0.019 μ_B/f.u. and 0.02 μ_B/f.u. for $x = 0.125$ and 0.17, respectively. For $x = 0.125$ in the structural phase with large coherent JTD O′ from 275 to 188 K, the orbital moment changes from 0.006 μ_B/f.u. at 250 K via 0.003 μ_B/f.u. at 220 K to 0.011 μ_B/f.u. at 200 K. Close to the Curie temperature T_C=188 K, the largest orbital moment of 0.034 μ_B/f.u. is found. In the phase O′* where the coherent JTD is suppressed, this large orbital moment decreases via 0.011 μ_B/f.u. to nearly zero (−0.003 μ_B/f.u. at 150 K) at the charge ordering transition temperature of 144 K. In the charge ordered phase below 145 K the orbital moment is −0.023 μ_B/f.u. for 140 K and −0.019 μ_B/f.u. for 80 K which seems to be relatively constant. The transition from positive to negative orbital moment (150 K) for $x = 0.125$ seems to be slightly shifted to higher temperatures while the related transition temperature is at 145 K. The same case is found for the $x = 0.17$ sample where the orbital moment of 0.02 μ_B/f.u. at 80 K slightly below the transition temperature of 90 K is comparable with the orbital moment for $x = 0.125$ above this transition temperature where the structural phase O* is present. This small shift of the transition temperature of the sample with $x = 0.17$ can be explained with the results of Asamitsu *et al.* (1995) mentioned above where the transition temperature from rhombohedral to orthorhombic changes drastically with an applied field for such a sample.

It should be noted that the determined orbital moments are very small in comparison to orbital moments found in Ni clusters of three atoms where an orbital moment

of 0.47 μ_B is present (Guirado-López *et al.*, 2003). Here bigger clusters lead to smaller orbital moments because a more bulk like behaviour leads to quenching of the orbital moment. A bigger orbital moment of 0.76 μ_B/f.u. is found in the present work in a $LuFe_2O_4$ single crystal (see section 5.4.3).

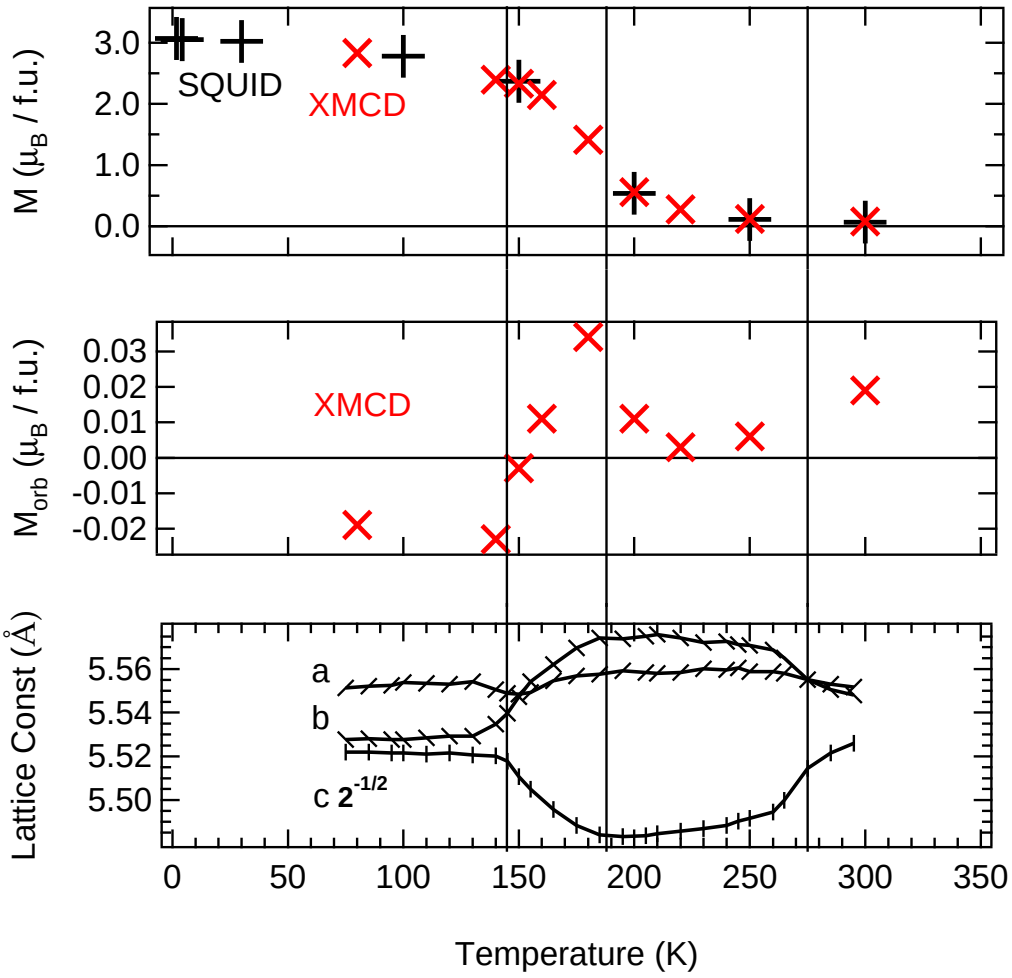

Figure 3.8: Total magnetic moment and Mn spin magnetic moment (top panel) and orbital magnetic moment (middle panel) and lattice parameter from Pinsard *et al.* (1997) (bottom panel) of $La_{0.875}Sr_{0.125}MnO_3$.

For a more detailed insight in the ordering of the $La_{0.875}Sr_{0.125}MnO_3$, the spin and orbital magnetic moment at the Mn site, the total magnetic moment and the lattice parameter from Pinsard *et al.* (1997) are compared in figure 3.8 on a temperature scale. In this figure three transition temperatures are marked. From 145 K to 188 K the structural transition from the ferromagnetic O′* to the paramagnetic O′ phase occurs. During this transition the orbital magnetic moment changes from ~ -0.02 μ_B/f.u. at 145 K to $\sim$0.04 μ_B/f.u. at 188 K. Remarkable is that the O′* structure has a negative orbital moment which is approximately the half of the positive moment at 188 K where the O′ phase is present. This is due to the structural

changes and indicates the occupation of different orbitals with different orbital quantum number m_l. Which orbitals are occupied in the different structural phases cannot be interpreted exactly because the quantitative value of the orbital moment is not very reliable due to quenching. Fact is that below 145 K another orbital ordering is present than above 145 K. The structural change from 145 K to 188 K (T_C) is seen in the lattice parameters and corresponds directly to the orbital moment. Li *et al.* (2009) found anomalies corresponding to the change of sign of the orbital moment. They observed a change of sign of the orthorhombic strain in the $b-c$ plane at the transition temperatures. Furthermore, in the range from 188 K to 275 K the cooperative Jahn–Teller distortion takes place. This leads to a reduction of the orbital moment. The results of Khomskii and Kugel (2003) give an explanation for the reduction in a cooperative JTD phase because they introduced that e_g orbitals which are placed in elongated or contracted octahedra away from the z–axis can be described by a combination of the d_{z^2} and the $d_{x^2-y^2}$ orbitals as described by equation 3.1:

$$|\Theta\rangle = \cos\Theta/2\left|z^2\right\rangle + \sin\Theta/2\left|x^2-y^2\right\rangle. \tag{3.1}$$

In this formula the mixing of two orbital states is described by the angle Θ, which changes the sign of $d_{x^2-y^2}$ state and therefore the orbital quantum number for different ordering can change the sign. The d_{z^2} state does not influence the orbital quantum number because for this state $m_l = 0$. For a perfectly coherent ordered phase, the corresponding orbital quantum numbers cancel out each other that leads to the reduction of the orbital moment in this phase. This is the case in the temperature range from 188 K to 275 K. Above this phase the orbital moment is growing because the cooperative JTD becomes small.

The achieved orbital moments are in agreement with the magnetization measurements of Dabrowski *et al.* (1999) for LSMO with $x = 0.12$ and 0.13 (see figure 3.9) showing for small applied magnetic fields of 20 Oe a decrease of magnetization at the charge ordering temperature (145 K for $x = 0.125$). After this decrease the low field magnetization is increasing again and a kink in high field magnetization measurements was mentioned by Xiong *et al.* (1999) which is explained by a magnetic transition. This transition can be interpreted as ferromagnetic coupling of the Mn^{4+} hole at low temperature and antiferromagnetic coupling of the hole at 145 K. This is in agreement with magnetization measurements in figure 3.6 where an increase from $\sim$2.4 μ_B/f.u. at 150 K to $\sim$3.1 μ_B/f.u. at 1.8 K is observed. Here for each Mn^{4+} with the magnetic moment of 3 μ_B, seven Mn^{3+} with 4 μ_B are present. The formally resulting spin moment makes $7 \times 4 + 3 = 31$ μ_B for ferromagnetic coupling and $7 \times 4 - 3 = 25$ μ_B for the antiferromagnetic one. As discussed before, the canting of spins reduces the total spin moment, but the ratio of 31:25 can be found if one compares the 1.8 K and the 150 K magnetization: 3.1 μ_B/f.u.$*25/31$ =2.5 μ_B/f.u.$\approx\sim$2.4 μ_B/f.u.. The somewhat smaller than expected spin moment at 145 K is due to the onset of the paramagnetic phase. The reduction of antiferromagnetic orbital ordering with decreasing temperature below 145 K in $La_{0.88}Sr_{0.12}MnO_3$ was suggested before by Endoh *et al.* (1999).

In figure 3.9 the low magnetic field magnetization versus temperature curves for $x = 0.12$ and 0.13 from Dabrowski *et al.* (1999) are compared with the orbital moments determined from XMCD for $x = 0.125$. The modulation of the magnetization

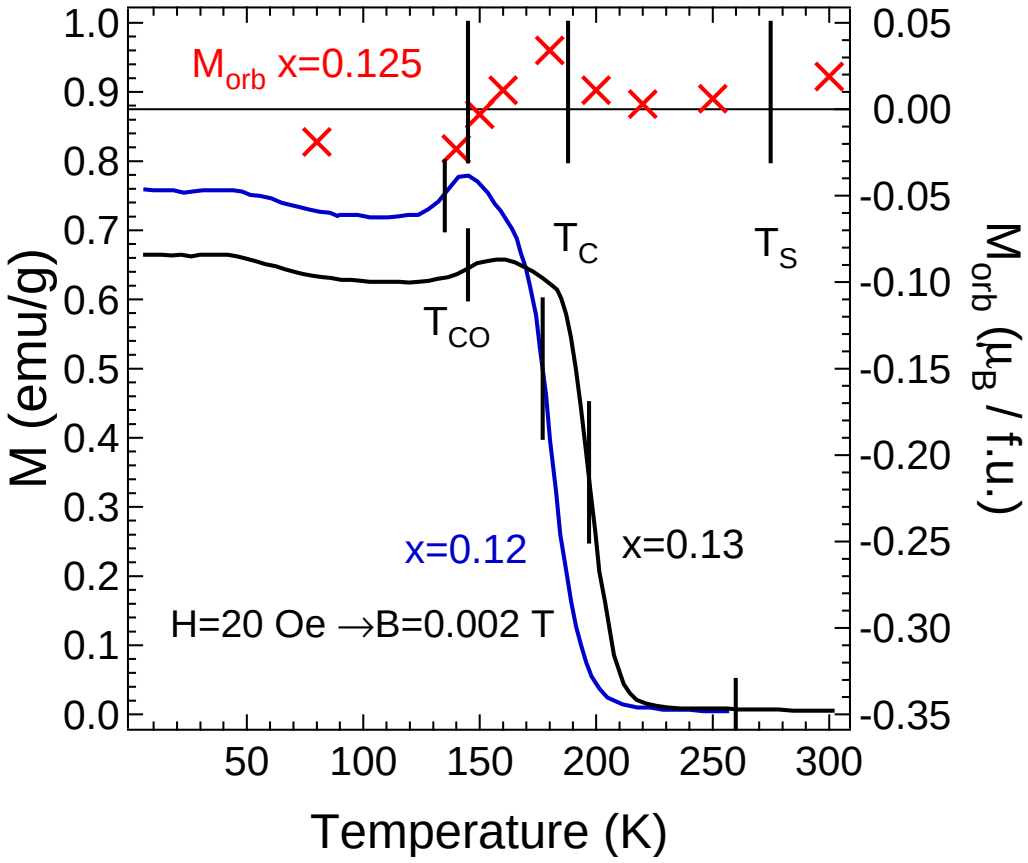

Figure 3.9: Total magnetic moment measured at low magnetic field by Dabrowski *et al.* (1999) (left axis) and orbital magnetic moment (right axis) of $La_{1-x}Sr_xMnO_3$ with x close to 0.125.

curve around T_{CO} corresponds to the orbital moment while around T_C the decreasing spin magnetization is covering the modulation.

3.6 Conclusions

The comparison of SQUID measurements with XMCD results proves the applicability of the factor for the spin magnetic moment found by Teramura *et al.* (1996) and the influence of charge transfer. The multiplet calculations gave the best agreement with XMCD spectra with charge transfer of 47.7% for Mn^{4+} and 29.0% for Mn^{3+}. For the samples with $x = 0.125$ and $x = 0.17$, a canted spin found by neutron powder diffraction (Pinsard *et al.*, 1997; Xiong *et al.*, 1999) is in agreement with the magnetometry and XMCD results. The perfect agreement of the magnetic moment measured by SQUID and that determined from XMCD for the single crystalline samples of $La_{1-x}Sr_xMnO_3$ ($x = 0.125$, 0.17 and 0.36) proves that the magnetic moment is completely localized at the Mn ions at the temperature of 80 K. For $La_{0.875}Sr_{0.125}MnO_3$, the above statement is moreover valid in the temperature range from 80 K to 300 K. In contrast to this result, Mannella *et al.* (2008) suggest for

samples with $x = 0.3$ to 0.4 that below T_C (>300 K) the Mn $2p$ e_g electrons are delocalized and do not contribute to the Mn $3s$ splitting which gives a local magnetic moment at the Mn sites of 3 μ_B/f.u.. On the one hand, the $3s$ splitting is not correlated with magnetization of the sample, but with the local spin configuration of the Fe ions. That means that the localization of e_g electrons at temperatures above T_C cannot be observed by XMCD and magnetometry due to the missing magnetization. On the other hand, this contradiction can be explained by the fact that the magnetic field is present for XMCD measurements and influences the delocalization of the e_g electrons. This big influence can explain the decreasing resistance with the applied magnetic field, because the localization of the e_g electrons leads to better hole conductivity.

For $x = 0.125$, the orbital magnetic moment determined from XMCD corresponds to the structural change which is visible in the lattice parameters (Dabrowski *et al.*, 1999). The change of sign of the orbital moment indicates the occupation of different orbitals in different structural phases. Corresponding to that, Li *et al.* (2009) observed a change of sign of the orthorhombic strain in the $b-c$ plane at the transition temperatures. In the temperature range from 188 K to 275 K where a coherent Jahn–Teller distortion takes place, the orbital moment is reduced. This is explained by the opposite sign of the orbital quantum numbers of the e_g orbitals which are different orientated in the crystal lattice. In magnetization versus temperature curves measured at low magnetic fields for x$\sim$ 0.125 (Dabrowski *et al.*, 1999) anomalies are present at structural transition temperatures. These anomalies can be identified as the orbital magnetic moment which is superimposed on the spin moment. The changes around the charge ordering temperature are interpreted as direct influence of the orbital magnetic moment. Furthermore a spin–flip below the charge ordering temperature suggested in several papers (Endoh *et al.*, 1999; Xiong *et al.*, 1999) is in agreement with presented magnetization versus temperature curves of $La_{0.875}Sr_{0.125}MnO_3$ and the increase of magnetization below 100 K (Dabrowski *et al.*, 1999).

Chapter 4

$REScO_3$ (RE = Sm, Gd, Dy)

4.1 Introduction

Perovskites of the type $REMO_3$, where RE^{3+} represents a trivalent rare earth metal, and M is a trivalent or mixed–valent transition metal, exhibit an enormous variety of physical properties (Maekawa *et al.*, 2004). During the last decade the so–called manganites have attracted much attention due to their unusual magnetic transport phenomena resulting in the colossal magneto resistance (CMR) effect (von Helmolt *et al.*, 1993; Jin *et al.*, 1994). These compounds are also promising candidates for various potential applications, e.g. for hard disk drive reading heads or in the rapidly growing field of magnetic RAM (MRAM). Another point is that ferroelectric perovskites such as $KTaO_3$, $KNbO_3$, $LiNbO_3$ or $BaTiO_3$ have been subject to intense studies due to their unusual dielectric properties and the possibility to switch the electrical polarization (Dawber *et al.*, 2005). This is leading to the idea that information can be also stored using the electrical polarization state of a ferroelectric material (FeRAM) (Fu and Cohen, 2000; Choi *et al.*, 2004). A practical realization of such device demands to prepare high quality thin films with thickness of the micron scale, in order to operate switches at few volts whereas the coercive voltages in these materials are at the order of kV/cm. These materials may also be used in somewhat related applications mentioned above, such as the next generation semiconductor components (to replace the SiO_2 gate dielectric). With the continued scaling of the gate oxide to below 2 nm, leakage currents due to tunnelling are very high, so the thickness must be increased without reducing the associated capacitance. This can be achieved with materials which exhibit a high dielectric constant k. Lucovsky *et al.* (2004) found that increases in k are generally accompanied by decreases in the optical band gap, E_g, the conduction band offset energy with respect to Si, E_B, and the effective electron tunnelling mass m_{eff}. Hence the adjustment of the electronic band structure plays an important role in tuning the high-k materials. In the last years a number of high-k compounds were found (Wilk *et al.*, 2001). The ternary oxide scandates $SmScO_3$, $GdScO_3$ and $DyScO_3$ are promising candidates to serve as high-k dielectrics in future applications (Zhao *et al.*, 2005; Kim *et al.*, 2006). The crystal structure of the rare earth scandates is displayed in figure 4.1.

Furthermore these materials are utterly interesting substrates for the production of highly strained ferroelectric thin films. Thin ferroelectric films often show strong

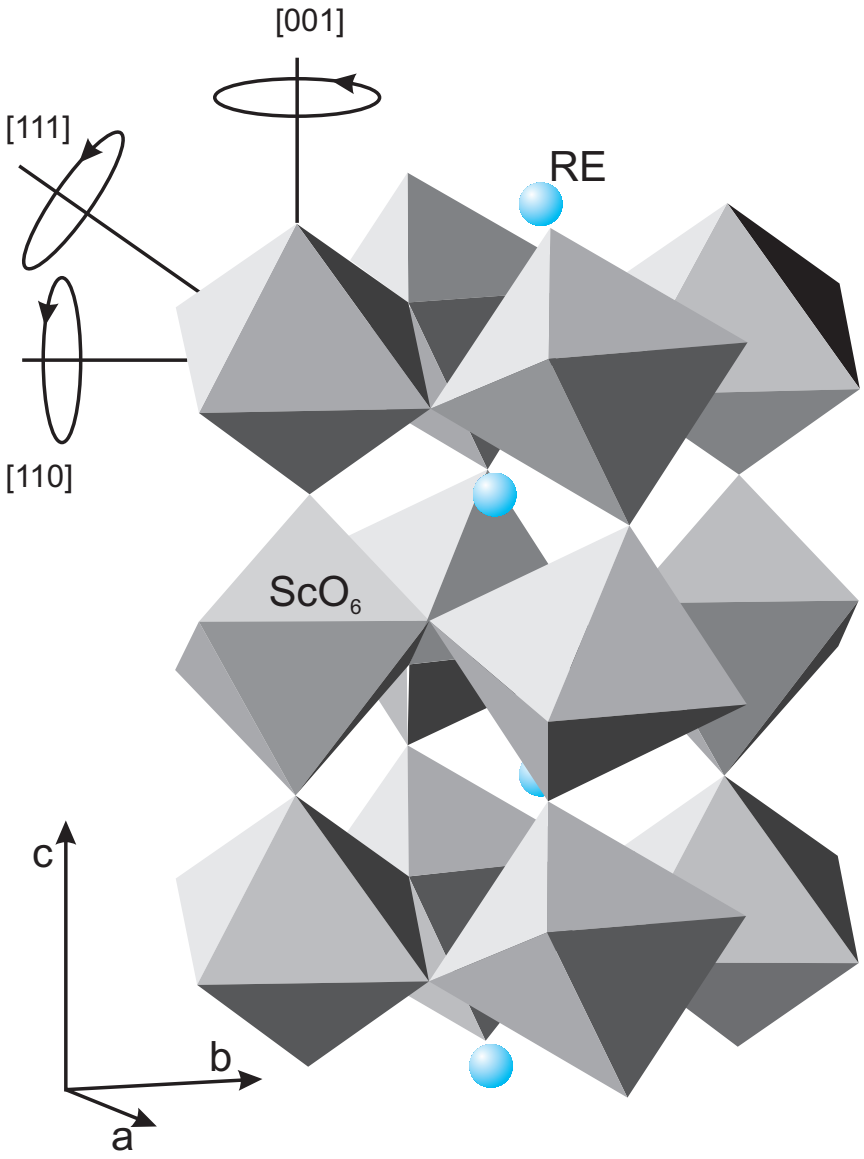

Figure 4.1: Orthorhombic $REScO_3$ crystal structure; octahedron tilting along [001], [110], and [111] is marked. RE is a rare earth atom in the A-site.

epitaxial strain effects, e.g. the change in critical temperatures, crystal structure and, generally, of their ferroelectric properties as a consequence of the growth on a substrate with defects or different lattice parameters. These strains can make worse the required thin film properties, but also can be used to control and optimise the desired ferroelectric properties if one finds a suitable high quality substrate. During the last few years the family of scandates such as $SmScO_3$, $GdScO_3$ or $DyScO_3$ has bridged the gap of suitable substrates, thus widening the scope for strain tailoring of the films and allowing to explore experimentally some of the desired predictions and properties (Schubert *et al.*, 2003; Choi *et al.*, 2004; Haeni *et al.*, 2004; Catalan *et al.*, 2006). Very recently it has been shown that $SrTiO_3/DyScO_3$ multilayers can be also used for modulation of the permittivity in terahertz range (Kužel *et al.*, 2007).

In view of all the above described experimental progress and potential applications, a proper theoretical approach to describe and predict the variety of properties in ferroelectric materials such as the scandates is highly desirable. Hence, these materials are subject to numerous first-principles studies since almost two decades now. Such calculations within density functional theory (DFT) offer a very powerful possibility to describe the structural, magnetic, and electronic structures of ferroelectrics in deep detail. However, there are some known limitations and inaccuracies. In particular in presence of rare earth $4f$ orbitals, the widely used local density approximation (LDA) and to some extent also the generalized gradient approximation (GGA) lead to a qualitatively incorrect description of the $4f$ energy placement. A related problem is that the structural properties, due to wrongly estimated localization of the $4f$ states, are often described improperly. There are a number of approaches in order to minimise or overcome these limitations. Some works include a Hubbard U parameter in order to consider the Coulomb repulsion between the highly localized $4f$ electrons. Some very recent works apply hybrid exchange functionals that combine fixed amounts of Hartree-Fock and LDA or GGA functionals to rare earth oxides as CeO_2 or ferroelectric oxides such as $BaTiO_3$ (Da Silva *et al.*, 2007; Bilc *et al.*, 2008).

Concerning the scandates, up to now only some electronic structure calculations for $DyScO_3$ have been reported (Delugas *et al.*, 2007). From experimental point of view only a few ultraviolet ellipsometry data, x-ray absorption spectroscopy data and a combination of internal photoemission and photoconductivity are available up to now (Cicerella, 2006; Lucovsky *et al.*, 2004; Afanas'ev *et al.*, 2004). However, in order to achieve a proper description of the electronic properties of rare earth based ferroelectric oxides (such as the scandates investigated here) a comparison with suitable experiments is of utmost importance. The techniques of x-ray photoelectron spectroscopy (XPS), x-ray absorption spectroscopy (XAS) and x-ray emission spectroscopy (XES) are powerful tools of unique precision in order to directly probe the total and partial densities of states (tDOS and pDOS, respectively) of ferroelectric materials (Moewes *et al.*, 1999; Kuepper *et al.*, 2004, 2003).

4.2 Sample Preparation

The single crystalline samples of $SmScO_3$, $GdScO_3$ and $DyScO_3$ were grown by R. Uecker of the *Institut für Kristallzüchtung* in Berlin (Uecker *et al.*, 2008). The starting materials for the crystal growth processes Dy_2O_3, Gd_2O_3, Sm_2O_3 and Sc_2O_3

were of 99.9% purity. To prepare the starting melt the powders were first dried and then mixed in a stoichiometric ratio, sintered at 900–1000 ℃, and finally isostatically pressed. Because the perovskite type RE scandates with the exception of $HoScO_3$ and $YScO_3$ melt congruently (Badie, 1978; Biegalski *et al.*, 2005), the selected crystals could be grown by the conventional Czochralski technique with RF-heating (25 kW microwave generator) and automatic diameter control. Iridium crucibles were used because the melting temperatures of these RE scandates lie between about 2100 ℃ for $DyScO_3$ and 2230 ℃ for$NdScO_3$ (Badie, 1978). The crucible dimensions were 40 mm in diameter and height (wall thickness 1.5 mm) for 20 mm diameter crystals, and 60 mm in diameter and height (wall thickness 1.5 mm) for 32 mm diameter crystals. Thermal insulation was provided by an outer alumina ceramic tube filled with zirconia granules. Flowing nitrogen or argon was used for the growth atmosphere. The pulling rate was 0.5–1.5 mm h^{-1} and the rotation rate was 8–15 rpm. The RE crystals were grown along the [110] direction. The structure and lattice constants of the samples were tested by x-ray powder diffraction and the chemical composition was investigated by an inductively coupled plasma optical emission spectrometer.

Spiral formation is a challenging problem in the Czochralski growth of several RE scandate crystals. It occurs if the dominant radiant heat transport through the crystal is reduced by absorption. The resulting flattening of the radial temperature gradient in the melt near the interface leads to a weakening of the thermally driven flow. This causes thermal instabilities, which can initiate spiral formation (Velickov *et al.*, 2007). The samples used during this work show a spiral formation of a few degree within a thickness of 3 mm.

4.3 Magnetic Measurements

Now we want to discuss magnetic properties by means of magnetic measurements. Magnetization versus temperature SQUID measurements were performed by K. Potzger and S. Zhou at *Forschnugszentrum Dresden-Rossendorf, Institute of Ion Beam Physics and Materials Research*. The results are presented in Figure 4.2. We expected the materials $SmScO_3$, $GdScO_3$ and $DyScO_3$ to exhibit similar magnetic order like the corresponding rare earth (3+) oxides, i.e. antiferromagnetism at low Néel temperatures. E.g., for Dy_2O_3, this temperature is 1.2 K (Bonrath *et al.*, 1966). Note that discussions about the kind of magnetic ordering in $GdScO_3$ occurred in the past (Stewart *et al.*, 1979). From our measurements basically the transition temperatures of the substrates were obtained prior to neutron diffraction measurement. The field-cooled $M-T$ curves were measured at a field H determined by $\mu_0 H$=0.5 T. The field was applied parallel to the single crystal surface. Cusps typical for the onset of antiferromagnetic order occur at 2.96 K ($SmScO_3$), 2.61 K ($GdScO_3$), and 3.10 K ($DyScO_3$). While the former two substrates exhibit Brillouin-type behaviour in the high temperature range (not shown), the latter deviates significantly exhibiting a large plateau (Fig. 4.2, inset). The peak for $GdScO_3$ is much broader than for the other samples. Moreover, $GdScO_3$ exhibits much larger magnetization and thus behaves similar to Gd_2O_3 (Stewart *et al.*, 1979).

Exemplarily, $DyScO_3$ was investigated with respect to its microscopic magnetic structure by means of neutron diffraction. The measurement was performed by

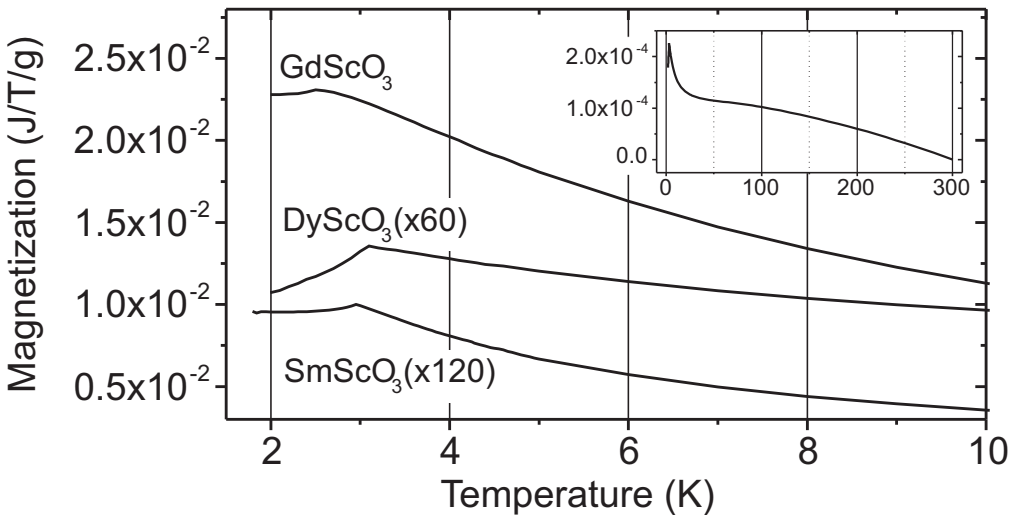

Figure 4.2: Magnetization versus temperature curves for $SmScO_3$, $GdScO_3$ and $DyScO_3$. The measurement was performed under an applied flux of μ_0H=0.5 T after cooling from 300 K in the same field. The magnification factor is indicated. The inset shows the high temperature range for $DyScO_3$. The constant M offset at 300 K has been subtracted.

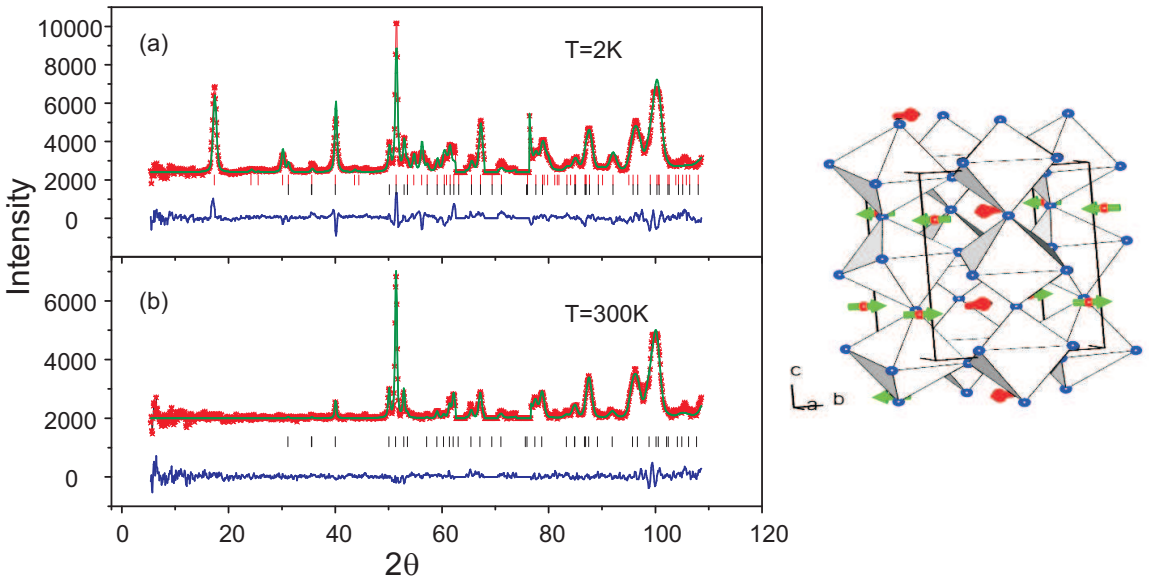

Figure 4.3: Neutron diffraction and crystal (magnetic) structures of $DyScO_3$. Results of the Rietveld refinement of the 2 K (a) and 300 K (b) neutron powder diffraction data of $DyScO_3$. The crystal and the magnetic structure (arrangement of arrows representing magnetic moments at Dy sites) is also shown.

A. Arulraj and N. Stüßer of the *Hahn-Meitner-Institut, Berlin*. Neutron powder diffraction of the compound $DyScO_3$ taken in a cylindrical vanadium container (diameter 8 mm) was recorded with the focusing diffractometer E6 at the Berlin Neutron Scattering Center (BENSC). The E6 diffractometer is equipped with a horizontally and vertically bent monochromator consisting of 105 pyrolytic graphite crystals ($20\times20\times2$ mm^3) mounted on a 15×7 matrix leading to a relatively high flux at the sample position. The incident wavelength was 2.442 Å. The data were collected at 2 K and 300 K. The integration of the Debye-Scherrer rings measured on a 2D detector, resulted in intensity versus scattering angle 2Θ for each temperature. Crystal (magnetic) structure was further analysed by Rietveld refinements employing the program GSAS (Larson and Von Dreele, 1994). An absorption correction for the cylindrical sample was carried out using GSAS, for which a wavelength dependent coefficient of 1.138 was used. A smoothly varying background was defined by extrapolating a fixed number of background points.

The room temperature (300 K) data set could be indexed with an orthorhombic lattice with space group *Pbnm*. In the 2 K data set several peaks in addition to those present in the 300 K data were observed (Fig. 4.3). These new peaks could be indexed with the propagation vector $k = 0$ and are due to the antiferromagnetic arrangement of the spins of Dy in the low temperature magnetic structure of $DyScO_3$. Of the four possible spin arrangements of the antiferromagnetic type only that with the magnetic group symmetry (Shubnikov group: $Pbnm'$ and $Pb'n'm'$) explains the presence of all the peaks of the 2 K data set. Symmetry analysis of the arrangement of the spin of Dy in the *Pbnm* structure of $DyScO_3$ indicates the following two possibilities. The first possibility is that the spin components of Dy belong to G mode with y component and A mode with x component (representation Γ_8) and in the second possibility G mode with x component and A mode with y component (representation Γ_5) (Bertaut, 1968). A Rietveld refinement of the 2 K neutron diffraction data set gives a good fit only with the second possibility (Shubnikov group: $Pb'n'm'$). In right panel of figure 4.3 the crystal structure and the magnetic structure (spin arrangement) of $DyScO_3$ at 2 K are shown.

4.4 LDA+U Calculations

The electronic structure calculations were performed by A. Postnikov of the Université Paul Verlaine in Metz with the (linearized) full potential augmented plane waves method [see e.g. reference (Singh, 1994)], of the density functional theory, as implemented in the WIEN2k code (Blaha *et al.*, 2001).

For the exchange correlation potential, we used the generalized gradient approximation in the form of Perdew-Burke-Ernzerhof (Perdew *et al.*, 1996, 1997). In order to describe the effects of intraatomic correlation beyond the conventional LDA or GGA treatment, we have taken into account the spin–orbit interaction and orbital dependent potential, notably LDA+U (Anisimov *et al.*, 1997) –or, rather GGA+U in our case,– specifically in the "LDA+U(SIC)" flavour of the WIEN2k implementation, with the correction added in the $4f$ shell of a rare earth. Even as the U and J values in the LDA+U formalism can be, in principle, estimated from first principles calculations (Anisimov and Gunnarsson, 1991), it is a more practical routine to use them as

adjustable phenomenological parameters. In the present context, we were guided by the placement of occupied (majority spin) RE $4f$ states in the x-ray (photo)emission spectra, relative to other valence band states. The best agreement was achieved with $U = 0.4$ Ry $= 5.4$ eV for all three samples. This sole criterion was, however, conflicting with the (experimentally founded) condition to have the band gap free from the minority spin $4f$ states. In order to satisfy this second criterion, we preferred to use somehow elevated U values, that resulted in a slightly overbonded majority spin RE $4f$ states. Our values of choice are $U = 0.6$ Ry $= 8.1$ eV for Gd $4f$ and $U = 0.8$ Ry $= 10.8$ eV for $SmScO_3$ and $DyScO_3$, as used in the comparison with the experiment (in part giving the reference to the results obtained with other U values as well). The J value was kept equal to 0.05 Ry $= 0.68$ eV.

Instead of the experimentally established noncollinear ferromagnetic structure depicted for $DyScO_3$ in figure 4.3 of section 4.3, we considered its most straightforward collinear simplification, with spin moments of RE centers set antiparallel between the nearest neighbours (both in the ab plane and along the c axis of Fig. 4.3). As the RE magnetic moments are quite localized (and really negligible, below 0.01 μ_B, on Sc and O sites), the plotted partial DOS of the antiferromagnetic structure are practically indistinguishable from those in the ferromagnetic phase.

Now the LDA+U calculations with $U = 0.4$ Ry are presented in detail. It has to be noted that these calculations are performed in ferromagnetic state. The influence of the magnetic ordering is marginal as discussed above.

The calculations for $SmScO_3$ are presented in Fig. 4.4. The Sm $4f$ states (top panel in Fig. 4.4) are dominating the occupied spin up DOS between -6 and -9.5 eV. The unoccupied Sm $4f$ states comprise spin up and spin down states. In the second panel of Fig. 4.4 Sm $5d$ and Sm $5p$ states are presented. The Sm $5d$ states are mainly occupied states from -16 eV to -24 eV. Sm $5p$ is mainly unoccupied from 1 eV to 7 eV. The calculated Sm states agree with the $4f^5$ configuration in high spin state. The Sc $3d$ states (third panel in Fig. 4.4) are mainly unoccupied from 1 eV to 7 eV, but a smaller contribution in the occupied states from -3 eV to -6.5 eV is due to hybridization with O $2p$ states. The Sc $3p$ states are completely occupied and located at ~ -29 eV. The calculations of oxygen states (panel four and five in Fig. 4.4) are split in x-y-direction and z-direction. Only small differences occur in the different directions. The O $2p$ states are building up intense bands between -3 eV and -6.5 eV, and contribute to the unoccupied DOS in the range of ~ 1 eV to 9 eV which are due to hybridization with Sc $3d$ and Sm $5d$ states. The O $2s$ states are mainly located in the range from -16 eV to -24 eV and at ~ -29 eV which is in the energy range of Sm $5p$ and Sc $3p$, respectively. A small O $2s$ density in the unoccupied DOS is located at $\sim$4 eV.

In Fig. 4.5 the calculations for $GdScO_3$ are plotted. The Gd $4f$ states (top panel) are dominating the occupied spin up DOS at $\sim$8 eV. Gd $4f$ spin down states are completely unoccupied. Gd $5d$ and Gd $5p$ states are presented in the second panel. The Gd $5d$ states are mainly contributing to the unoccupied DOS between 1 eV and 7 eV. The main part of the Gd $5p$ is present from -17.5 eV to -22.5 eV and ~ -25.5 eV. The calculated Gd states agree with the $4f^7$ configuration in high spin state. In the third and the fourth panel the Sc $3d$ and Sc $3p$ states, respectively, are presented. The Sc $3d$ states are mainly located in the unoccupied DOS between 1 eV

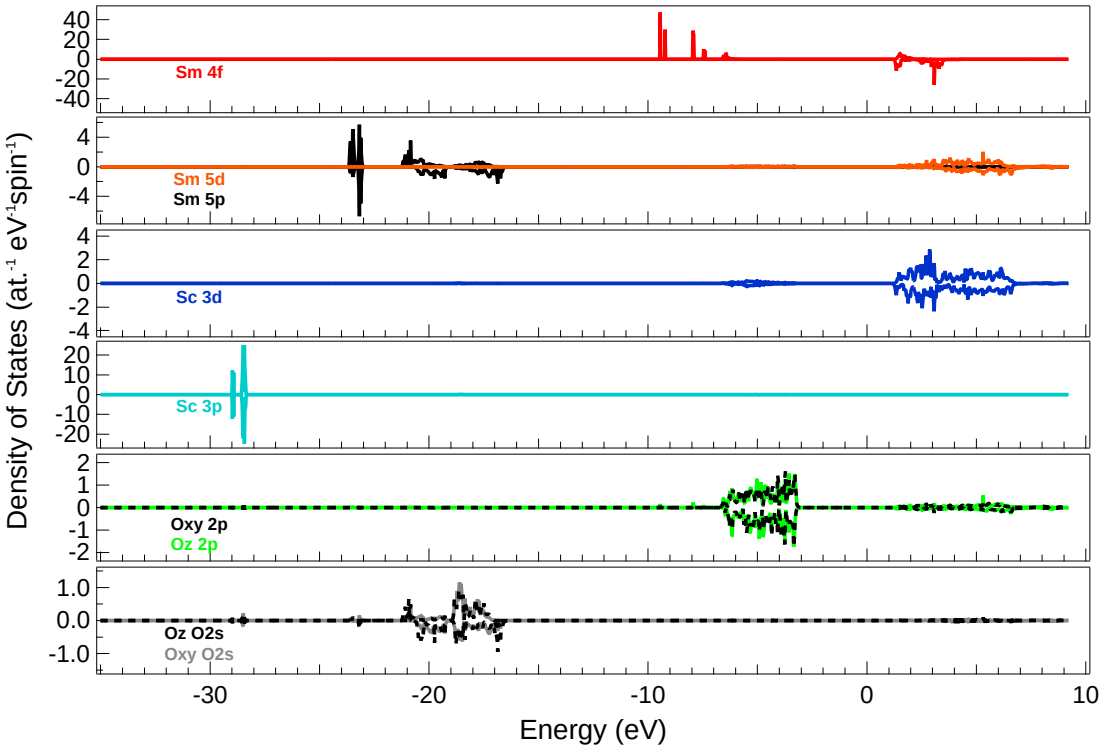

Figure 4.4: Band structure (LDA+U) calculations of the densities of states (DOS) of $SmScO_3$ in ferromagnetic ground state.

and 7 eV, but due to hybridization with O $2p$ a small density is in the occupied states between -3 eV and -7 eV. The Sc $3p$ states are completely occupied and located at ~ -29 eV. The oxygen states (panel four and five in Fig. 4.5) are split in x-y-direction and z-direction. The different directions show only small differences. The main part of the O $2p$ states is occupied and is located between -3 eV and -7 eV. The density in the unoccupied DOS between 1 eV and 9 eV is due to hybridization with Sc $3d$ and Gd $5d$ states. The O $2s$ states are mainly located in the range from -17 eV to -23 eV and ~ -29 eV which is in the energy range of Gd $5p$ and Sc $3p$, respectively. A small O $2s$ density in the unoccupied DOS is located at $\sim$4 eV.

The calculations for $DyScO_3$ are presented in Fig. 4.6. In the top panel the Dy $4f$ states are plotted. They are dominating the DOS. The main part of the occupied states is in spin up state between -6 eV and -9 eV. A smaller occupied DOS is found at ~ -5 eV. The unoccupied Dy $4f$ states in spin down state are located between Fermi level and 3 eV. The small spin down state just below Fermi level in the Dy $4f$ calculation belongs to the unoccupied states. It appears below Fermi level due to shift of the calculations for comparison with the experiment. These states are not present in the experimental band gap. In the second panel the Dy $5d$ and Dy $5p$ DOS is presented. The Dy $5d$ states are mainly unoccupied and are located between 1.5 eV and 7 eV. The Dy $5p$ states are completely occupied and take place at -18 eV to -19 eV, -21 eV to -23 eV and ~ -27 eV. The Dy states are comparable with a

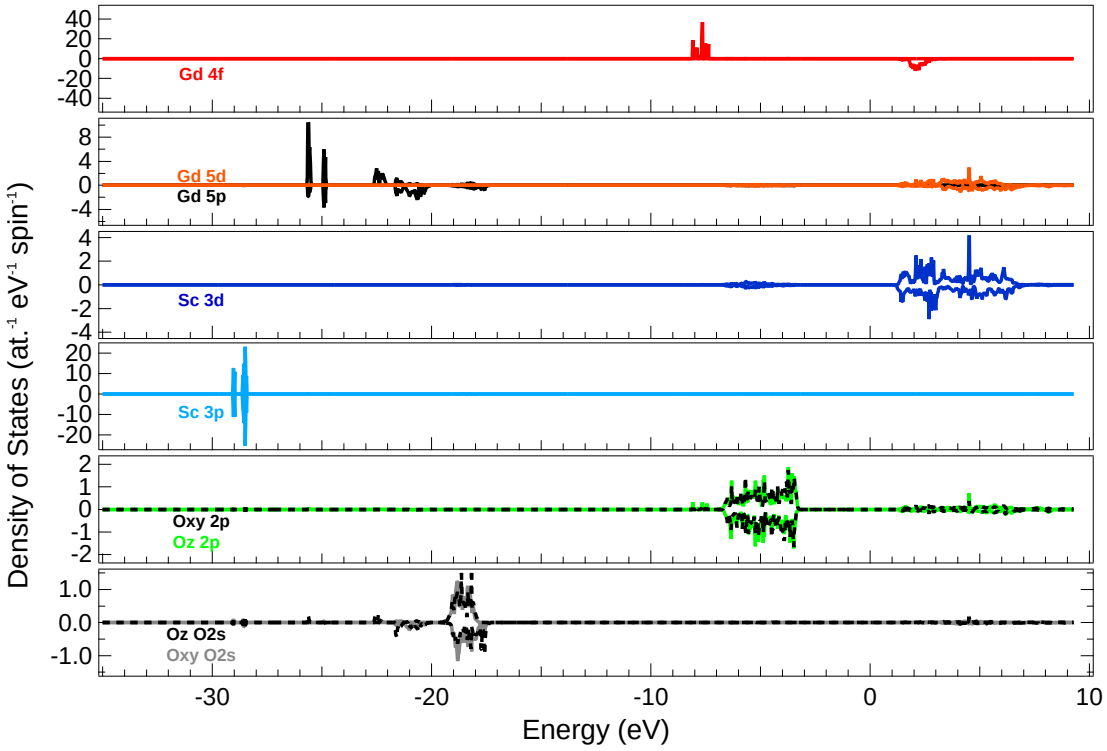

Figure 4.5: Band structure (LDA+U) calculations of the densities of states (DOS) of $GdScO_3$ in ferromagnetic ground state.

$4f^9$ configuration in high spin state. The Sc DOS of $3d$ and $3p$ states is presented in panel three and four, respectively. The Sc $3d$ states are mainly unoccupied between 1.5 eV and 7 eV. The small occupied Sc $3d$ states in the range of -3 eV to -7 eV is due to hybridization with O $2p$ states. The Sc $3p$ states are completely occupied and are located at ~ -29 eV. The oxygen DOS is plotted in panel five (O $2p$) and panel six (O $2s$) and is split in x-y-direction and z-direction. The different directions show only small differences. The O $2p$ states are mainly occupied in the range of -3 eV to -7 eV. The unoccupied O $2p$ states are located between 1.5 eV and 9 eV due to hybridization with Dy $5d$ and Sc $3d$ states. O $2s$ states are mainly occupied at -18 eV to -19 eV, -21 eV to -23 eV and ~ -29 eV. These states are in the energy range of Dy $5p$ and Sc $3p$. A small unoccupied DOS of O $2s$ is located at $\sim$4 eV.

In conclusion the calculations with $U = 0.4$ Ry show that the RE $4f$ states are dominating the occupied DOS between -6 eV and -9 eV (Sm and Dy) and between -7 eV and -8 eV (Gd). These states are mirroring the spin configuration of the RE atoms (Sm $4f^5$, Gd $4f^7$ and Dy $4f^9$). The RE $4f$ states seem to be not much correlated to other states. The occupied O $2p$ states seem to hybridize with the unoccupied Sc $3d$ states and the unoccupied RE $5d$ states. The fact that the occupied O $2s$ sates are in the energy range of Sc $3p$ and Dy $5p$ states points to a small correlation between the O $2s$ states and RE $5p$ and Sc $3p$ states. The appearance of RE $4f$ states inside the band gap is not in comparison with the experiments.

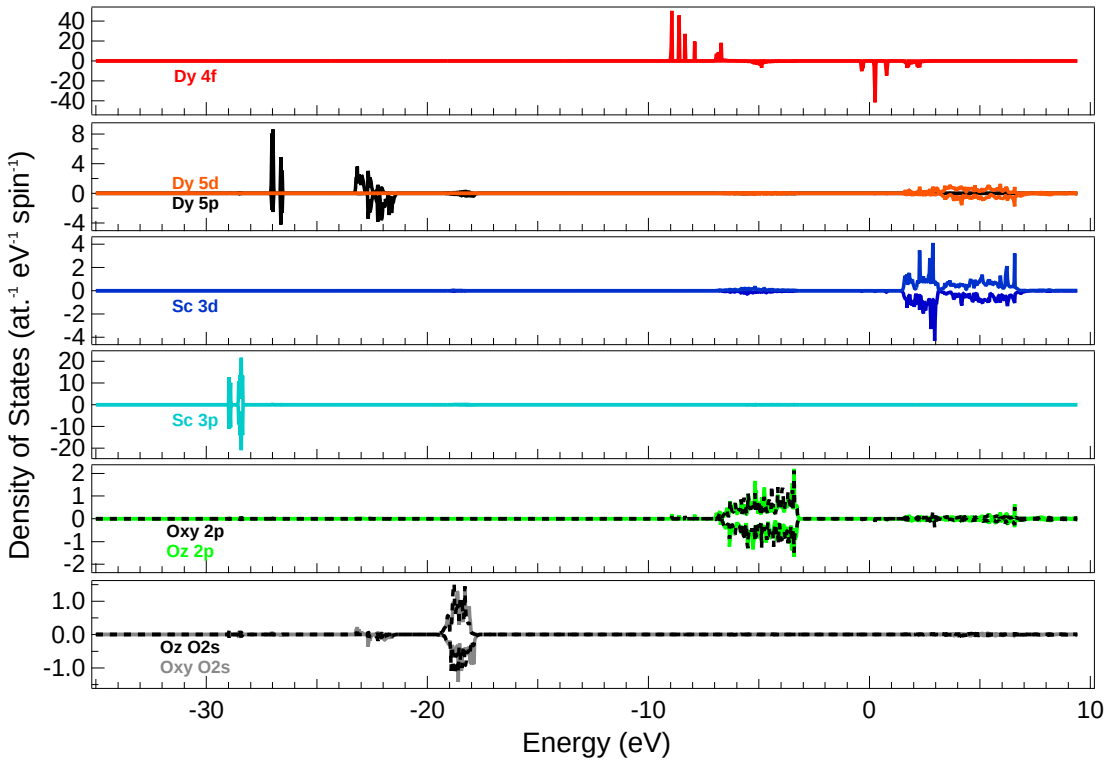

Figure 4.6: Band structure (LDA+U) calculations of the densities of states (DOS) of $DyScO_3$ in ferromagnetic ground state.

Therefore calculations with higher U values were performed.

Now the LDA+U calculations with U value of 0.6 Ry for $GdScO_3$ and 0.8 Ry for $SmScO_3$ and $DyScO_3$ in antiferromagnetic ground state are presented. The tuning of U can be subjected to careful analysis and argument. As stated above, we chose a compromise between the position of RE $4f$ states in the valence band and the need to the band gap free of the RE $4f$ states. Emphasizing a typically semiempirical character of the U values in practical calculations, it is noted that the examples are known where the U values have been evaluated over a range of rare earth compounds. E.g. Larson *et al.* (2007) cited a range of U values gradually varying from 7.47 eV (CeN) to 10.94 eV (LuN), in a row of rare earth nitrides. Our values are close to those cited by Larson *et al.* (2007), with a noticeable difference that we were primarily guided by the criteria named in the previous section. Summarizing the results over different U, we note that the larger U values, understandably, move the (vacant) minority spin $4f$ states out of the band gap, as desired. However, this happens at the expense of lowering the majority-spin Dy $4f$ well below its experimentally expected position. This problem illustrates the shortcoming and crudeness of the LDA+U approach: with a single tuneable parameter it is difficult to accommodate the correct placement of $4f$ states relative to the valence band involving other atoms, and the introduction of further tuneable U-parameters (e.g., for Sc $3d$ and O $2p$ states) would sacrifice physical transparence.

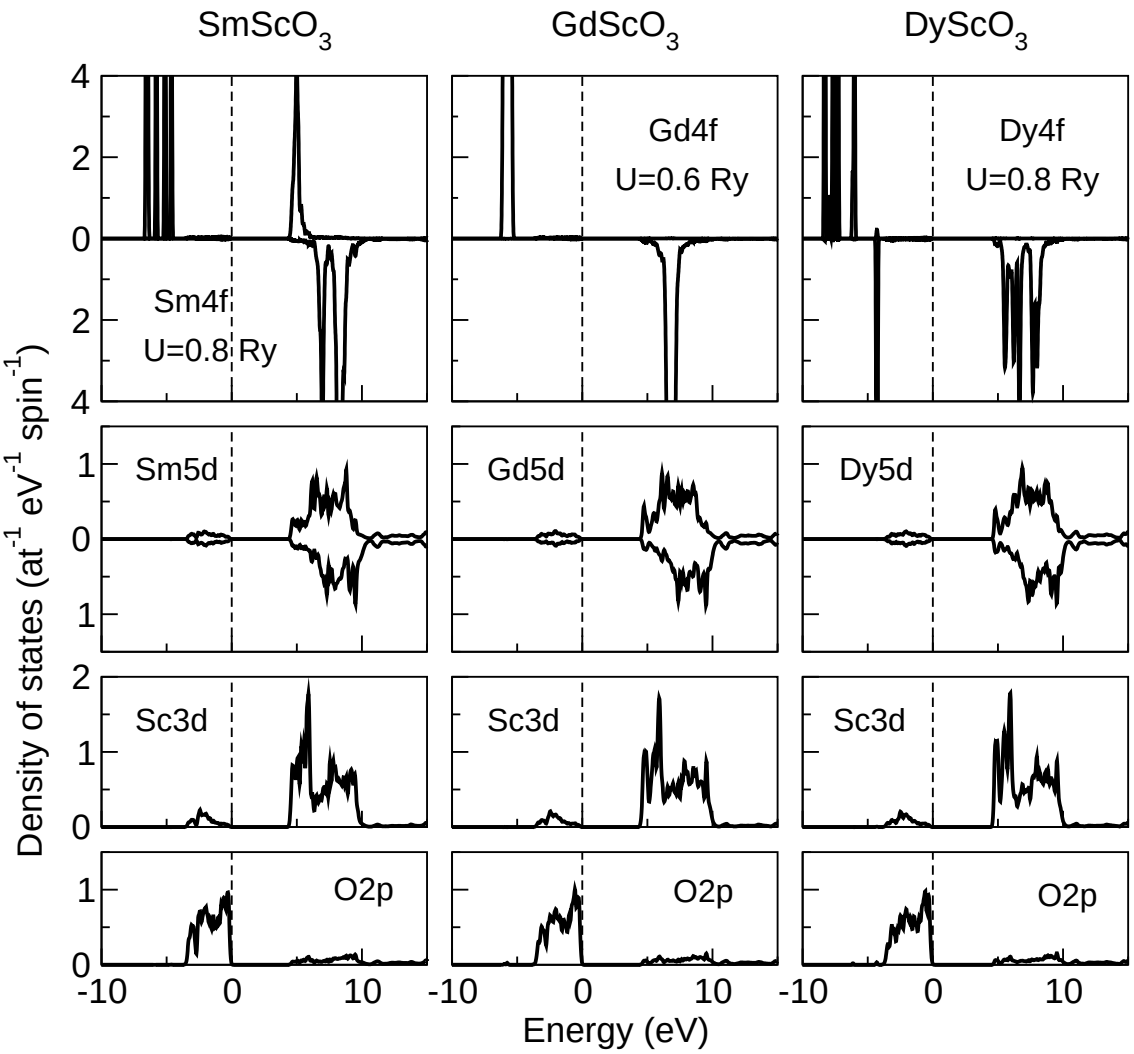

Figure 4.7: Band structure (LDA+U) calculations of the densities of states (DOS) of $SmScO_3$, $GdScO_3$ and $DyScO_3$ in antiferromagnetic ground state.

With this in mind, we note that occupied RE $4f$ states are intentionally placed just below the experimental determined valence band, which is formed predominantly by O $2p$, with a small admixture of RE $5d$ and Sc $3d$ in the range between 0 eV and -3 eV. However, due to the orbital-dependent potential taken into account, the $4f$ peak remains narrow only for Gd (around -6 eV) with its half-filled shell, whereas for Sm (-4.5 eV to -7 eV) and Dy (-4.5 eV to -8.5 eV) it reveals a system of energy levels, yielding a non negligible hybridization with the valence band (majority-spin states) and the conduction band (minority-spin states). Apart from the details of this hybridization, the Sc $3d$ partial DOS and the RE $5d$ DOS are almost identical throughout the three compounds (occupied: 0 eV to -4 eV, unoccupied: 4.5 eV to 10 eV). For the comparison with the experimental data in the following the Fermi level of the calculations with higher U value is shifted by -2.5 eV into the band gap. That the experimental Fermi level lies in the calculated gap can be due to a very

small amount of defects.

4.5 Core Level XPS of RE, Sc and O

The valence states of the elements in the rare earth scandates were determined by x-ray photoelectron spectroscopy (XPS). The chemical shift and the shape of the XPS core levels give information about the valence state. The XPS measurements were performed at the *University of Osnabrück* with the photoelectron spectrometer PHI 5600ci as described in section 2.6.1.

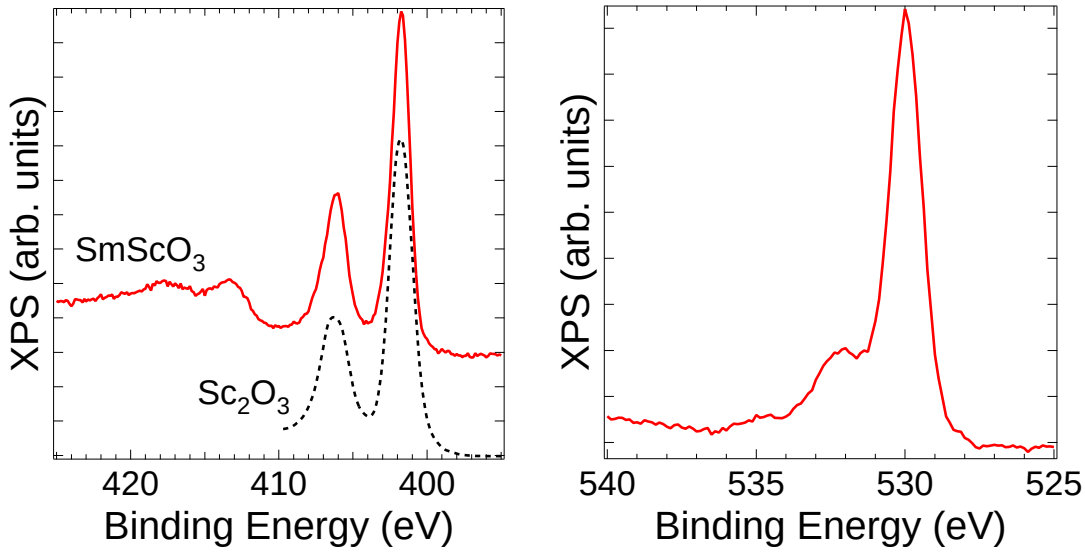

Figure 4.8: Sc $2p$ (left panel) and O $1s$ (right panel) core level XPS spectra of $SmScO_3$. Sc_2O_3 is used as Sc^{3+} reference (Chastain, 1992).

$SmScO_3$ XPS core level The Sc $2p$ core level XPS spectra of $SmScO_3$ is plotted in the left panel of figure 4.8 together with the Sc $2p$ core level XPS spectra of Sc_2O_3 where Sc is trivalent. The sharp Sc $2p_{3/2}$ peak is shifted to ∼402 eV leading to the 3+ valence state of Sc atoms. The spin–orbit splitting of the Sc $2p$ level is ∼4.5 eV. Thus the Sc $2p_{1/2}$ peak is at around 406 eV. There are two satellites, one slightly above 413 eV and the other slightly below 418 eV. These satellites belong to the Sc $2p$ levels and are due to excitations in the valence band from O $2p$ states to unoccupied Sc $3d$ states, which are hybridized with each other. In the right panel of figure 4.8 the O $1s$ core level of $SmScO_3$ show a main peak at 530 eV regarding to O^{2-} atoms in metal oxides. The shoulder at 532 eV is due to defects at the oxygen site which are usually located at the surface, but can also appear in the bulk. The small peak at 535 eV is due to carbon oxide contamination of the surface.

The XPS spectra of the Sm $3d$ core level is plotted in the left panel of figure 4.9. The main peak at 1083 eV belongs to the Sm $3d_{5/2}$ level in 3+ valence state (Chastain, 1992). The Sm $3d_{3/2}$ peak is located at 1110 eV. The spin–orbit splitting of Sm $3d$ is 27 eV. The small shoulders at both peaks and the small structures around the

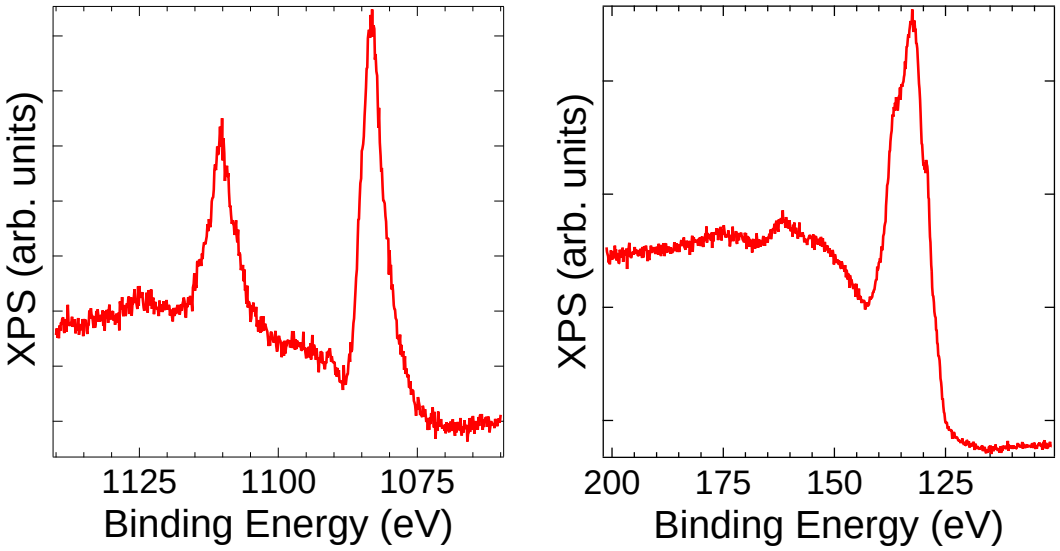

Figure 4.9: Sm 3*d* (left panel) and 4*d* (right panel) core level XPS spectra of $SmScO_3$.

main peaks are due to the complex multiplet splitting of the Sm 3*d* states. In the right panel of figure 4.9 the Sm 4*d* spectra is presented. The main structure takes place from 123 eV to 144 eV. In this region one can see several shoulders due to the multiplet splitting.

The valence states of the atoms in the $SmScO_3$ compound are as expected, Sm^{3+}, Sc^{3+} and O^{2-}.

$GdScO_3$ XPS core level The XPS results for Sc 2*p*, O 1*s*, Gd 3*d* and Gd 4*d* core level of the $GdScO_3$ sample are presented in figures 4.10 and 4.11, respectively.

The Sc 2*p* XPS spectra of $GdScO_3$ is plotted in the left panel of figure 4.10 together with the Sc 2*p* XPS spectra of Sc_2O_3 where Sc is trivalent. The Sc $2p_{3/2}$ and the Sc $2p_{1/2}$ peaks located at ∼402 eV and ∼406 eV are spin–orbit split by ∼4.5 eV. The chemical shift points to a 3+ valence state of the Sc atoms. The satellites belonging to the Sc 2*p* levels at 413 eV and ∼418 eV are due to excitations in the valence band from O 2*p* states to unoccupied Sc 3*d* states, which are hybridized. This result is identical to the result for the $SmScO_3$ sample.

In the right panel of figure 4.10 the O 1*s* XPS core level spectrum is displayed. The main peak at 530 eV points to O^{2-} in metal oxides. The small shoulder at 532 eV is due to defects at the oxygen site in comparison with the result for $SmScO_3$.

The Gd 3*d* XPS core level spectra of $GdScO_3$ and Gd_2O_3 are plotted in the left panel of figure 4.11. The trivalent Gd_2O_3 spectrum is similar to the $GdScO_3$ spectrum. In the right panel of figure 4.11 the Gd 4*d* spectra of Gd metal, $GdScO_3$ and Gd_2O_3 is plotted. The peak structure is due to multiplet splitting of the 4*d* level. The main peak structure at ∼144 eV leads to a Gd^{3+} valence state. The structure is better resolved for the metallic sample than for the oxides, but the general structure is comparable for all three spectra.

The results of the XPS core level spectroscopy for $GdScO_3$ are the same as for

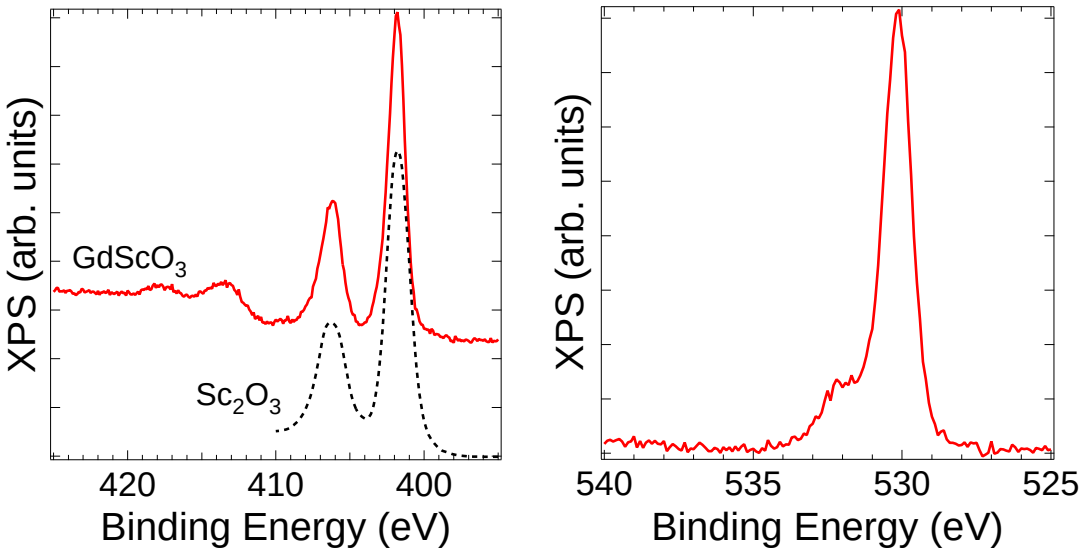

Figure 4.10: Sc 2p (left panel) and O 1s (right panel) core level XPS spectra of $GdScO_3$. Sc_2O_3 is used as Sc^{3+} reference (Chastain, 1992).

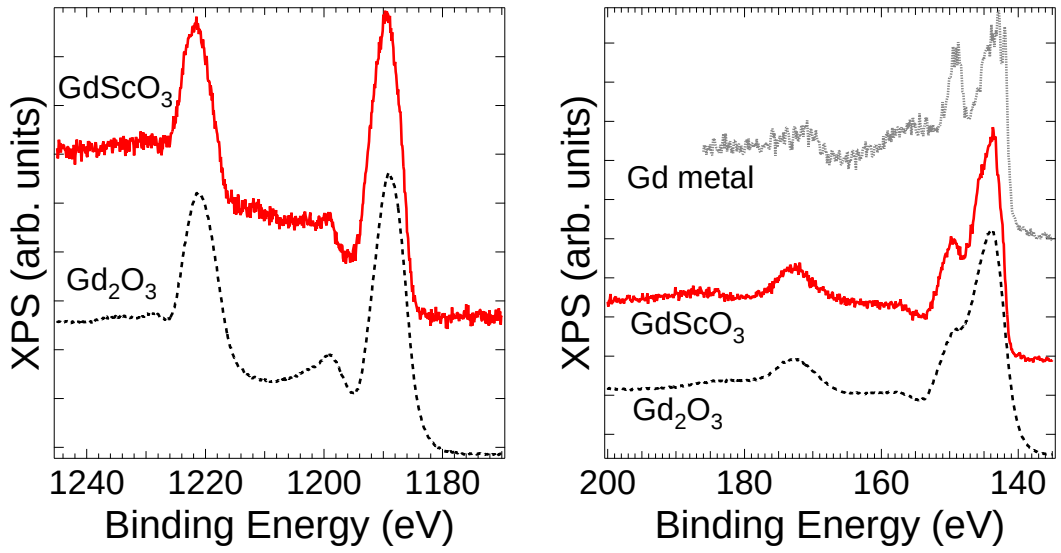

Figure 4.11: Gd 3d (left panel) and 4d (right panel) core level XPS spectra of $GdScO_3$ and reference spectra (Lütkehoff, 1997) of Gd_2O_3 and Gd metal.

the $SmScO_3$ sample. The valence states are as expected, Gd^{3+}, Sc^{3+} and O^{2-}.

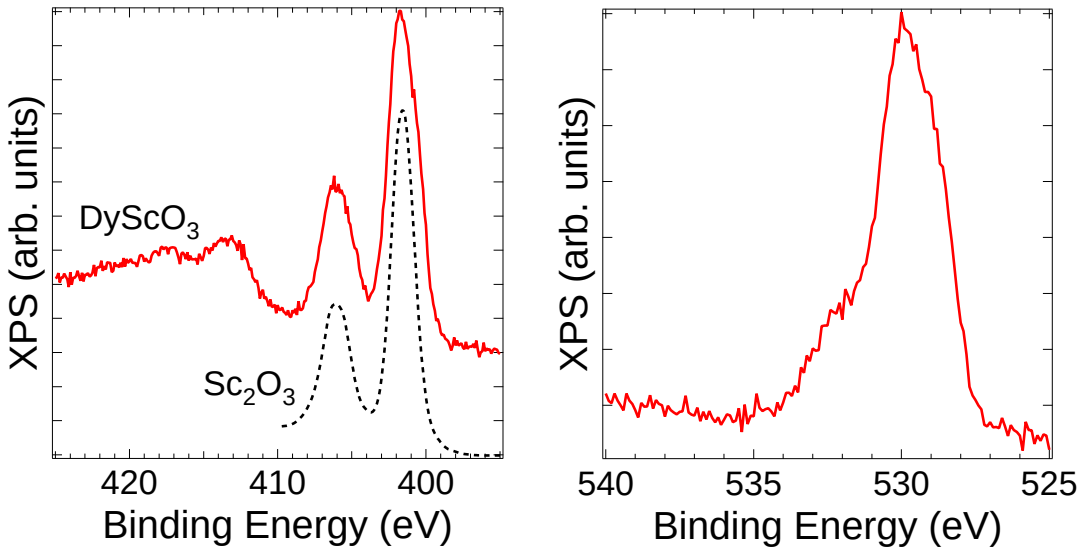

Figure 4.12: Sc 2p (left panel) and O 1s (right panel) core level XPS spectra of $DyScO_3$. Sc_2O_3 is used as Sc^{3+} reference (Chastain, 1992).

$DyScO_3$ XPS core level In the figures 4.12 and 4.13 the XPS core level spectra of Sc 2*p*, O 1*s*, Dy 3*d* and Dy 4*d* are presented and compared with reference spectra of Sc_2O_3 and Dy_2O_3.

The Sc 2*p* core level spectra of $DyScO_3$ and Sc_2O_3 in the left panel of figure 4.12 comprises the ∼4.5 eV spin–orbit split main peaks at 402 eV and 406 eV. The chemical shift leads to a Sc^{3+} valence state. The satellites of the Sc 2*p* level at 413 eV and ∼418 eV are due to the excitation in the valence band from O 2*p* to unoccupied Sc 3*d* in the conduction band, which are hybridized.

In the right panel of figure 4.12 the O 1s level of the $DyScO_3$ sample is presented. The main peak at 530 eV is common for metal oxides where oxygen is in 2- valence state. The shoulder at 532 eV is due to oxygen defects.

The Dy 3*d* spectrum of $DyScO_3$ is presented in left panel of figure 4.13 together with the Dy 3*d* spectrum of Dy_2O_3 where Dy is trivalent. Both spectra are very similar, but the Dy_2O_3 peaks are slightly broader and the background of the $DyScO_3$ spectrum is steeper due to the smaller amount of Dy in this sample. In the right panel the Dy 4*d* spectra of $DyScO_3$ and of Dy_2O_3 are plotted. The multiplet splitting in the peak structure from 152 eV to 160 eV is better resolved for the $DyScO_3$ sample than for Dy_2O_3. The small peaks at 162 eV and 165 eV are also better observable for the $DyScO_3$ sample.

The valence states of O and Sc in the $DyScO_3$ sample is as expected and comparable with the results of $SmScO_3$ and $GdScO_3$. It should be noted that the Dy valence state can deviate from 3+ explained by the results from Uecker *et al.* (2008) and Velickov *et al.* (2007). They found amounts of tetravalent rare earth ions in

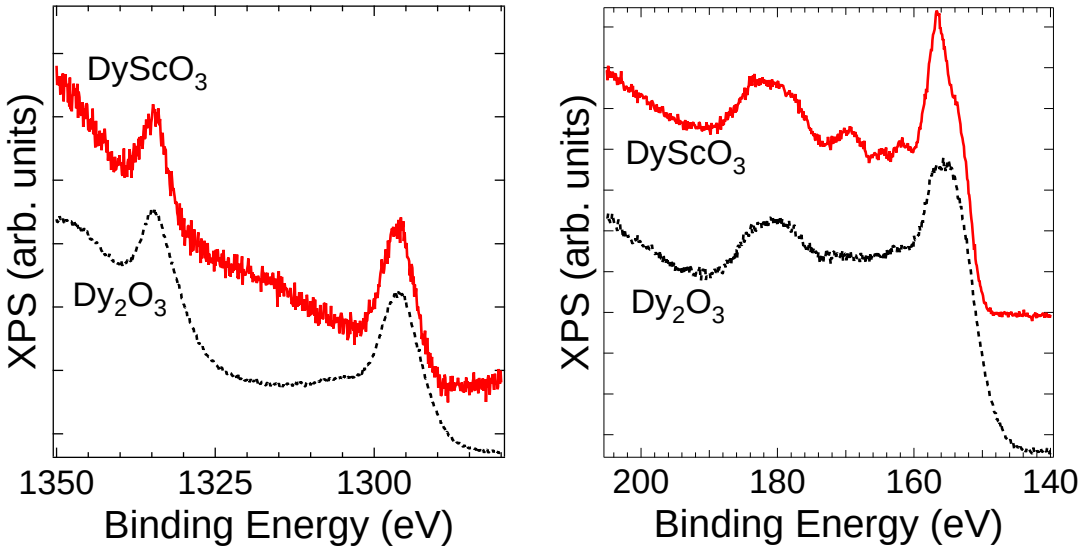

Figure 4.13: Dy 3d (left panel) and 4d (right panel) core level XPS spectra of $DyScO_3$ and of Dy_2O_3.

$DyScO_3$ and $TbScO_3$, that are responsible for colour changes of the samples. These amounts are in the range of 1 percent so that they cannot be observed precisely with XPS.

4.6 XAS and XES/RIXS of RE, Sc and O

With x-ray absorption spectroscopy (XAS) one can get element–specific information about the unoccupied states, while x-ray emission spectroscopy (XES) gives element specific information about the occupied states. The XAS and XES/RIXS experiments were performed at the *Advanced Light Source* in Berkeley, USA, at beamline 8.0.1. as described in section 2.6.4.

4.6.1 Sc $L_{2,3}$–Edge XAS and Sc $3d \rightarrow 2p$ XES

The Sc $L_{2,3}$-edge XAS of $SmScO_3$, $GdScO_3$ and $DyScO_3$ is plotted in the left panel of figure 4.14 in comparison with multiplet calculations. The spectral features are very similar for all three samples, but small differences in shape and intensity are observable. The spectra comprise four main features at 401 eV, 403 eV, 405 eV and 407 eV. Small features appear at 399.5 eV, 400 eV, 401.5 eV and 406.5 eV. The splitting of more than 4 eV between the first group of two main features and the last group of two main features refers to the spin–orbit splitting of the Sc $2p$. The smaller splitting inside both groups is close to 2 eV and is due to the crystal field of the oxygen octahedra surrounding the Sc atoms. The two small features in front of and one feature behind the first main peak at 401 eV are due to the multiplet splitting in octahedral symmetry as can be seen from the multiplet calculations in the same figure where the four main features and the three small features around

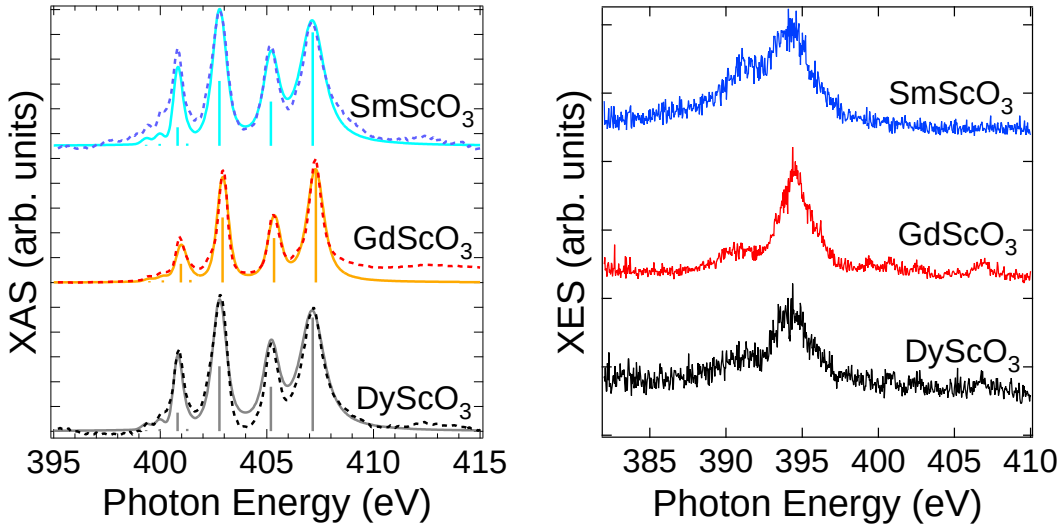

Figure 4.14: left panel: Sc $L_{2,3}$-edge XAS (broken lines) in comparison with multiplet calculations (sticks and solid lines) of REScO3. right panel: Sc $3d \rightarrow 2p$ XES excited with 420.2 eV of REScO3.

the 401 eV main peak are simulated in perfect agreement. The small feature at 406.5 eV and the differences between experiment and calculation in intensity and broadening of all peaks are due to further deformation of the oxygen octahedra. The differences between the samples are due to the influence of different electronic configurations of the rare earth atoms. This influence can arise from hybridization between the Sc $3d$ level and the O $2p$ level, which are hybridized with RE 5d levels. The similarity of the Sc $L_{2,3}$-edge XAS of $SmScO_3$ and $DyScO_3$ can be explained by the comparable electronic configuration of the RE atoms, namely Sm $4f^5$ and Dy $4f^9$. These configurations are comparable because the number of electrons in the Sm $4f$ is equal to the number of holes in Dy $4f$. The number of holes and the number of electrons are exchangeable in the multiplet theory. The parameters for the broadened multiplet calculations are summarized in table 4.1.

Table 4.1: Parameters for broadened multiplet calculations of Sc $L_{2,3}$-edge XAS in O_h symmetry of $SmScO_3$, $GdScO_3$ and $DyScO_3$. There are five values for Lorentzian broadening; one for the two prefeatures and four for the main peaks.

	Crystal Field (10Dq) in eV	Gaussian in eV	Lorentzian in eV (prefeatures and 4 peaks)				
$GdScO_3$	1.74	0.2	0.08	0.1	0.15	0.2	0.35
$Sm/DyScO_3$	1.74	0.2	0.02	0.02	0.25	0.3	0.6

The occupied Sc $3d$ states probed by XES are presented in the right panel of figure 4.14. The excitation energy was set to 420.2 eV for all samples. Due to the $3d^0$ configuration the occupied states of Sc $3d$ are nearly empty, but a small signal is present due to strong hybridization with O $2p$ states. The spectra comprise one main feature at 394 eV with one shoulder at 396 eV and another shoulder at 391 eV,

differently pronounced in all three samples. The main peak refers to Sc 3*d* states while the small shoulder at 396 eV is due to the hybridization with O 2*p* states. The shoulder at 391 eV appears in different intensities for the three samples. The energetic distance to the Sc 3*d* main feature refers to the spin–orbit splitting of Sc 2*p* states, but this cannot explain the different intensities of the shoulder. Hence the shoulder is influenced by the presence of the rare earth atom. This influence can originate from different distortions of the oxygen octahedra and from a more complex hybridization of Sc 3*d*, O 2*p* and RE 5*d* states. Such a complex hybridization was already mentioned by Lucovsky *et al.* (2004) and Liferovich and Mitchell (2004). Nevertheless the main part of this shoulder is explained with the spin–orbit splitting of Sc 2*p* states.

4.6.2 RE $M_{4,5}$-Edge XAS and RE $4f \rightarrow 3d$ XES

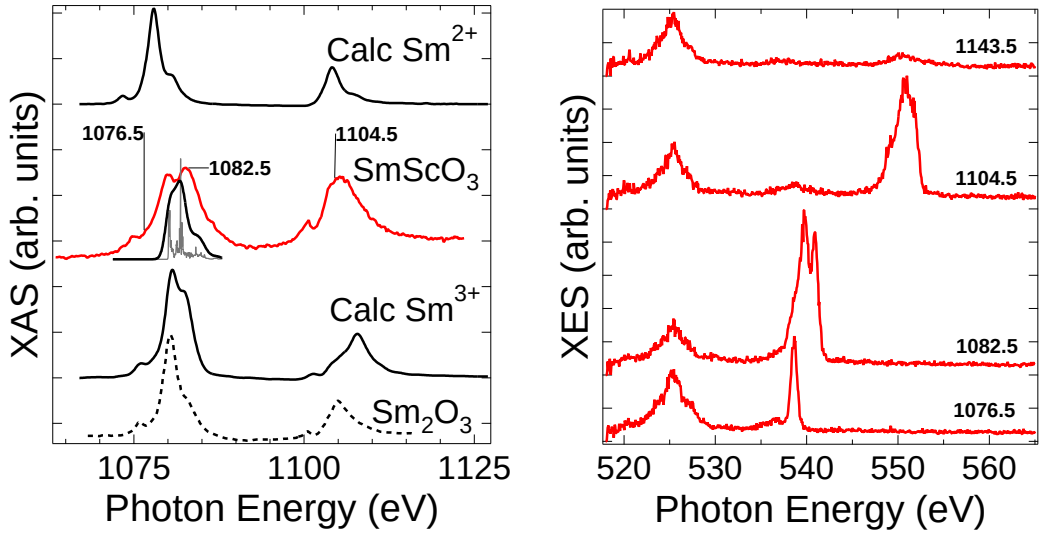

Figure 4.15: Left panel: $SmScO_3$ Sm $M_{4,5}$-edge XAS with band structure calculations of unoccupied states of Sm (grey sticks), Sm^{2+} and Sm^{3+} multiplet calculations (Thole *et al.*, 1985) (solid black) and Sm_2O_3 reference (Kaindl *et al.*, 1984) (broken black). Right panel: resonant Sm $4f \rightarrow 3d$ XES in second order.

$SmScO_3$ XAS and XES The Sm $M_{4,5}$-edge XAS is plotted in the left panel of figure 4.15. For comparison the XAS of the trivalent reference Sm_2O_3 (Kaindl *et al.*, 1984), the band structure calculation of unoccupied Dy states and multiplet calculations (Thole *et al.*, 1985) of divalent and trivalent Sm 3*d* XAS are presented. The XAS spectra consists of two intense features at 1080 eV (M_5-edge) and 1105 eV (M_4-edge) due to the spin–orbit splitting of Sm 3*d* states. The band structure calculation below the XAS agrees with the shape of the M_5-edge of the experiment, but cannot render the prepeak which is due to multiplet splitting. The XAS of the reference sample Sm_2O_3 shows a similar structure beside the double peak at 1080 eV which is not split in the reference, but this splitting appears in the band structure calculation and the multiplet calculations of Sm^{3+}. Kaindl *et al.* (1984) have interpreted such a splitting

with mixture of Sm^{2+} and Sm^{3+} for $Sm_{0.3}Y_{0.7}S$ sample. In our case a Sm^{2+} contribution cannot be responsible for the double peak feature in the experiment because the multiplet calculation of Sm^{2+} shows the main peak at lower photon energies than the double peak appears. The calculations can be very well calibrated to the experiment with respect to the small peak at ∼1100 eV. Hence the Sm $M_{4,5}$-edge XAS shows trivalent rare earth ions and some spectral features arise from the crystal distortion of $SmScO_3$. Surface defects may also play a role which can be the reason for the difference between experiment and calculation.

The excitation energies of the resonant XES data Sm $4f \rightarrow 3d$ in the right panel of figure 4.15 are indicated in the XAS spectra in the left panel. The second order of the rare earth emission was measured because of the limit of the detector. Therefore the spectra are at the half energy value of the first order rare earth spectra. The first order oxygen $1s$ emission at around 525 eV is present in each spectrum. The elastic peaks in the lower three spectra are clearly visible at 552 eV, 541 eV and 538 eV in the corresponding spectrum. In the spectrum excited with 1076.5 eV there is only a small inelastic feature at 537 eV. The resonantly excited inelastic part of the spectra excited with 1082.5 eV is more intense than the elastic peak in this spectrum. The resonant excitation at the Sm M_4-edge results in a three peak structure at around 550 eV. The already mentioned elastic peak at 552 eV is somewhat smaller than the inelastic peak at 550 eV with a shoulder at 549 eV. The normal XES spectra at the top of this figure shows the mentioned O $1s$ emission and just small inelastic peaks from the rare earth states at 537 eV and 550 eV. In the resonant XES spectra no loss feature is observable that would always appear in the same distance from the elastic peak. Therefore no small excitation in the valence band region take place. This is due to the large band gap which suppresses such effects.

$GdScO_3$ XAS and XES In the left panel of figure 4.16 the Gd $M_{4,5}$-edge XAS is plotted in comparison with the Gd $3d$ XAS of the trivalent reference compound Gd_2O_3 (Kaindl *et al.*, 1984), band structure calculations of the unoccupied Gd states and multiplet calculations of $3d$ XAS of Gd^{3+} (Thole *et al.*, 1985). The spin–orbit split main features are located at around 1185 eV and 1215 eV. The band structure calculations and multiplet calculations are in agreement with the experimental Gd M_5-edge. The XAS of the reference sample is very similar to the $GdScO_3$ XAS beside the intensity of the two shoulders at 1190 eV and the peaks at 1213 eV and 1215 eV, but the multiplet calculations show a similar intensity ratio for the double peaks at around 1215 eV. This similarities are a clear indication for the trivalent gadolinium ions in the sample and the reference.

The XE spectra of $GdScO_3$ (right panel of figure 4.16) were excited with the energies indicated in the XA spectrum. The spectra with resonant excited Gd M_5-edge (E_{exc} = 1181.51 eV and 1183.8 eV) comprise the corresponding elastic peak and the edge of the inelastic features. The complete inelastic emission structure of the Gd M_5-edge (∼590 eV) is visible in the resonant emission spectrum excited with 1215.7 eV. In this spectrum the inelastic Gd M_4-edge at 605 eV and the elastic peak at ∼608 eV are present. In the normal XES excited with 1163.5 eV the M_5- and the M_4-edge are located at ∼590 eV and 605 eV, respectively. No energy loss features are present.

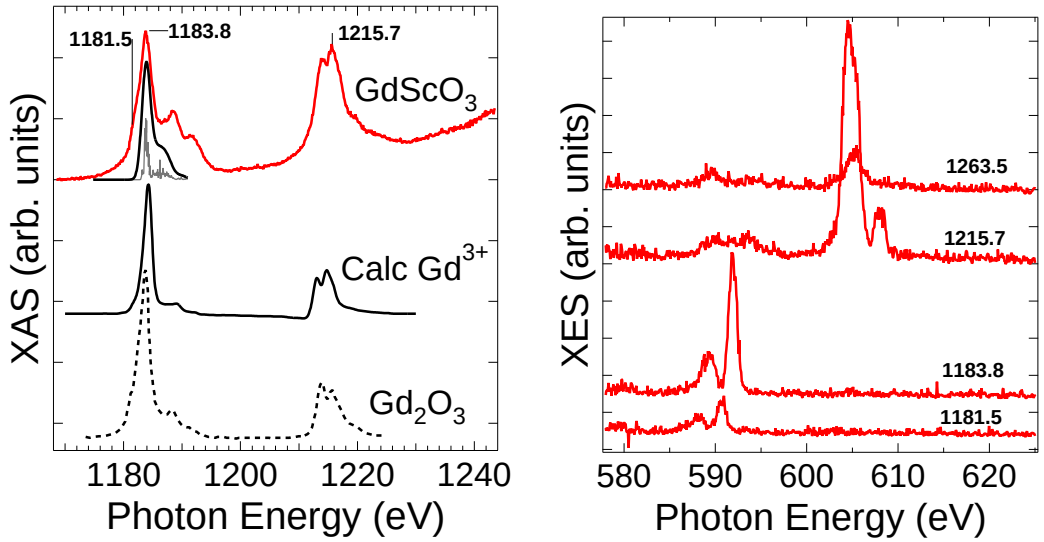

Figure 4.16: Left panel: $GdScO_3$ Gd $M_{4,5}$-edge XAS with Gd_2O_3 reference (Kaindl *et al.*, 1984) (broken black), band structure calculations of unoccupied states of Gd (grey sticks) and Gd^{3+} multiplet calculations from Thole *et al.* (1985) (black solid). Right panel: resonant Gd $4f \rightarrow 3d$ XES in second order.

$DyScO_3$ XAS and XES In the left panel of figure 4.17 the Dy $M_{4,5}$-edge XAS of $DyScO_3$ is presented in comparison with Dy $4f$ band structure calculation and the XAS of the reference compound Dy_2O_3. The M_5-edge of $DySc_3$ at ∼1294 eV is in very good agreement with the reference and the calculations. The clear multiplet structure of M_5-edge in the reference spectra is smeared in the $DyScO_3$ sample and the shoulder at 1298 eV is more intense for the scandate. The calculation gives a similar intensity for the shoulder at 1298 eV as for the scandate. The multiplet states from 1285 eV to 1294 eV are found in both experiments. The shape of the M_4-edge of the scandate agrees with the shape of the reference. These spectra are a clear indication for trivalent Dy atoms in the scandates.

In the right panel of figure 4.17 the XES, excited with energies indicated in the corresponding XAS spectra, is presented. The three lower spectra excited resonantly at the M_5-edge comprise the elastic peak and a small shoulder to lower photon energies which is due to inelastic features excited in resonance. The resonant emission spectrum excited at the M_4-edge at 1328.1 eV shows the weak inelastic structure of the M_5-edge from 642 eV to 652 eV. The elastic peak and resonant excited inelastic features are present at around 663 eV. The pure inelastic structure of the Dy $M_{4,5}$-edge is visible in the normal emission spectra excited with 1363.6 eV. No energy loss features are visible.

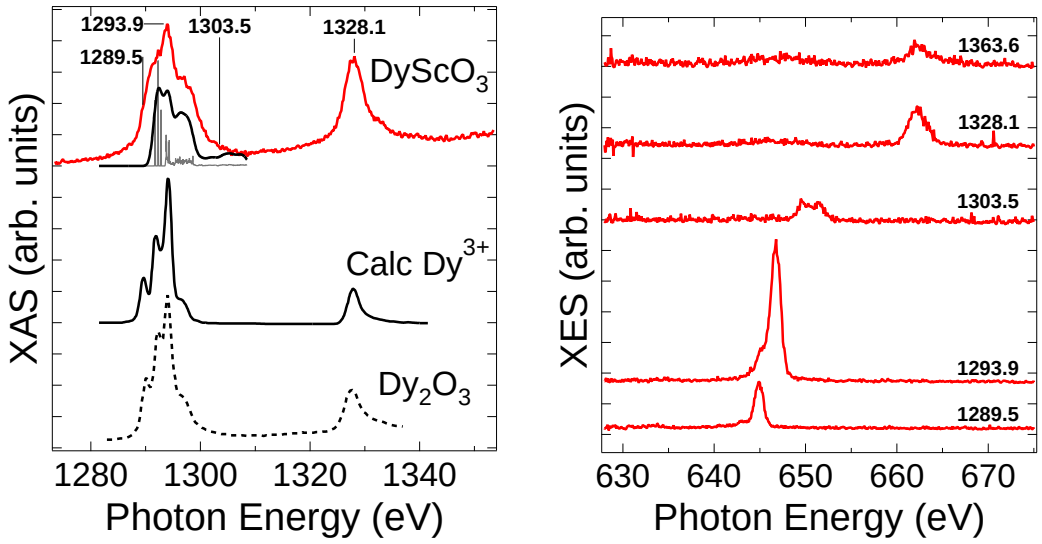

Figure 4.17: left panel: $DyScO_3$ Dy $M_{4,5}$-edge XAS with Dy $4f$ band structure calculation and Dy_2O_3 reference. Right panel: resonant Dy $4f \rightarrow 3d$ XES in second order.

4.7 Discussion

4.7.1 Band gaps with XES and XAS of O K–Edge

The band gap of high-k dielectric materials is important as barrier for the tunnelling of electrons through the thin dielectric layers (see leakage current in section 1.2.3). Therefore the band gap plays an essential role. While x-ray emission spectroscopy is probing the occupied states, x-ray absorption spectroscopy is probing the unoccupied states. Thus XES and XAS are adequate tools for the analysis of band gaps. It should be noted that due to different final states of both methods the charge transfer energy shifts the XAS and XES spectra in energy with respect to each other. The first principles calculations are included in the determination of the band gaps for comparison with the experiment.

There are different methods in literature to obtain band gaps which are comparable with the method that is used here. Very similar is the approach made by Dong *et al.* (2004), where the onset of the O $1s$ XAS and O K–edge XES peaks was taken to determine the band gap of ZnO. Another possibility is given by Hüfner *et al.* (1991) where the band gap of NiO is determined between Fermi level of XPS and the maximum of the first peak of a Bremsstrahlung Isochromat Spectroscopy (BIS) spectrum. The advantages of XAS and XES compared with band structure calculations are that a small density of states at the edge of the band gap are taken into account, but defect states which can broaden the spectra are filtered because they are not present in the calculations. More advantages are that the experiments are made under very similar conditions in a short time range and that the relative calibration of XAS and XES is very precise. A disadvantages is the element specific band gap, but due to the delocalization of the O $2p$ electrons this method is applicable. Another point is the charge transfer energy which can impair the result.

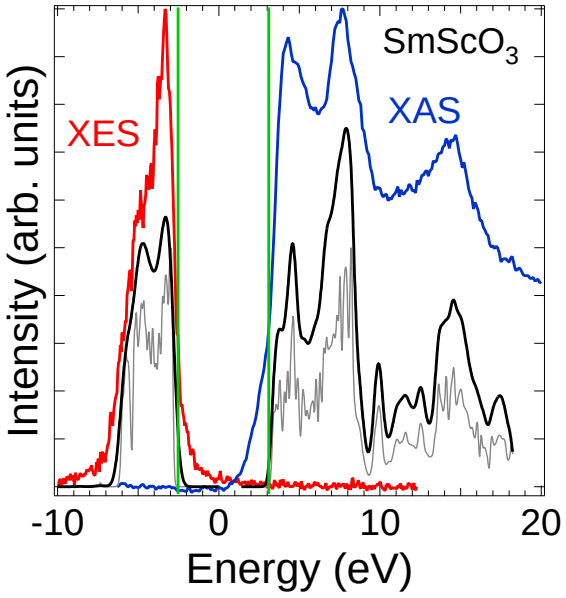

Figure 4.18: Band gap of $SmScO_3$ single crystal by O 1s XAS and O K XES spectra.

As the band gap is formed by rare earth $4f$, $5d$ and scandium $3d$ states hybridized with O $2p$, the LDA+U correction naturally increases the band gap, as is known from many ab initio studies of correlated oxides. The values of band gaps resulting from band structure calculations should not be taken too seriously because of empirical adjustment of the U value. Still, it is comfortable having proceeded from the adjustment, primarily of the $4f$ peak positions in the XP spectra, to arrive at values for the band gaps which are in the range of the results from optical experiments. This yields the conviction that the overall description of the underlying band structure is correct. Also the shape of the calculations is in very good agreement with the shape of the XAS and XES experiments. In the figures 4.18, 4.19 and 4.20 the band gap of the calculations is enlarged by shifting the unoccupied states (1.4 eV for $SmScO_3$, 1.6 eV for $GdScO_3$ and 1.5 eV $DyScO_3$) to achieve perfect agreement with the XA spectra and the XE spectra. To determine the band gap in the experiment the highest occupied and the lowest unoccupied states of the enlarged calculations are used so one can overcome the too small band gap of the calculations. The calculated and experimental values are compared with ultraviolet absorption results (Cicerella, 2006), UV ellipsometry measurements (Lim *et al.*, 2002; Lucovsky *et al.*, 2004) and a combination of internal photoemission and photoconductivity measurements (Afanas'ev *et al.*, 2004) in table 4.2.

In figure 4.18 the O K XES and O $1s$ XAS results for $SmScO_3$ are plotted. The band gap is determined to 5.6 eV from experiment. This value is in good agreement with different results in the literature. Lim *et al.* (2002) found the band gap for a $SmScO_3$ single crystal in the range of 5.5 eV to 6.0 eV by means of far UV spectroscopic ellipsometry. The results of Cicerella (2006) with the same technique, but for a 355.9 nm $SmScO_3$ layer on $LaAlO_3$ produced by pulsed laser deposition determined a band gap of 5.55 eV. While in the same publication a band gap of 5.4 eV was

determined by UV spectroscopy.

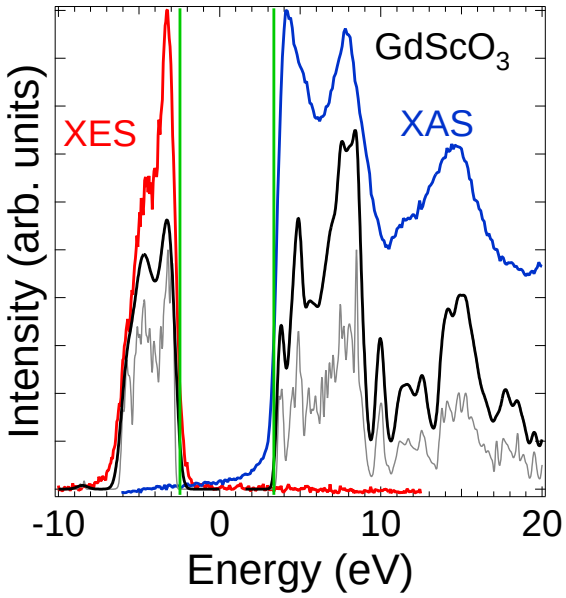

Figure 4.19: Band gap of $GdScO_3$ single crystal by O 1s XAS and O K XES spectra with help of LDA+U calculations.

Results for $GdScO_3$ are shown in figure 4.19. The band gap is 5.8 eV which is in the range of results from the literature. Lim *et al.* (2002) determined a band gap of 6.5 eV with UV ellipsometry for a single crystal while the UV transmission spectrum in the same paper show the absorption onset below 6 eV. Cicerella (2006) found a 5.2 eV band gap with UV spectroscopy on a single crystal. Anisotropic analysis of ellipsometry data for the single crystal gave band gaps closer to 6 eV. VUV spectroscopic ellipsometry data by Lucovsky *et al.* (2004) shows the onset of transitions from the top of valence band, O 2p π non-bonding states at 5.8 eV. Afanas'ev *et al.* (2004) found a 5.6 eV band gap with a combination of internal photoemission and photoconductivity measurements.

Figure 4.20 shows the XES and XAS results for $DyScO_3$. The band gap is determined to 5.9 eV. This is in good agreement with the results of Cicerella (2006) finding a band gap of 5.3 eV for a single crystal with UV transmission spectroscopy. Afanas'ev *et al.* (2004) determined a band gap of 5.7 eV with a combination of internal photoemission and photoconductivity measurements.

For a more complete overview of band gaps in rare earth scandates the O 1s XAS and O K XES of $NdScO_3$ and $TbScO_3$ single crystals are presented in figure 4.21. These results were already presented in the diploma thesis of Derks (2008). In $NdScO_3$ the trivalent Nd ions has $4f^3$ configuration and the trivalent Tb ion $TbScO_3$ has $4f^8$ configuration. No band structure calculations were available for these two compounds. Therefore the band gaps has to be determined from the XAS and XES experiment as made by Dong *et al.* (2004) for poly and single crystalline ZnO where the onset of the O 1s XAS and O K–edge XES peaks was taken to determine the band gap. This method is improved by the comparison with the spectra and calculations of $SmScO_3$,

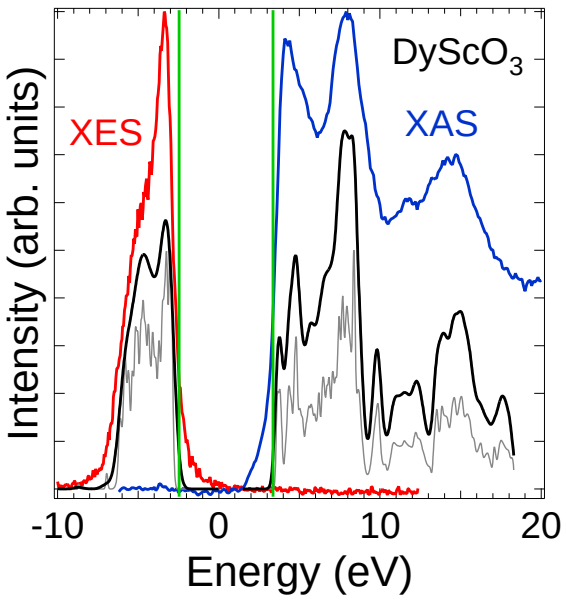

Figure 4.20: Band gap of $DyScO_3$ single crystal by O 1*s* XAS and O *K* XES spectra.

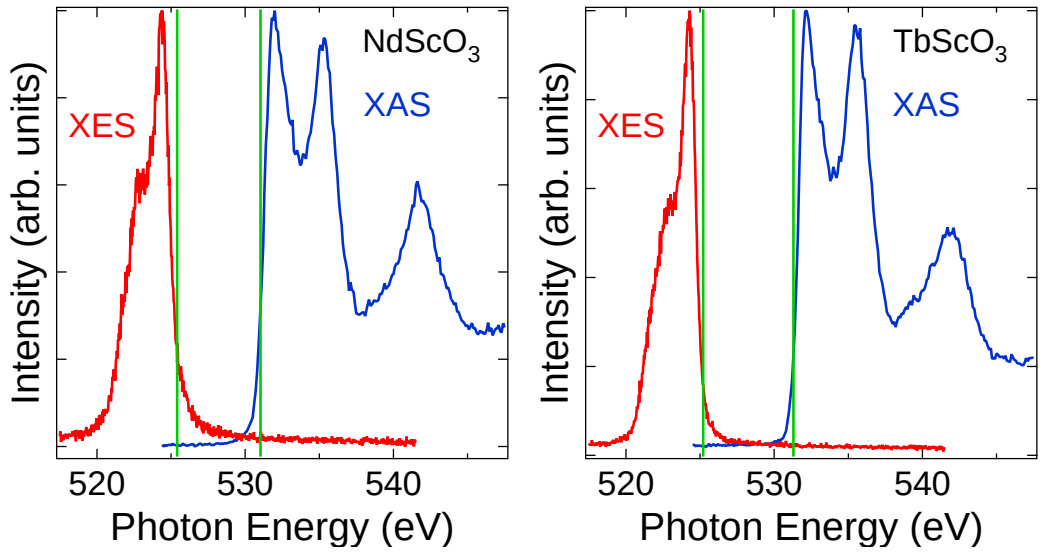

Figure 4.21: Band gap of $NdScO_3$ and $TbScO_3$ single crystals by O 1*s* XAS and O *K* XES spectra.

$GdScO_3$ and $DyScO_3$ to get rid of broadened absorption edges due to defects. For $NdScO_3$ a band gap of ∼5.6 eV is found and for $TbScO_3$ the band gap is ∼6.1 eV. The value for $NdScO_3$ is in agreement with the result found by Cicerella (2006) by ultraviolet absorption. For $TbScO_3$ the value found by Cicerella is 0.5 eV smaller. In Cicerella's work band gaps of 5.5 eV for $NdScO_3$ and 5.6 eV for $TbScO_3$ were found for thin film samples deposited on $LaAlO_3$ by pulsed laser deposition.

Table 4.2: Band gaps of $NdScO_3$, $SmScO_3$, $GdScO_3$, $TbScO_3$ and $DyScO_3$ experimental and theoretical results in comparison with literature.

	$NdScO_3$	$SmScO_3$	$GdScO_3$	$TbScO_3$	$DyScO_3$
Cicerella (2006) bulk		5.4 eV	5.2 eV		5.3 eV
thin film	5.5 eV			5.6 eV	
Lim *et al.* (2002)		5.5 - 6.0 eV	6.5 eV		
Afanas'ev *et al.* (2004)			5.6 eV		5.7 eV
Lucovsky *et al.* (2004)			5.8 eV		
present work LDA+U		4.2 eV	4.2 eV		4.4 eV
experiments	5.6 eV	5.6 eV	5.8 eV	6.1 eV	5.9 eV

In table 4.2 the results for the band gap determined by XAS and XES is compared with literature data. Different results can be understood if one takes into account the differences of the techniques and their interpretation. The band gap is defined as the energetic difference between the highest occupied and the lowest unoccupied state in the ground state. In experiments the initial state is usually the ground state, while the final state differs for various techniques. For XPS and XES the final state is a $N-1$ electron state where one electron has left the atom. During the XAS process the electron stays in the atom and the final state is a N electron state. A different charge of the final states in XPS and XAS processes implies a need to introduce a correction in order to permit a superposition of both in the common energy scale. The correction becomes larger the more "dense" the core states are. Consequently the difference (correction) is large in R $4f$, but negligible in O $2p$ (weak localization) and in Sc $3d$ (empty d-shell), the states which essentially flank the band gap.

The band gaps determined by XAS in comparison with XES are correlated to the crystallographic structure of the rare earth scandates. The crystallographic parameters of the whole family of rare earth scandates was investigated in detail by Liferovich and Mitchell (2004). Essential for the band gap are the ScO_3 octahedra, because Sc and O are strongly hybridized and the rare earth ions are less included in this hybridization. The correlation between the mean distance determined by Liferovich and Mitchell (2004) and the band gaps determined by XAS and XES can be seen in figure 4.22.

In the molecular orbital theory it is known that the splitting of molecular oribtals depends on the hybridization and the distance between the atoms of the molecule. The correlation between the band gap and the Sc–O distance can be seen in equation 4.1

$$\mathrm{Gap} - \mathrm{ScO}_{\mathrm{Gap}} = const. \times \exp[-\alpha(d - d_0)], \tag{4.1}$$

where Gap is the band gap of the hybridized Sc–O states and $\mathrm{ScO}_{\mathrm{Gap}}$ the band gap

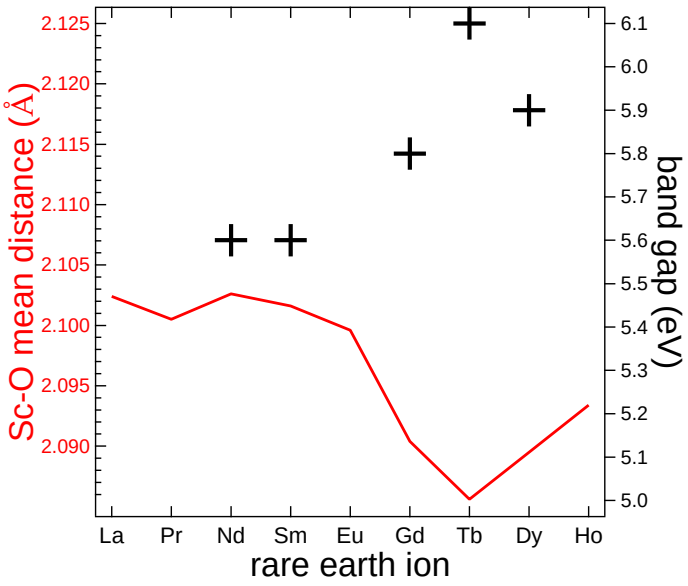

Figure 4.22: Sc-O mean distance of rare earth scandates from Liferovich and Mitchell (2004) and band gaps determined by XAS and XES.

of isolated Sc–O states as depicted in figure 4.23. d is the mean distance between the hybridized Sc and O atoms.

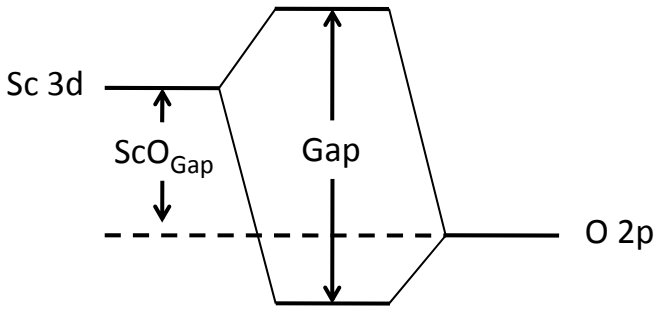

Figure 4.23: Molecular orbitals of hybridized Sc and O atoms.

In figure 4.24 the logarithm of the difference of the hybridized and the separated band gap is plotted over the Sc–O distances. The best linear fit was found with a ScO_{Gap} of 5.5 eV and a d_0 of 0.2080 nm.

The found constants ScO_{Gap} and d_0 can now be substracted from the determined band gap and the Sc–O distances from the literature. In figure 4.25 the resulting values are normalized and a very good agreement between the band gap and the Sc–OO distance is visible.

In conclusion, the band gaps determined by XAS and XES in combination with LDA+U calculations give data which are in good agreement with different results from the literature (see Table 4.2). The $GdFeO_3$-like distortion of the perovskite structure

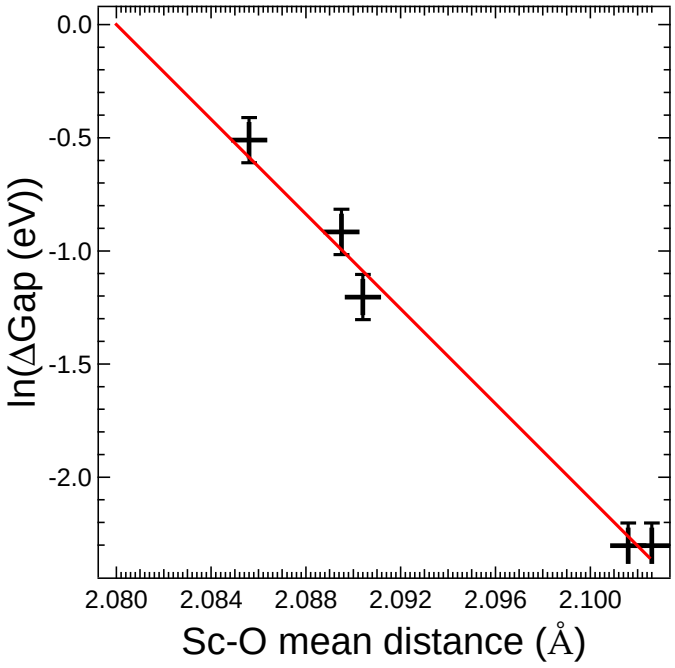

Figure 4.24: Logarithmic plot of the ΔGap over Sc-O mean distance of rare earth scandates with a linear fit.

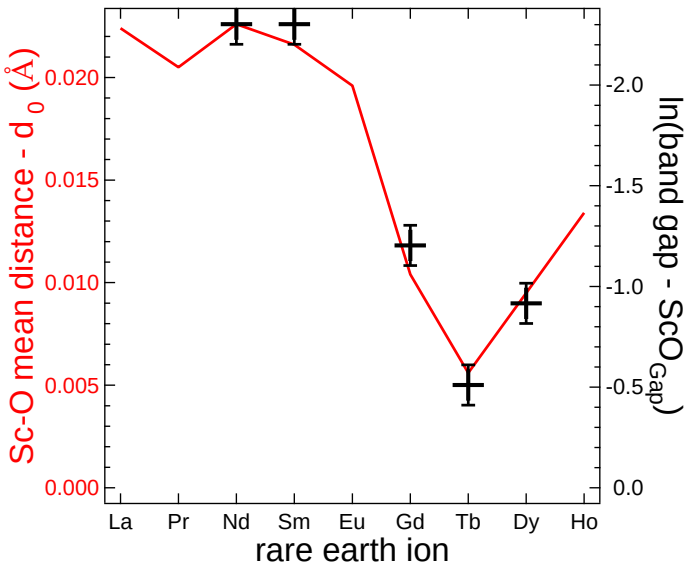

Figure 4.25: ln(ΔGap) and Sc-O mean distance of rare earth scandates.

plays a key role in the formation of the band gap because the Sc–O distances are influenced by the distortion (see figure 4.25).

4.7.2 Valence Band: Calculations compared with XPS and XES

The valence band is the most important part of the electronic structure, because the bonding and the interaction between atoms of the crystal appears in this energy region. Many important properties and effects are based on the structure of the valence band below the Fermi level and the conduction band above the Fermi level. With XPS the total density of the occupied states is probed while XES probes the partial density of occupied states, which means that this technique is element–specific. In this section the experimental total and partial density of states are compared with band structure calculations to identify different features in and their contribution to the valence band.

The XPS valence band spectra of $SmScO_3$, $GdScO_3$ and $DyScO_3$ are plotted in Fig. 4.26. The experiments are compared with the results of *ab initio* band structure calculations, namely the total density of states from a GGA calculation which gives the best agreement with the experiment for the on-site Coulomb potential U=0.4 Ry=5.4 eV. The calculation with a bigger U value are also presented. The U values mainly influence the position of the RE $4f$ states. The excitation ($N-1$ electrons) during the XPS process is not included in the calculations (N electrons). Hence the localized states at ~ -30 and ~ -20 eV in the calculations are located closer to the Fermi level than in the XPS measurements. Additionally multiplet effects are not included. The valence band region is constituted by rare earth $4f$, $5p$, $5d$ and scandium $3p$, $3d$, $4s$ and oxygen $2p$, $2s$ states. These states have different photoionization crosssections, which should be taken into account for weighting the corresponding contributions to the total DOS. Specifically, we took the relative photoionization crosssection values, corresponding to the excitation energy of 1486.6 eV, from Scofield (1976). The weights tabulated therein, which refer to each respective electronic shell as a whole, were normalized to a single electron and then multiplied with partial densities of states and with the number of atoms of each type in the unit cell, giving the calculated spectral intensity which is compared to the experiment. Then the calculated total density of states was convoluted with a 0.45 eV Gaussian and a 0.5 eV Lorentzian for experimental and lifetime broadening, respectively.

The XPS valence band region of $SmScO_3$ comprises eight distinct features a-h (top of Fig 4.26). Features a, b and c are located at -3.5, -5.0 and -7.5 eV on an energy loss scale, followed by a shoulder at -9.5 eV (d). The O $2p$ states are located from -3 eV to -5 eV, while the Sm $4f$ multiplet is found in the features b, c and d. The next group of features e, f and g is located at -19.5 eV, -21.5 eV and -24.5 eV. In this region the O $2s$ states take place around -22 eV and the Sm $5p$ multiplet reaches from -19 eV to -25 eV. At -30.5 eV the feature h appears which corresponds to Sc $3p$ states. The experiment is very well reproduced by the calculation with $U = 0.4$ Ry beside the intensities of Sm $4f$ multiplet features b, c and d. For U=0.8 Ry the calculated Sm $4f$ states are less split and appear too far away from the Fermi level.

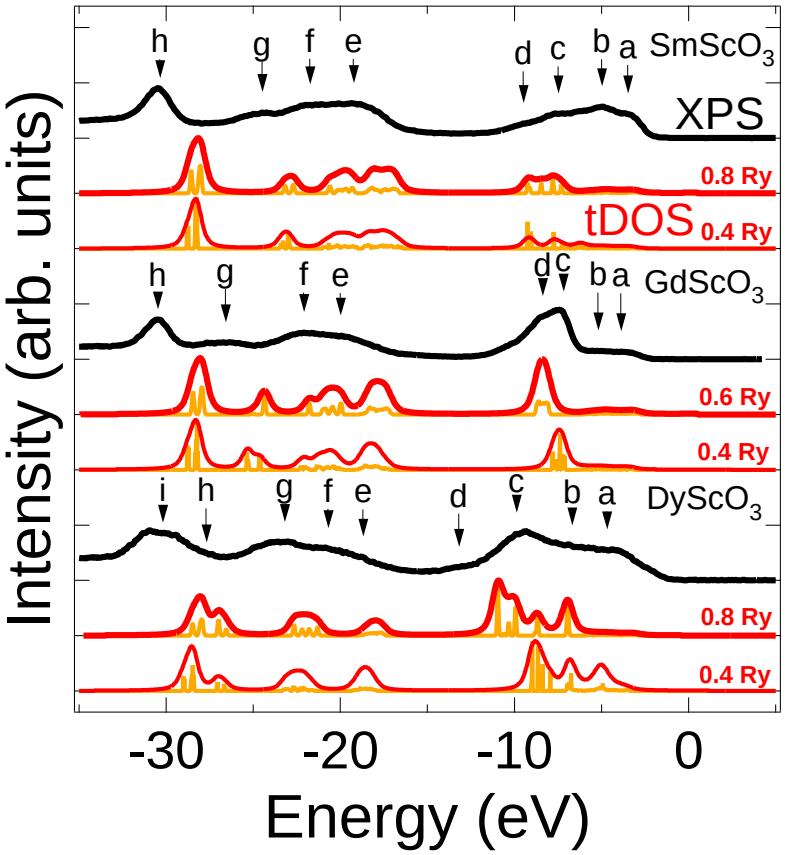

Figure 4.26: XPS in the valence band region of $SmScO_3$, $GdScO_3$ and $DyScO_3$ compared with band structure calculations and the Gd 5*p* multiplet (Thole *et al.*, 1993).

Also the XPS valence band region of $GdScO_3$ consists of eight features a-h (middle of Fig 4.26). The four features close to the Fermi level are a, b, c and d at −4.0, −5.5, −7.5 and −8.5 eV. The O 2*p* states are located at −3 eV to −5.5 eV (a, b), while the Gd 4*f* states are relatively localized at −7.5 eV to −8.5 eV (c, d). Features e and f are located at −20.0 eV and −22.0 eV, followed by a relatively small feature g at −26.5 eV. The O 2*s* states are at around −22 eV and the Gd 5*p* multiplet reaches from −18 eV to −26.5 eV which can be seen also from the Gd 5*p* multiplet (Thole *et al.*, 1993). The Sc 3*p* feature h takes place at −30.5 eV. Features a-d close to the Fermi level are in very good agreement with both calculations. The intensities of features e and f are reversed in the calculation with respect to experiment, whereas the g and h features are reproduced well.

Finally the XPS valence band $DyScO_3$ consists of nine features a-i. Features a, b and c are located at −4.5 eV, −7.0 eV and −9.0 eV, followed by a shoulder at −13.0 eV (d). From −3 eV to −5 eV the O 2*p* states take place. The Dy 4*f* multiplet comprises of the features b, c and d. Features e, f and g take place at −18.5, −20.5 and −23.0 eV. O 2s states are located at around −22 eV. The Sc 3*p* feature i at −30.5 eV has a prepeak h at −27.5 eV. The Dy 5*p* multiplet reaches from −18.5 eV to −27.5 eV. The Dy 5*p* multiplet reaches from −18.5 eV to −27.5 eV.

The three features a, b and c near the Fermi level are reproduced by the calculation with U=0.8 Ry a little bit too far away from the Fermi level, but the calculation with U=0.4 Ry is in perfect agreement. Multiplet feature d is missing in calculations. Features e, f and g are calculated as two separated peaks. Feature i and the prepeak h are in very good agreement with the calculation.

In general the shape of the XPS measurement is reproduced by the calculations in a satisfactory way. However, there are some differences in detail. The comparison for $GdScO_3$ and $DyScO_3$ shows a difference at the group of features around −20 eV. The comparison of the states closer to the Fermi level reveals differences for $SmScO_3$ by rendering the rare earth $4f$ multiplet in position and splitting. Also the $DyScO_3$ calculations with U=0.8 show the $4f$ states shifted away from the Fermi level. The position of the rare earth $4f$ states is influenced by the choice of the U parameter. Other differences arise from the fact that the calculations did not include multiplet effects which are more important for rare earth atoms than for oxygen and scandium atoms.

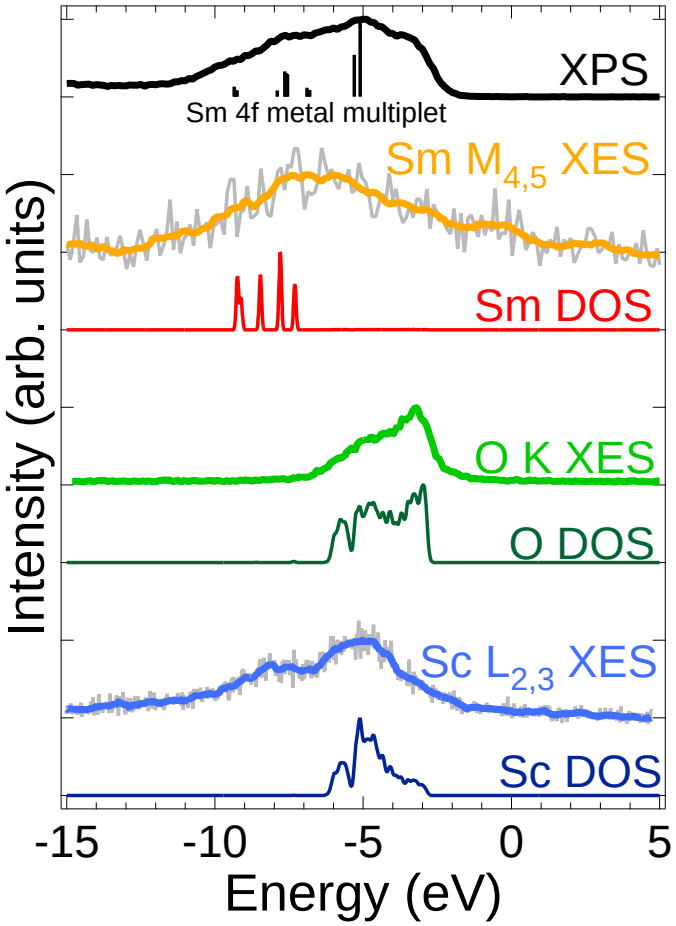

Figure 4.27: XPS spectra of $SmScO_3$ compared with XES and calculated densities of states. Multiplet calculation of trivalent Sm $4f$ states is taken from Lang *et al.* (1981).

Now a detailed comparison between XPS valence band, XES and pDOS of the

calculations is presented. In Figure 4.27 the XE spectra of Sm $M_{4,5}$, O K and Sc $L_{2,3}$ are displayed with corresponding partial DOS from the GGA+U calculations. Below the XPS valence band spectra of $RScO_3$ the rare earth $4f$ multiplet calculations of Lang *et al.* (1981) are plotted. This calculations are using the Russel-Saunders spin–orbit coupling scheme for comparison with XPS valence band spectra of trivalent rare earth metals. Comparable calculations are made by Gerken (1983). The XE spectra have been plotted on a common energy scale with the XPS valence band by using corresponding XPS core level binding energies for calibration (Sm $3d$: 1109.5 eV, O $1s$: 530.0 eV, and Sc $2p$: 401.5 eV). The Sm $M_{4,5}$ XE spectrum consists of Sm $4f$ features from −2 eV to −11 eV with a maximum at −6 eV. The calculated partial DOS has four features from −7 eV to −10 eV. These features can be seen in the experiment with bigger energy separation. This structure is better rendered by the multiplet calculation of trivalent Sm $4f$ states, that also shows the main peak at −5 eV.

The O K XE spectrum has two features at −3.0 eV and −5.0 eV. These features agree with the calculated O $2p$ states and are strongly hybridized with Sc $3d$ states. The −5.0 eV feature has more d character and the −3 eV feature has more p character what is in agreement with the results of Winiarski *et al.* (1994) finding more d character for higher binding energy for $KTaO_3$ and $KNbO_3$ single crystals. The Sc $L_{2,3}$ XE spectrum comprises three features at −3.0 eV, −5.0 eV and −8.0 eV. The −3.0 eV and −5.0 eV features are due to the hybridization between O $2p$ and Sc $3d$ while here the d-character at higher binding energy is clearly seen. The third feature at −8.0 eV is not covered by the calculation, because it is due to the spin–orbit splitting of Sc $2p$ core level of ∼4 eV. But this cannot completely explain the shape and energetic position of this feature. It is not clear if there is another feature due to an interaction between Sc and Sm which might be a d state coupling that was formerly found for complex oxides (Wilk *et al.*, 2001; Lucovsky *et al.*, 2004; Liferovich and Mitchell, 2004).

Also the XE spectra of $GdScO_3$ are compared with the XPS valence band and pDOS calculations (Fig. 4.28). Below the XPS valence band spectrum the calculation of trivalent Gd $4f$ multiplets from Lang *et al.* (1981) is plotted. XPS core level energies have been used to get a common energy scale (Gd $3d$: 1189.5 eV, O $1s$: 530.0 eV, Sc $2p$: 401.5 eV). The Gd $M_{4,5}$ XE spectra comprises an intense feature at −8.0 eV with a shoulder at −6.0 eV. The main feature is perfectly rendered by the band structure calculation, but the shoulder closer to E_F is missing in the calculation. This is in comparison with the multiplet calculation of trivalent Gd $4f$ states. The O K XES has a O $2p$ main feature at −3.5 eV with a shoulder at −5.0 eV. Here again the p character at the −3.5 eV feature is visible. The calculations show O $2p$ levels in correct position and shape. The Sc $L_{2,3}$ XE spectrum consists of three features, a Sc $3d$ feature at −5.0 eV with a shoulder at −3.5 eV, and a small shoulder from −7.5 eV to −10 eV which is due spin–orbit splitting of the Sc $2p$ (∼4 eV). As discussed before an interaction between Sc and Gd is possible, but weaker than for $SmScO_3$. The calculation shows the Sc $3d$ features at −3.5 eV and −5.5 eV, but the feature around −9 eV is missing.

In Figure 4.29 the XES experiments of $DyScO_3$ are shown, along with the band structure calculated partial densities of states. The common energy scale is achieved

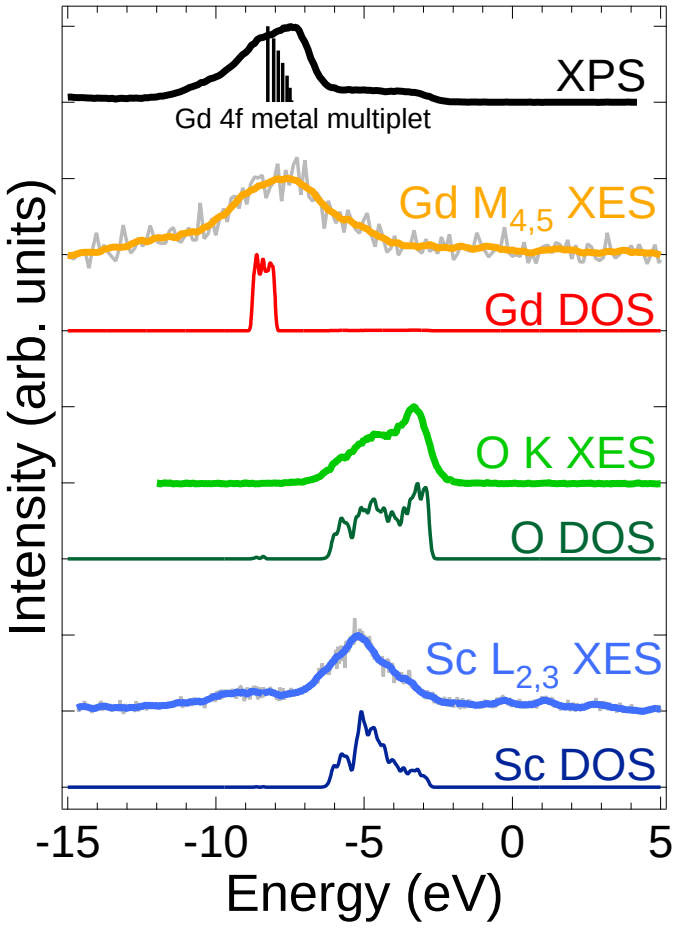

Figure 4.28: XPS spectra of $GdScO_3$ compared with XES and calculated densities of states. Multiplet calculation of trivalent Gd $4f$ states is taken from Lang *et al.* (1981).

by use of the XPS core level energies (Dy $3d$: 1296.0 eV, O $1s$: 530.0 eV, Sc $2p$: 401.5 eV). Multiplet calculations of trivalent Dy $4f$ states (Lang *et al.*, 1981) is plotted below the XPS VB spectrum. The Dy $M_{4,5}$ XE spectra comprises four Dy $4f$ features at −5.0 eV, −7.0 eV, −9.0 eV and −13.0 eV. The three features from −5.0 eV to −9.0 eV are calculated at too high binding energy and the feature at −13.0 eV is missing in the calculation which is due to not included multiplet effects. The multiplet calculation of dy $4f$ metal gives a better agreement with the Dy states. In the O K XE spectrum the O $2p$ main feature at −3.5 eV with a shoulder from −5.0 eV to −7.0 eV is in good agreement with the calculation. The Sc $L_{2,3}$ spectrum is due to O $1s$ hybridization and consists of a peak at −5.0 eV with a shoulder at −3.5 eV and a smaller peak at −8.0 eV. As discussed for the other samples, this is due to the spin–orbit splitting of Sc $2p$. The interaction between Sc and Dy might be smaller than for $SmScO_3$ but larger than for $GdScO_3$. The calculation renders the peaks at −3.5 eV and −5.0 eV. Here again the d character at −5.0 eV and the p character at −3.5 eV is clearly visible in agreement with results of Winiarski *et al.* (1994) as mentioned above. The electronic structures of $SmScO_3$, $GdScO_3$ and $DyScO_3$ are

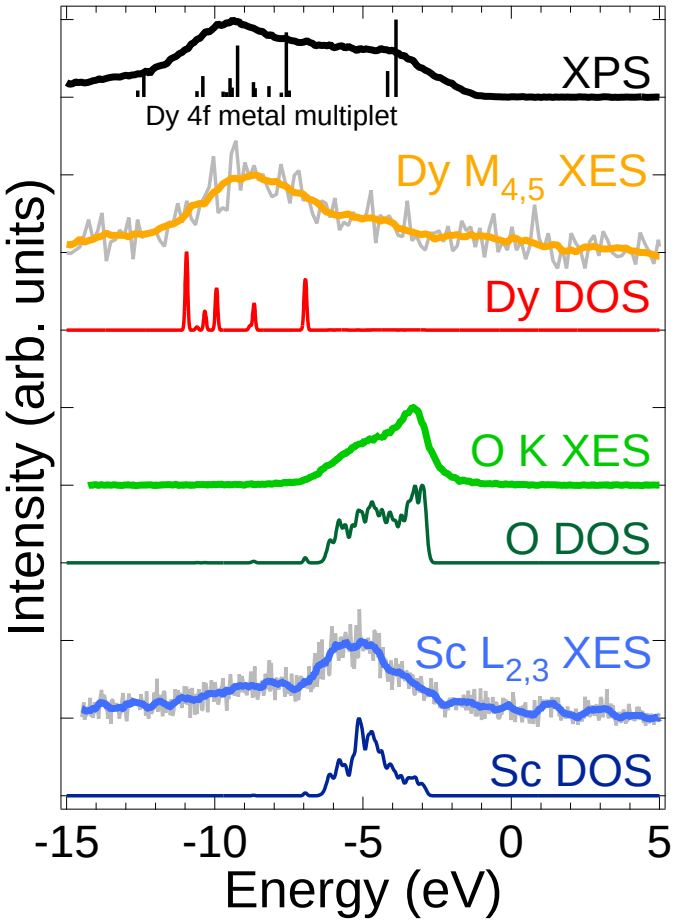

Figure 4.29: XPS spectra of $DyScO_3$ compared with XES and calculated densities of states. Multiplet calculation of trivalent Dy $4f$ states is taken from Lang *et al.* (1981).

very similar. In the range from -3 eV to -5 eV there are O $2p$ states which are hybridized with Sc $3d$.

The main content of the valence band are the rare earth $4f$ levels, which are located at -7.5 eV for Gd. For the Sm and the Dy compounds the RE $4f$ levels are more multiplet–split in the range from -6 eV to -10 eV for Sm and from -5 eV to -9 eV for Dy. The band structure calculations show some difference to the RE $4f$ states due to multiplet splitting of $4f$ states and the high U values which are necessary for a band gap which is free from RE $4f$ states. This is visible by comparing multiplet calculations for trivalent rare earth $4f$ states with the experimental data. The less multiplet–split O and Sc states are in very good agreement with the band structure calculations. An interaction between Sc and RE atoms might be present in the Sc $L_{2,3}$ XE spectra at around -8 eV. Such a hybridization was found for $DyScO_3$ and $GdScO_3$ by Lucovsky *et al.* (2004) and for $AScO_3$ perovskite alloys by Halilov *et al.* (2004).

4.8 Conclusions

In conclusion, magnetic and electronic properties of the rare earth scandates ($SmScO_3$, $GdScO_3$ and $DyScO_3$) were investigated. The superconducting quantum interference device (SQUID) measurements reveal antiferromagnetic coupling at 2.96 K ($SmScO_3$), 2.61 K ($GdScO_3$), and 3.10 K ($DyScO_3$). For $DyScO_3$ a Rietveld refinement of a 2 K neutron diffraction data set gives an antiferromagnetic spin arrangement of Dy in the *Pbnm* structure (Shubnikov group: $Pb'n'm'$). The band structure calculations (LDA+U) give rise for a coupling between Sc 3d, RE 5d and O 2p states. With x-ray photoelectron core level spectroscopy of rare earth scandates in comparison with reference samples determines the valence state of rare earth atoms to be 3+, of scandium atoms to be 3+ and of oxygen atoms to be 2-. Multiplet splitting of RE 4d states was observed. X-ray absorption spectroscopy in comparison with the band structure calculations (RE $M_{4,5}$) and multiplet calculations (Sc $L_{2,3}$) are in agreement with the results of x-ray photoelectron spectroscopy. With resonant x-ray emission spectroscopy the occupied states in the valenceband were observed element specific and no loss features and therefore no excitations at E_F were visible due to the band gap. With x-ray absorption and emission spectroscopy at the O K-edge in comparison with band structure calculations of the unoccupied oxygen states, the band gaps of $NdScO_3$, $SmScO_3$, $GdScO_3$, $TbScO_3$ and $DyScO_3$ are determined to 5.6 eV, 5.6 eV, 5.8 eV, 6.1 eV and 5.9 eV, respectively. These values are corresponding to the Sc–O mean distances. The comparison of x-ray photoelectron spectroscopy of the valence band, normal x-ray emission and band structure calculations give a good agreement between experiment and calculations. A small mismatch between band structure calculations and experiment for rare earth 4f states is due to multiplet splitting which agrees with trivalent rare earth multiplet calculations. A strong hybridization between Sc 3d and O 2p states was observed, as predicted by the calculations. The rare earth d-states may play a role in this complex hybridization.

Chapter 5

$LuFe_2O_4$

5.1 Introduction

Magnetoelectric coupling and multiferroics in spintronics is a rapidly emerging area of research, where a number of possible device architectures have been proposed (Binek and Doudin, 2005). Recent proposals to develop novel multifunctional storage components for microelectronics have led to an intense interest in materials in which ferroelectric and magnetic order parameters are coupled (Cohen, 2000; Hill, 2000). Devices fabricated from such multiferroic materials could store information through both the electric and the magnetic polarization of the bit, providing an additional degree of freedom in designing memory elements. Furthermore, magnetodielectric coupling in multiferroics may be particularly useful in designing devices to read magnetic storage systems. Current read heads rely on magnetoresistive materials, which generate heat and are sensitive to thermal noise. Capacitive readings under magnetic fields can be accomplished with no or very small amounts of heat produced, and capacitance measurements can be more sensitive than resistive measurements, which could allow the magnetic bit density to be increased. $LuFe_2O_4$ (LFO) seems to be a promising candidate for such applications because of its giant room temperature magneto dielectric response (Subramanian *et al.*, 2006), which suggests a strong coupling between spin moment and electric dipole at room temperature. This giant magneto capacitance is due to charge ordering of Fe^{2+} and Fe^{3+} ions (Xiang and Whangbo, 2007). In ferroelectric crystals this spontaneous polarization is arising from the arrangement of electric dipoles. First-principles calculations (Cohen, 1992; Sághi-Szábo *et al.*, 1998) and electron density analysis (Kuriowa *et al.*, 2001) of ferroelectric materials have revealed that the covalent bond between the anions and cations, or the orbital hybridization of electrons on both ions, plays a key role in establishing the dipolar arrangement. However, for LFO an alternative model, electronic ferroelectricity (Portengen *et al.*, 1996), has been confirmed (Ikeda *et al.*, 2005b) in which the electric dipole depends on electron correlations, rather than on the covalence. This would offer the attractive possibility of ferroelectric materials which could be controlled by the charge, spin and orbital degrees of freedom of the electron. This material is not only of interest for application, it is a challenge to understand basic properties of multiferroic materials. The basic coherences are just partly understood. Several competing interactions, like charge and orbital ordering,

exchange coupling, give the chance to clarify the nature of these effects. Another controversial discussed question is the antiferro magnetic coupling of the iron ions. On one hand magnetic measurements suggest an averaged iron moment at the Fe ions on a triangular net arranged ferrimagnetically (Iida *et al.*, 1993), on the other hand Mössbauer (Sugihara *et al.*, 1978) and neutron diffraction (Lang *et al.*, 1981) studies suggest Fe^{2+} and 1/3 of Fe^{3+} make up majority spin and 2/3 of the Fe^{3+} make up minority spin. The latter magnetic ordering was confirmed by additional Mössbauer, neutron and magnetization measurements (Siratori *et al.*, 1992) leading to the spin and charge order model depicted in the left panel of figure 5.1.

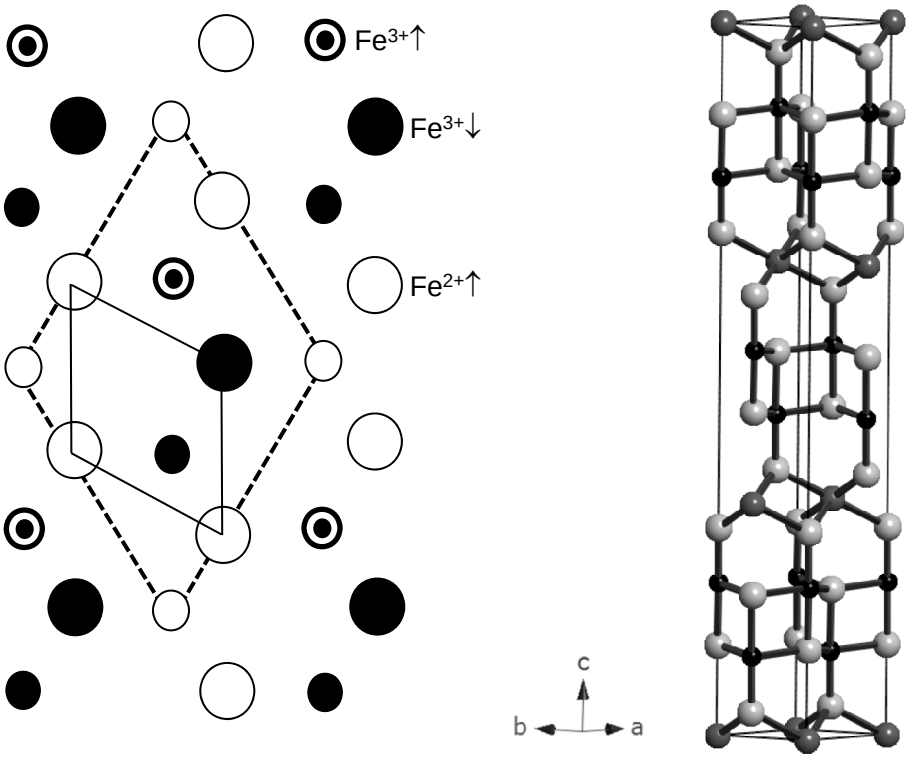

Figure 5.1: Left: Spin and charge ordering model in a W-layer of $LuFe_2O_4$ (Siratori *et al.*, 1992) adopted from Ikeda *et al.* (2005a). The solid line marks the chemical unit cell while the dotted line represents a superlattice cell. Large and small circles distinguish between upper and lower triangular plane of a W-layer, respectively. White circles represent Fe^{2+} ions with majority spin. Black circles and double circles stand for Fe^{3+} ions with minority and majority spin, respectively. Right: Hexagonal double layered structure of $LuFe_2O_4$ in trigonal spacegroup $R\bar{3}m$ (Lu dark grey, Fe black, O light grey). Adopted from Subramanian *et al.* (2006).

The crystal structure of LFO was measured by Isobe *et al.* (1990) by means of x-ray diffraction. The layered structure has $R\bar{3}m$ symmetry. The crystal consists of double layers of Fe ions trigonal bipyramidal surrounded by O ions. Between these double layers a layer of Lu ions surrounded by O octahedra is present.

The XPS measurements were performed at the *University of Osnabrück* with the photoelectron spectrometer PHI 5600ci as described in section 2.6.1. The XAS,

XMCD and XES/RXES measurements were performed at the *Advanced Light Source* in Berkeley, USA, at the beamlines 8.0.1 and 4.0.2 (see section 2.6.4). The experiments on LFO presented in this work are partly performed in collaboration with Christine Derks and therefore already presented in her diploma thesis (Derks, 2008). The multiplet calculations in c_{3i} symmetry were performed in collaboration with Christian Taubitz from the University of Osnabrück.

5.2 Valence State of Fe Ions by Core Level XPS and XAS

The formal valence states of ions in $LuFe_2O_4$ are Lu^{3+}, O^{2-} and resulting from this $Fe^{2.5+}$. XPS measurements (Derks, 2008) of the Fe $2p$ and Fe $3s$ (see figure 5.2) core level confirmed this assumption.

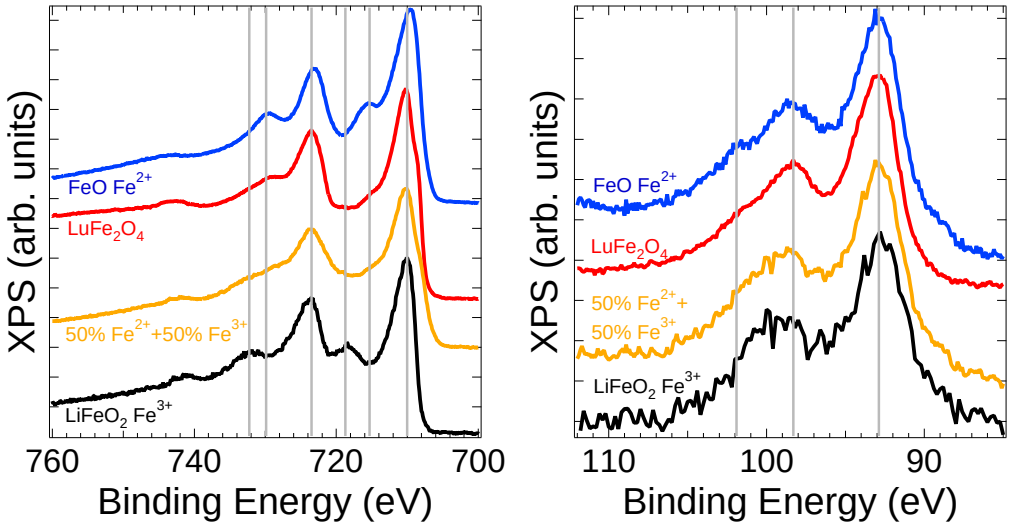

Figure 5.2: XPS measurements of Fe $2p$ (left panel) and Fe $3s$ (right panel) of $LuFe_2O_4$ in comparison with Fe^{2+} and Fe^{3+} reference compounds and a mixture of them.

Fe $2p$ XPS results were published by Park *et al.* (2007) with worse resolution than this measurements. They fitted the Fe $2p_{3/2}$ main peak and found equal contribution of Fe^{2+} and Fe^{3+}. The chemical shift of the Fe $2p$ is so small that it is better to take into account the satellites. In the left panel of figure 5.2 the main features are marked with grey lines. The Fe^{2+} and Fe^{3+} satellites of the reference compounds can give as 50%-mixture the Fe $2p$ XPS structure of LFO. In the right panel of figure 5.2 the same procedure was made for the Fe $3s$ XPS spectra with the same result.

The valence state of Fe has also an influence on the shape and energy position of XA spectra. In figure 5.3 the XAS of $LuFe_2O_4$ is presented in comparison with reference compounds Fe_2O_3 (Fe^{3+}) and FeO (Fe^{2+}). The measurements of $LuFe_2O_4$ were carried out in total electron yield (TEY) and total fluorescence yield (TFY). The TFY is less surface sensitive than the TEY because photons are measured instead of electrons and the escape depth of photons is higher than the escape depth of

electrons. Due to self–absorption of the light, the L_3–edge is underestimated in the TFY measurement and the L_2–edge is more intense than in TEY measurements. The

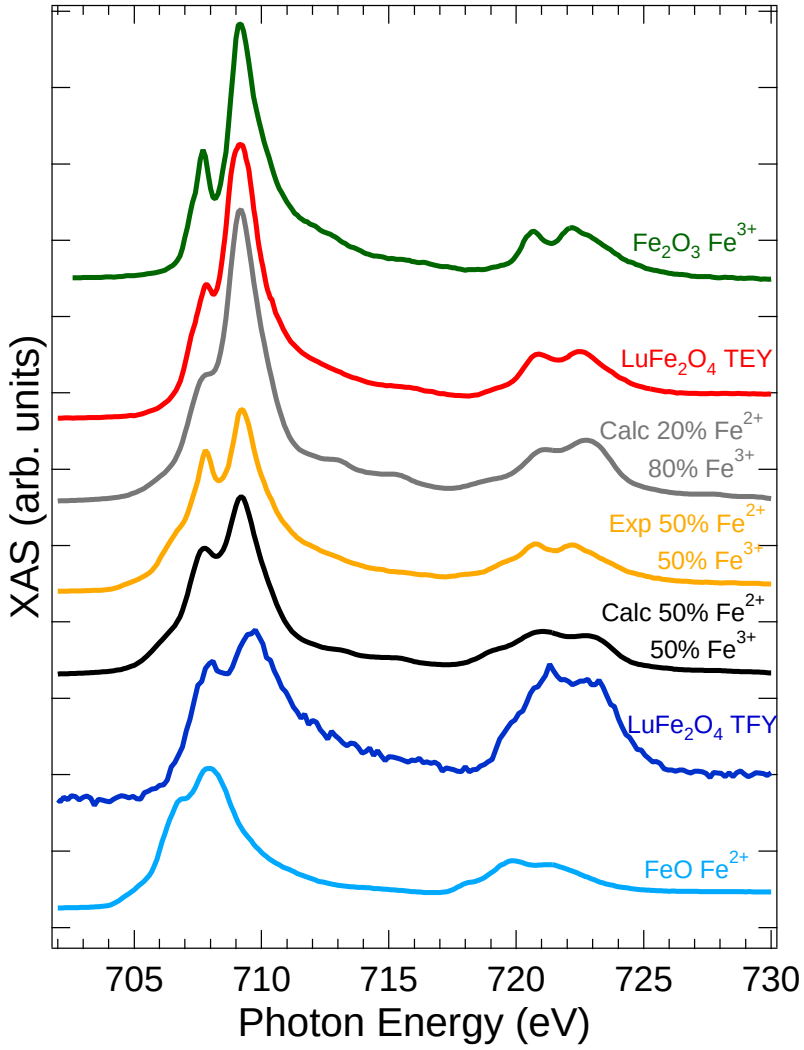

Figure 5.3: XAS measurements in total electron yield (TEY) and total fluorescence yield (TFY) at the Fe L-edge of $LuFe_2O_4$ in comparison with Fe^{2+} and Fe^{3+} reference compounds, a mixture of the reference spectra and multiplet calculations.

TEY XAS of $LuFe_2O_4$ in figure 5.3 is in best agreement with multiplet calculations with 20% Fe^{2+} and 80% Fe^{3+}. The more bulk sensitive TFY measurement is in good agreement with multiplet calculations with 50% Fe^{2+} and 50% Fe^{3+} and with a 50%-50% mixture of the reference compounds.

These measurements show that the surface of the sample is dominated by Fe^{3+} ions and the bulk is in the expected 50%-50% valence state. Although the more surface sensitive XPS measurement show no domination of the trivalent iron the XPS and XAS results fit together because the LFO sample for XPS measurements was cleaved in situ while in the XAS chamber no cleaving device was available.

5.3 RXES at the Fe L–Edge and the O K–Edge

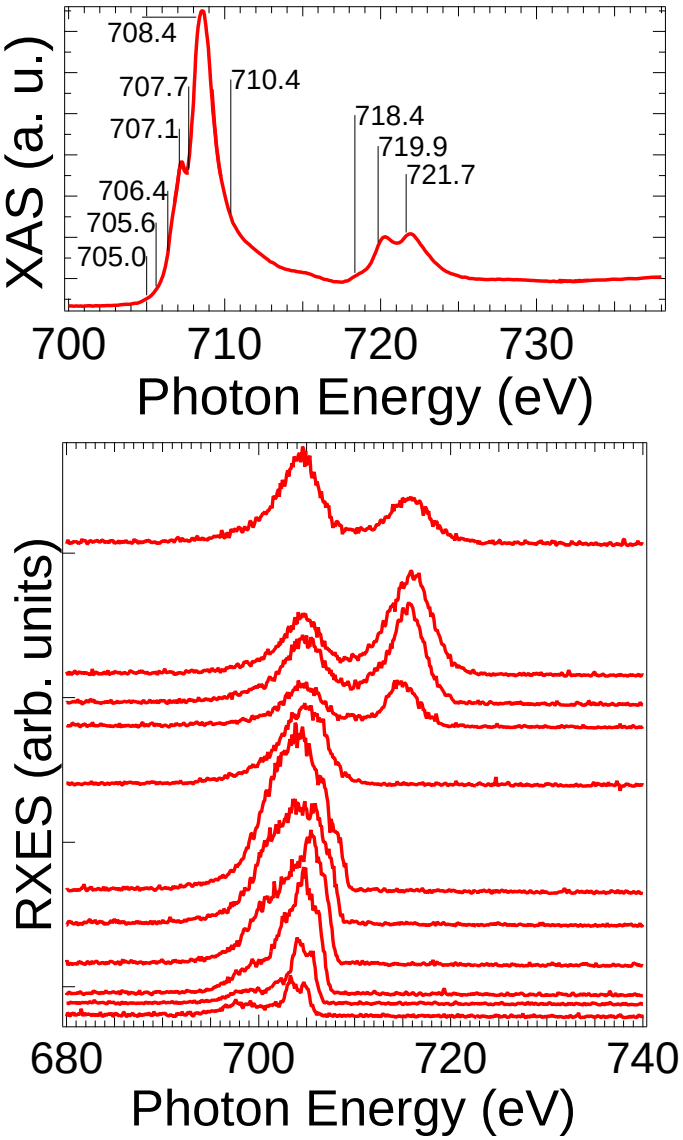

Figure 5.4: RXES at the Fe L-edge (lower panel) of $LuFe_2O_4$ excited with the energies indicated in the corresponding Fe L-edge XAS (upper panel).

In the lower panel of figure 5.4 the Fe $3d \rightarrow 2p$ RXES is presented. The corresponding excitation energies are indicated in the XA spectrum of the Fe L–edge which is plotted in the upper panel of figure 5.4. The RXE spectra excited at the onset of the Fe L_3–edge XAS (705.0 eV and 705.6 eV) comprise the elastic peak and an energy loss peak in 1.5 eV distance. The inelastic structure from 700 eV to 708 eV is growing with the excitation energy while the energy loss peak is shifted with the elastic peak. The loss peak and the elastic peak disappear for excitations above 710 eV. For excitations at the Fe L_2–edge ($\approx$720 eV) the second inelastic structure appears at around 715 eV. The elastic features of the RXE spectra are marked

in figure 5.5 on an energy loss scale. The elastic peak at 0 eV is clearly visible for lower excitation energies (705.0, 705.6 and 706.4 eV). The loss feature at 1.5 eV was mentioned above. Another small loss feature is located at 4 eV. The 1.5 eV feature

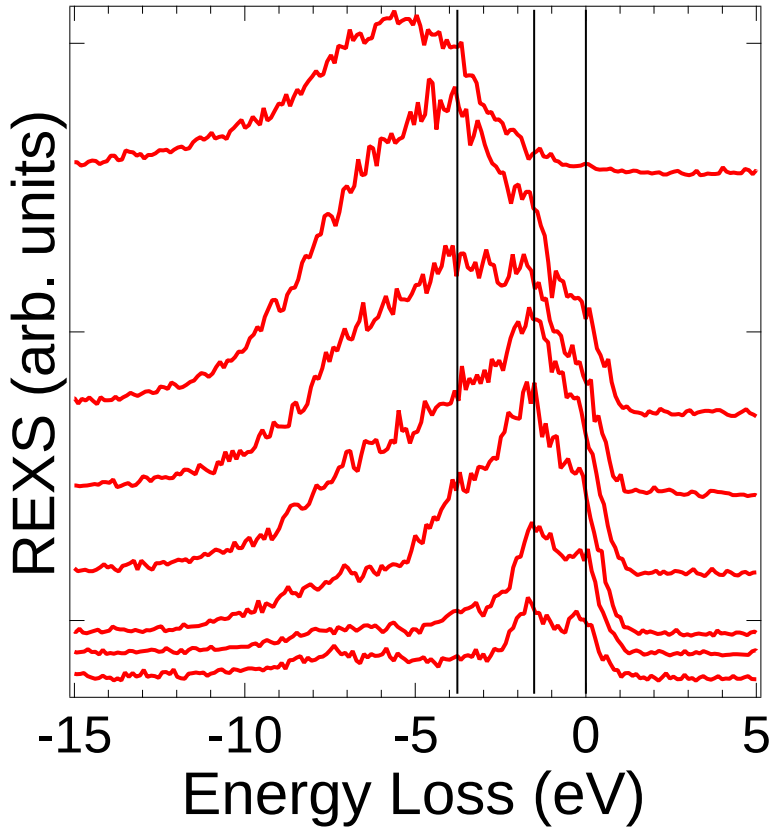

Figure 5.5: RXES at the O K-edge of $LuFe_2O_4$ on an energy loss scale. Excitation energies are indicated the corresponding XAS in the upper panel of figure 5.4.

might be interpreted as excitation from the highest occupied states of divalent Fe ions to the lowest unoccupied states of trivalent iron, which are in both cases down spin $3d_{xy}$ and $3d_{x^2-y^2}$ states. This electron hopping is the reason for the ferroelectric properties (Ikeda *et al.*, 2007). The 4 eV feature might be interpreted as an intra atomic excitation of the spin down electrons at the divalent iron sites from the highest unoccupied Fe 3d states to the lowest unoccupied Fe 3d states. This suggestions arise from band structure calculations from Xiang and Whangbo (2007) where comparable energy differences can be found around the Fermi level. It should be noted that these ground state energies do not correspond to excitation and can just give a hint for possible explanations.

The RXE O 2p →O 1s spectra are presented in the lower panel of figure 5.6. The excitation energies for the RXES are marked in the XA spectra in the upper panel of figure 5.6. The resonant excitation of the XE spectra comprises no elastic features. The inelastic peak is located at 523 eV.

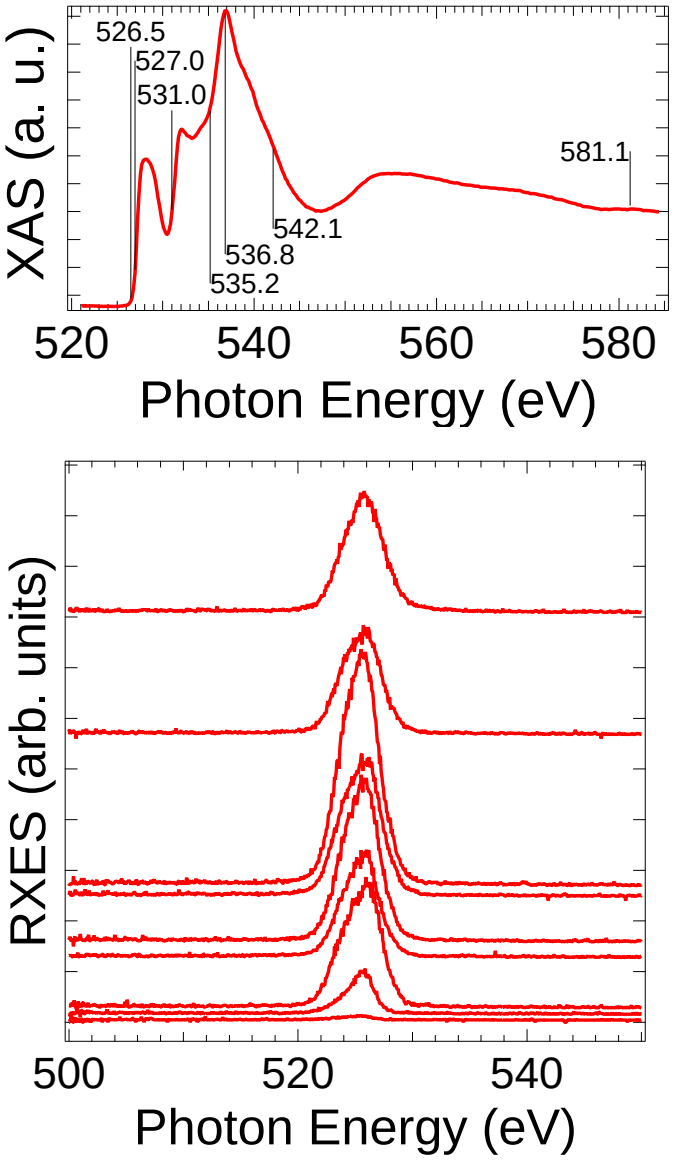

Figure 5.6: RXES at the O K-edge (lower panel) of $LuFe_2O_4$ excited with the energies indicated in the corresponding O K-edge XAS (upper panel).

5.4 Discussion

5.4.1 Occupied States by XPS, XES and Calculations

The electronic structure of occupied states was investigated by x-ray photoelectron spectroscopy (XPS) of the valence band and x-ray emission spectroscopy (XES) from Fe $3d \rightarrow$ Fe $2p$ and O $2p \rightarrow$ O $1s$. The results are presented in figure 5.7 in comparison with band structure calculations made by A. Postnikov of the Université Paul Verlaine in Metz within the same approach as outlined in the previous Chapter 4; the WIEN2k code (Blaha *et al.*, 2001) and GGA+U calculation. For the latter the U value of 0.7 Ry≈9.5 eV for the Lu $4f$ states and 0.3 Ry≈4.1 eV for the Fe $3d$ states gave the best agreement with the experiment.

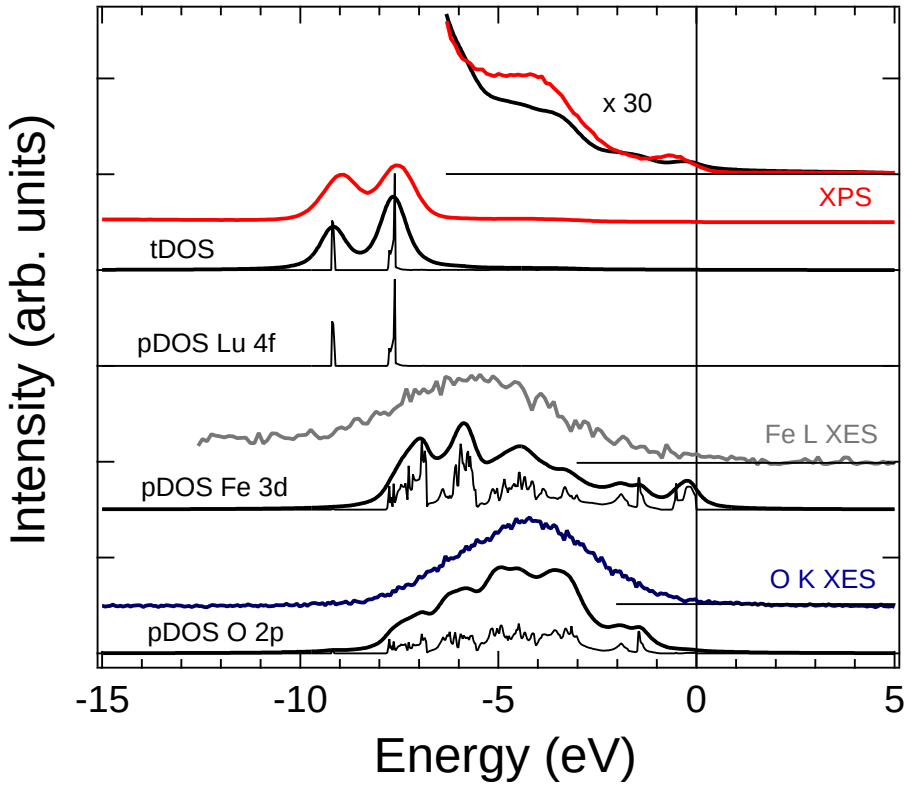

Figure 5.7: Partial and total occupied DOS of $LuFe_2O_4$ calculated by LDA+U calculations in comparison with the XPS valenceband and XES measurements of the Fe L-edge and the O K-edge. In the top the calculated tDOS and the XPS is enlarged for comparison of the small states close to the Fermi level.

In the XP spectrum two peaks of the Lu $4f$ multiplet are located at -7.5 eV and -9 eV. The structure from -3 eV to -6 eV are distributed to O $2p$ states hybridized with Fe $3d$ states in comparison with the XE spectra of the Fe L–edge and the O K–edge. The small states close to the Fermi level (0 eV to -1 eV) can be interpreted as highest occupied Fe $3d$ (d_{xy}, $d_{x^2-y^2}$) spin down states of the divalent sites in comparison with band structure calculations of Xiang and Whangbo (2007).

The band structure calculations presented in figure 5.7 are in excellent agreement with the XES and XPS measurements. The states close to the Fermi level in the XPS valence band can be identified as highest occupied Fe 3*d* states as stated above. Remarkable is the agreement between the XPS and the calculation in the range from −5 eV to Fermi level as can be seen in the thirty times enlarged spectra in the top of figure 5.7. The strong hybridization between Fe 3*d* and O 2*p* becomes clear if one compares the peak structure of the calculated DOS of these states where the most intense Fe 3*d* states are located at −6 eV and −7 eV and the most intense O 2*p* states are located at −3.5 eV and −4.5 eV. Here it is very clear that the states at higher binding energy (∼ −6 eV) have *d* character and the states at ∼ −4 eV have *p* character as found by Winiarski *et al.* (1994) for $KTaO_3$ and $KNbO_3$. In comparison with the calculations from Xiang *et al.* the Fe 3*d* spin–up states can be identified to the d_{z^2} at −7 eV while $d_{xy+dx^2-y^2}$ orbitals contribute to the −7 eV and −6 eV peak and the d_{xy+dxz} orbitals are contributing mainly to the −6 eV peak and just a small part of the −7 eV peak is attributed to this orbital. In the calculations from literature the hybridization between O 2*p* and Fe 3*d* is weaker than in the approach of the present work. The small density at −1.5 eV appears in the Fe 3*d* and the O 2*p* calculation in similar intensity. It should be noted that the 3*d* orbitals in the distorted crystal field cannot be exactly described by the common notation, e.g. d_{z^2} because different distortions lead to different combinations of these basic orbitals as found by Khomskii and Kugel (2003) which was mentioned in section 3.5.

5.4.2 Unoccupied States by XAS and Calculations

The unoccupied states of $LuFe_2O_4$ were investigated by XAS at the Fe *L*–edge and the O *K*–edge. The experiment are compared with LDA+U = 0.7 Ry band structure calculations in figure 5.8. The calculations are convoluted with 0.4 eV gaussian for experimental broadening. The calculated unoccupied Fe 3*d* states take place from 0 eV to 3 eV which is in agreement with the states measured by XAS. The prepeak in the XAS corresponds to the divalent Fe ions and its position is influenced by the small chemical shift in the Fe 2*p* core level. This shift is only present in the absorption measurement because the dipole transition from the core level to the conduction band is not taken into account for band structure calculations. In section 5.4.3 multiplet calculations are presented for XMCD spectra which take into account the transition of the XAS process and show a very good agreement with the experiment.

The unoccupied states of the O 2*p* states are located over a wide range from 0 eV to 16 eV with three local maxima at 1 eV, 5 eV and 10 eV. This structure is relatively good reproduced by the calculations. The second peak at 5 eV is calculated too close to the Fermi level, but the general structure is very well calculated. The first peak close to the Fermi level is at the same position where the unoccupied Fe 3*d* states are located. This indicates the strong hybridization between Fe 3*d* and O 2*p* which is also present in the occupied states discussed in section 5.4.1.

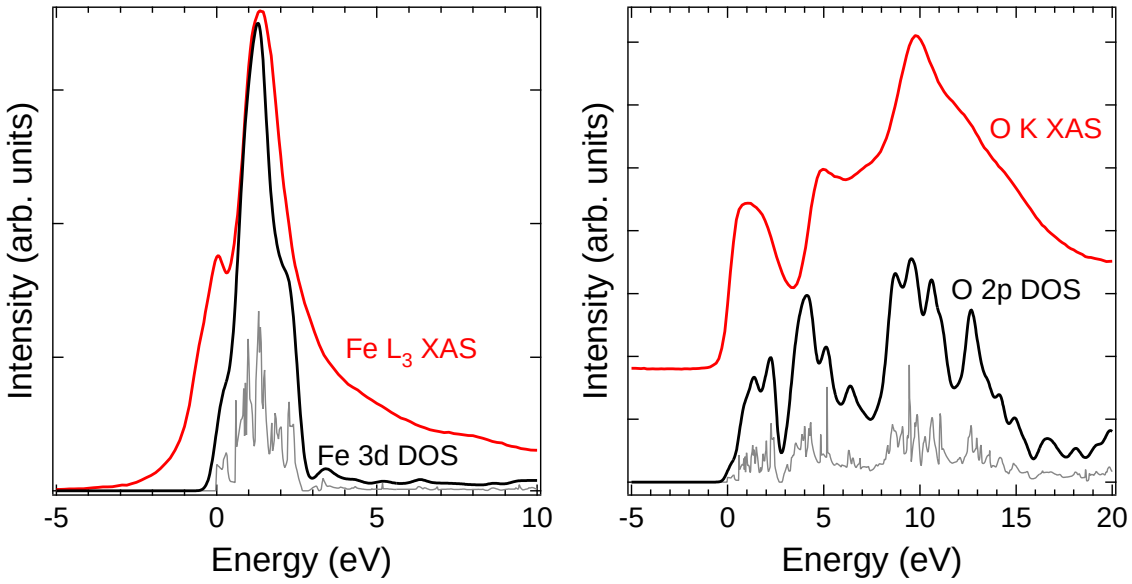

Figure 5.8: Fe L-edge (left panel) and O K-edge (right panel) XAS of $LuFe_2O_4$ in comparison with band structure calculations with 0.4 eV gaussian broadening.

5.4.3 Magnetic Structure by XMCD

The magnetic structure of $LuFe_2O_4$ can be investigated by means of x-ray magnetic circular dichroism (XMCD). As described in section 2.3.2, the XMCD gives information about element specific spin and orbital magnetic moments. One can also distinguish between different valence states. Therefore this technique is a very powerful tool to investigate the magnetic structure of $LuFe_2O_4$.

For a better understanding of the experimental XMCD spectra of the Fe L–edge multiplet calculations were performed. The crystal symmetry c_{3i} of $LuFe_2O_4$ is included in the calculations. To find the best parameters to describe the bipyramidal trigonal crystal field the parameters were tested with calculations for Ti^{3+}. In this configuration just one $3d$ electron is present and in the ground state the crystal field splitting of the $3d$ states is directly visible. The crystal field parameters for the multiplet calculations are implemented in the .rac file which is shown in figure 5.10. With this parameters the $3d$ states split as depicted in figure 5.9. This splitting is typical for a trigonal bipyramidal crystal field. In comparison with band structure calculations from Xiang and Whangbo (2007) the energetic lowest states are the d_{xy} and $d_{x^2-y^2}$, at somewhat higher energy the d_{xz} and d_{yz} are located and the energetic highest state is d_{z^2}.

In figure 5.11 the XMCD spectra of the Fe L–edge, measured in TEY, is presented in the upper part of the graph and the multiplet calculations in c_{3i} symmetry are plotted in the lower part of the graph for comparison. The Fe^{2+} and Fe^{3+} peak of the L_3–edge are located at 708.0 eV and 709.5 eV, respectively. The Fe^{3+} contribution is higher than 50% which is in agreement with the XAS results of figure 5.3 in section 5.2, where the Fe^{3+} contribution is up to 80%. The best agreement between multiplet calculations and experiment is achieved with 50% antiferro magnetic

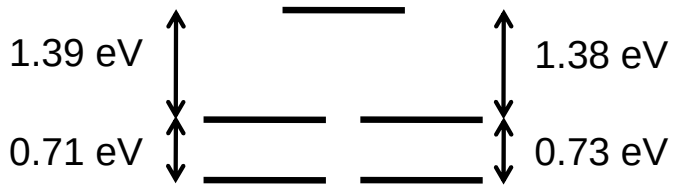

Figure 5.9: Ground state of $3d$ states in Ti^{3+} calculated with TT multiplet. The parameters for the calculations are shown in the .rac file figure 5.10.

Fe^{3+} and 50% magnetic mixed–valent bulk, resulting in an overall Fe^{3+} contribution of 75%. The Fe L_2–edge peaks are located at 721 eV and 723 eV with a shoulder at 720 eV. The experimental dichroic signal at the L_2–edge is very small, but the dichroism in the calculated L_2–edge agrees with the experiment. The L_3–edge shows a clear dichroism at the Fe^{2+} peak and a smaller dichroism at the Fe^{3+} peak which is inverted. This is a clear indication of a majority spin at the Fe^{2+} sites, while 1/3 of the Fe^{3+} spin is in majority and 2/3 is in minority. This configuration is also used for the multiplet calculations and gives a perfect agreement with the experiment besides the shoulder at 707 eV which is overestimated by the calculation. Such a configuration was found before in LFO by Mössbauer and neutron diffraction (Sugihara *et al.*, 1978; Tanaka *et al.*, 1989). This configuration is in contradiction to the magnetization found by Iida *et al.* (1993) who measured 2.8 μ_B/f.u.. The mentioned spin configuration results in a lower magnetization $4\mu_B + 2/3 * 5\mu_B - 1/3 * 5\mu_B = 2.33\mu_B$/f.u.. This discrepancy can be explained by the magnetic moment determined by the sum rules from the XMCD data as described in section 2.3.2. The antiferromagnetic Fe at the surface is taken into account in the analysis. The factors found by Teramura *et al.* (1996) were also taken into account (Fe^{2+}:0.875, Fe^{3+}:0.685). In table 5.1 the resulting moments are presented. The relatively high orbital moment of 0.76 μ_B/f.u.

Table 5.1: Magnetic spin and orbital moment at the Fe sites determined by the sum rules from XMCD in comparison with moment determined from multiplet calculations and expected values.

	XMCD	multiplet calculation		expected	
	$LuFe_2O_4$	Fe^{2+}	Fe^{3+}	Fe^{2+}	Fe^{3+}
M_{spin}	1.41 μ_B/f.u.	2.490 μ_B	3.299 μ_B	4.0 μ_B	5.0 μ_B
M_{orb}	0.76 μ_B/f.u.	1.494 μ_B	0.009 μ_B	$\pm$2.0 μ_B	0.0 μ_B

can explain the discrepancy between the moment resulting from the spin configuration and the total magnetic moment measured by magnetometry. The spin configuration results in a spin moment of m_{spin} =2.33 μ_B/f.u. and the maximal orbital moment for Fe^{2+} in an trigonal bipyramidal crystal field and in high spin state is $m_{orb} = \pm 2$ μ_B/f.u. for the occupation of d_{xy} or $d_{x^2-y^2}$, while the Fe^{3+} in high spin state has no orbital moment due to completely filled spin up states and completely empty down spin states. This results in a maximal total magnetic moment of M =2.33 μ_B/f.u.+2 μ_B/f.u.=4.33 μ_B/f.u.. In this model the magnetization of the spin moment is ∼60.5 % at a temperature of $T = (260 - 280)$ K and magnetic field

```
% vertical 1 1
butler O3
to    Oh
to    D3d
to    C3i
endchain
actor   0+ HAMILTONIAN ground  PRINTEIG
 OPER HAMILTONIAN
   BRANCH 0+ > 0 0+ > 0+  > 0+  1.0
 OPER SHELL2
   BRANCH 4+ > 0 0+ > 0+  > 0+  -3.834
   BRANCH 4+ > 0 ^1+ > 0+  > 0+ -2.240
   BRANCH 2+ > 0 ^1+ > 0+  > 0+ 2.0
 OPER SPIN2

   BRANCH 1+ > 0 1+ > ^0+   > 0+   0.001
actor   0+ HAMILTONIAN excite  PRINTEIG
 OPER HAMILTONIAN
   BRANCH 0+ > 0 0+ > 0+  > 0+  1.0
 OPER SHELL2
   BRANCH 4+ > 0 0+ > 0+  > 0+  -3.834
   BRANCH 4+ > 0 ^1+ > 0+ > 0+  -2.240
   BRANCH 2+ > 0 ^1+ > 0+ > 0+  2.0
 OPER SPIN2

   BRANCH 1+ > 0 1+ > ^0+   > 0+   0.001
actor   1- left        transi PRINTTRANS
  oper MULTIPOLE
    branch  1- > 0 1- >  1- > 1- 1.000
actor   -1- right        transi PRINTTRANS
  oper MULTIPOLE
    branch  1- > 0 1- >  1- > -1- 1.000
actor   0- parallel    transi PRINTTRANS
  oper MULTIPOLE
    branch  1- > 0 1- > ^0- > 0- 1.000
RUN
```

Figure 5.10: Multiplet calculation parameters for bipyramidal trigonal crystal field for Ti^{3+}. The resulting ground state splitting of $3d$ states is depicted in figure 5.9.

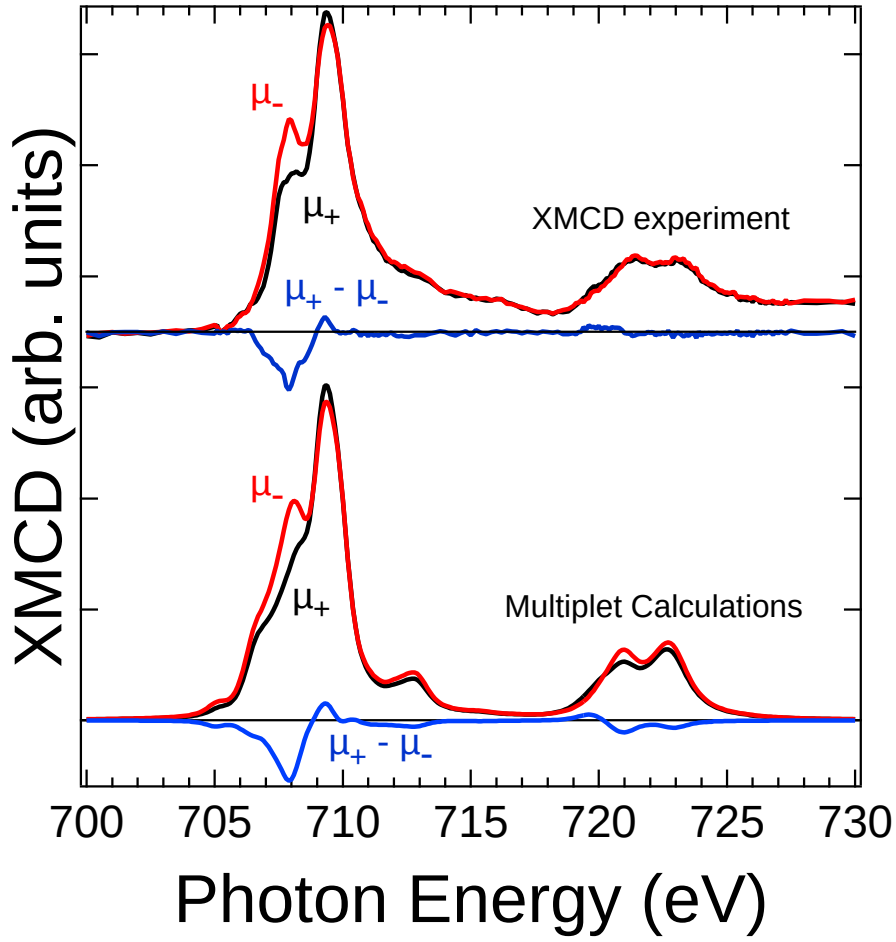

Figure 5.11: XMCD spectra in TEY (top) in comparison with multiplet calculations (bottom) of $LuFe_2O_4$ at the Fe L-edge.

of $B = 6$ T and the orbital moment is quenched from 2 μ_B/f.u. to 0.76 μ_B/f.u.. The high orbital moment can be also determined from the multiplet calculation of Fe^{2+}. The experimental orbital moment is partly quenched, but in many bulk materials the orbital moment is completely quenched. The high orbital moment agrees also with the very large hysteresis in the magnetization measurements of Iida *et al.* (1993) where the spin flips from one orientation to the other at a magnetic field of ∼11 T pointing antiparallel to the magnetization. The orbital moment is the reason for the spin–lattice interaction and the magnetic easy axis is set by the orbital moment which is fixed in the lattice by the electron configuration.

5.5 Conclusions

In conclusion the valence state of Fe ions in $LuFe_2O_4$ was determined to 50% 2+ and 50% 3+ by XPS of Fe $2p$ and $3s$ levels. In XAS experiments in TEY mode a higher Fe^{3+} contribution was found at the not cleaved surface. The more bulk

sensitive TFY mode showed that the bulk of the sample has the expected 50%–50% configuration. In the REXS of the O K–edge two energy loss features were found at 1.5 eV and 4 eV. The 1.5 eV feature might be due to electron hopping and the 4 eV feature might be due to an intraatomic excitation. The comparison of the occupied states measured by XPS and XES with LDA+U calculations showed the following electronic structure. Lu $4f$ states are located at -7.5 eV and -9 eV. Fe $3d$ states are strongly hybridized with O $2p$ states from -1 eV to -8 eV while at higher binding energy (~ -6 eV) more d character was present and the p character was found at lower binding energies (~ -4 eV). Very small states at the Fermi level in XPS and XES could be identified as highest occupied Fe^{2+} states which corresponds to the d_{xy} and $d_{x^2-y^2}$ spin down states. The unoccupied states measured by XAS at the Fe L–edge and the O K–edge could be calculated by the LDA+U calculation in good agreement. The magnetic structure was investigated by XMCD and showed that the Fe^{2+} ions contribute to the majority spin moment and the Fe^{3+} ions contribute with 2/3 to minority and 1/3 to majority spin moment resulting in a total spin magnetic moment of 2.33 μ_B/f.u.. This configuration was found before with Mössbauer and neutron diffration, but a discrepancy to magnetic measurement finding a total magnetic moment of $\sim$2.8 μ_B/f.u. could not be explained. The orbital magnetic moment of 0.74 μ_B/f.u. found by XMCD could explain this discrepancy and could also explain the big hysteresis from -11 T to 11 T in high field magnetic measurements at 4.2 K because the spin moment is coupled via the orbital moment to the crystal lattice and so a not quenched orbital moment can lead to a strong easy axis of the magnetization.

Summary and Outlook

In this work the electronic and magnetic structure of the colossal magneto resistance material $La_{1-x}Sr_xMnO_3$, the high–k and strain tailoring compounds $REScO_3$ (Sm, Gd, Dy) and the multiferroic $LuFe_2O_4$ was investigated by means of x-ray spectroscopic techniques.

In Chapter 3, SQUID measurements of $La_{1-x}Sr_xMnO_3$ (x = 0.125, 0.17, 0.36) were compared with XMCD results. The very good agreement of these two experiments proofs the applicability of the correction factor for the spin magnetic moment and the importance of charge transfer. The multiplet calculations gave the best agreement with the XMCD spectra with charge transfer of 47.7% for Mn^{4+} and 29.0% for Mn^{3+}. For the samples with $x = 0.125$ and $x = 0.17$, a canted spin was confirmed by magnetometry and XMCD results. The perfect agreement of the magnetic moment measured by SQUID and that determined from XMCD for the single crystalline samples proofs that the magnetic moment is completely localized at the Mn ions at the temperature of 80 K for $x = 0.17$ and 0.36 and in the temperature range from 80 K to 300 K for $x = 0.125$. In comparison with the literature it was assumed that the applied magnetic field leads the a localization of e_g electrons. This influence can explain the decreasing resistance with the applied magnetic, field because the localization of the e_g electrons leads to better hole conductivity. For $x = 0.125$ the orbital magnetic moment determined from XMCD corresponds to the structural change which occurs in the temperature range from 145 K to 188 K, whereby a change of sign of the orbital moment corresponds to the occupation of different orbitals in different structural phases. This is corresponding to a change of sign of the orthorhombic strain in the $b - c$ plane at the transition temperatures. In the temperature range from 188 K to 275 K where a coherent Jahn–Teller distortion takes place, the orbital moment is reduced which is explained by different orientated orbitals. Additionally the measured orbital moments correspond to anomalies in magnetization versus temperature curves. Furthermore a spinflip below the charge ordering temperature is confirmed by magnetization versus temperature curves of $La_{0.875}Sr_{0.125}MnO_3$.

The magnetic and electronic structure of the rare earth scandates ($SmScO_3$, $GdScO_3$ and $DyScO_3$) were presented in Chapter 4. The magnetic measurements reveal antiferromagnetic coupling at low temperatures in agreement with neutron diffraction data of the Dy compound. A strong hybridization between Sc 3d and O 2p states was found in the photoemission, emission and absorption measurements in agreement with band structure calculations. There are indications for a more complex hybridization between Sc 3d, O 2p and RE 5d states. With x-ray absorption and emission spectroscopy at the O K-edge in comparison with band structure calculations of the unoccupied oxygen states, the band gaps of $RESCO_3$ were determined

and it was found that these values are corresponding to the Sc–O mean distances.

In Chapter 5 the electronic and magnetic structure of $LuFe_2O_4$ was presented. The valence state of Fe ions was determined to 50% 2+ and 50% 3+ by XPS of Fe $2p$ and $3s$ levels. The complete electronic structure of the occupied and unoccupied states was investigated by x-ray spectroscopic techniques in agreement with band structure calculations. Small states close to the Fermi level could be identified as highest occupied Fe^{2+} states. The magnetic structure was investigated by XMCD and showed that the Fe^{2+} ions contribute to the majority spin moment, whereas the Fe^{3+} ions contribute with 2/3 to minority and 1/3 to majority spin moment resulting in a total spin magnetic moment of 2.33 μ_B/f.u.. The orbital magnetic moment of 0.74 μ_B/f.u. found by XMCD could explain the discrepancy to magnetic measurements ($\sim$2.8 μ_B/f.u.) and could also explain the big hysteresis from -11 T to 11 T in high field magnetic measurement at 4.2 K.

Now a short outlook is given for further investigation of the investigated compounds.

For $La_{1-x}Sr_xMnO_3$ it would be very interesting to get a more detailed picture of temperature and magnetic field dependence of the orbital moment. It might be possible to find a direct correspondence between the orbital moment and the orbital ordering which is essential for the CMR compound family. Another possible approach to learn more about the orbital ordering would be the x-ray magnetic linear dichroism which can be measured in different geometric orientations.

For the rare earth scandates some compounds with other rare earth ions could be investigated to get a complete picture of the band gap behaviour of this family.

The magnetic structure of the multiferroic $LuFe_2O_4$ should be investigated by XMCD at different temperatures to get more information about the orbital moment which seems to play an important role for the magnetic behaviour of this compound. It should be noted that in the total electron yield, some problems occurred at temperatures below T_C. One possibility is to measure the XMCD in fluorescence yield. Furthermore the character of the metallic states close to the Fermi level could be investigated by angle–resolved ultraviolet photoemission spectroscopy.

Acknowledgement

It is gratefully acknowledged that this work was facilitated by the *Graduate College 695: Nonlinearities of Optical Materials* which is financed by the *Deutsche Forschungsgemeinschaft* and the *Federal State of Niedersachsen*. Furthermore I want to acknowledge the financial support by the department of physics of the university of Osnabrück.

I want to thank apl. Prof. Prof. h.c. Dr. Dr. h.c. Manfred Neumann for enabling this work in the workgroup *Elektronenspektroskopie* at the university of Osnabrück. His scientific intuition and competence was a great gift for my work. Apart from that, he excellently supports the social activities of our workgroup.

Now I want to thank collaborating scientists for the scientific support and the friendly companionship. Firstly I want mention Dr. Karsten Küpper, who has supervised already my diploma thesis and has also been a great support for this work. Next I want to thank Prof. Dr. Andrei Postnikov for the very good cooperation and the painstaking correction of publications and this work, especially.

My workgroup was during the years always a very friendly mixture of nice people. The homelike atmosphere is due to my good friends Manuel Prinz and Christian Taubitz, who were always helping hands in private and scientific questions. Especially in the last year, a real gift were our diploma students Christine, Anna and Miriam. They have my sympathy and friendship. I want to thank Werner Dudas for technical support and the private evenings during the last years. Furthermore I have to acknowledge the electrical and mechanical workshops of the department, as well as the crystal growth facility, that has prepared many samples for my work. The whole Department of Physics of the University of Osnabrück is acknowledged for nice working atmosphere. The secretaries, especially our secretary Marion von Landsberg, were always very kind and helpful.

A really hearty thank is for my family, who have supported my whole education and life in any situation. Mum and Dad, Marc and Saskia, thank you! I want to mention also the Holterhues family, who are extremely friendly and helpful. One cannot find more hospitability anywhere.

At the end I want to thank my only one, Julia Holterhues, for the best years of my life, your patience, your kindness and your love. Kisses!

Danksagung

Diese Arbeit wurde durch das *Graduiertenkolleg 695: Nichlinearitäten optischer Materialien* ermöglicht, das finanziert wird von der *Deutschen Forschungsgemeinschaft* und dem *Bundesland Niedersachsen*. Ich möchte mich darüberhinaus für die finanzielle Unterstützung des Fachbereichs Physik der Universität Osnabrück bedanken.

Mein Dank gilt apl. Prof. Prof. h.c. Dr. Dr. h.c. Manfred Neumann für das Ermöglichen dieser Arbeit in der Arbeitsgruppe *Elektronenspektroskopie* der Universität Osnabrück. Seine wissenschaftliche Intuition und Kompetenz waren ein großes Geschenk für meine Arbeit. Abgesehen davon unterstützt er in exzellenter Weise die sozialen Aktivitäten unserer Arbeitsgruppe.

Nun will ich Kooperationspartnern für wissenschaftliche Unterstützung und freundliche Begleitung danken. Zuerst möchte ich Dr. Karsten Küpper nennen, der schon meine Diplomarbeit betreut hat und auch eine große Unterstützung bei dieser Arbeit war. Als nächstes möchte ich Prof. Dr. Andrei Postnikov für die sehr gute Zusammenarbeit und für die ausführlichen Korrekturen von Veröffentlichungen und insbesondere von dieser Arbeit danken.

In den letzten Jahren war meine Arbeitsgruppe immer eine freundliche Mischung aus netten Leuten. Die heimische Atmosphäre entstand durch meine guten Freunde Manuel Prinz und Christian Taubitz, die mir immer in privaten und wissenschaftlichen Fragen geholfen haben. In besonderer Weise waren im letzten Jahr unsere Diplomandinnen Christine, Anna und Miriam ein wahres Geschenk. Ihnen gilt meine Sympathie und Freundschaft. Ich möchte Werner Dudas für seine technische Unterstützung danken wie auch für private Abende in den letzten Jahren. Weiterhin möchte ich mich bei der Elektronikwerkstatt und der feinmechanischen Werkstatt bedanken, sowie der Kristallzucht, in der viele Proben für mich präpariert wurden. Bedanken möchte ich mich bei dem gesamten Fachbereich Physik der Universität Osnabrück für die nette Atmosphäre. Die Sekretärinnen, besonders unsere Sekretärin Marion von Landsberg, waren immer nett und hilfsbereit.

Ein sehr herzlicher Dank gilt meiner Familie, die meine komplette Ausbildung und mein ganzes Leben in jeder Situation unterstützt hat. Mama und Papa, Marc und Saskia, vielen Dank! Ich möchte auch der Familie Holterhues danken, die sehr freundlich und hilfsbereit ist. Nirgendwo kann man mehr Gastfreundschaft finden.

Am Ende bedanke ich mich bei meiner Liebsten, Julia Holterhues, für die besten Jahre meines Lebens, Deine Geduld, Deine Liebenswürdigkeit und Deine Liebe. Kuss!

Bibliography

Abe, K., N. Yanase, K. Sano, M. Izuha *et al.* (1998). Modification of ferroelectricity in heteroepitaxial (Ba,Sr)TiO_3 films for non-volatile memory applications. *Integr. Ferroelectr.* **21**, 197.

Afanas'ev, V. V., A. Stesmans, C. Zhao, M. Caymax *et al.* (2004). Band alignment between (100)Si and complex rare earth/transition metal oxides. *Appl. Phys. Lett* **85**, 5917.

Alers, G. B., D. J. Werder, Y. Chabal, H. C. Lu *et al.* (1998). Intermixing at the tantalum oxide/silicon interface in gate dielectric structures. *Appl. Phys. Lett.* **73**, 1517.

Andersen, P. W. (1961). Localized Magnetic states in Metals. *Phys. Rev.* **124**, 41.

Anderson, P. W. (1950). Antiferromagnetism. Theory of Superexchange Interaction. *Phys. Rev.* **79**, 350.

Anisimov, V. I., F. Arysetiawan and A. I. Lichtenstein (1997). First-principles calculations of the electronic structure and spectra of strongly correlated systems: the LDA + U method. *J. Phys. Cond. Mat.* **9**(4), 767.

Anisimov, V. I. and O. Gunnarsson (1991). Density-functional calculation of effective Coulomb interactions in metals. *Phys. Rev. B* **43**, 7570.

Anisimov, V. I., M. A. Korotin, J. Zaanen and O. K. Andersen (1992). Spin bags, polarons, and impurity potentials in $La_{2-x}Sr_xCuO_4$ from first principles. *Phys. Rev. Lett.* **68**, 345.

Anisimov, V. I., J. Zaanen and O. K. Andersen (1991). Band theory and Mott insulators: Hubbard U instead of Stoner I. *Phys. Rev. B* **44**, 943.

Arenholz, E. and S. O. Prestemon (2005). Design and performance of an eight-pole resistive magnet for soft x-ray magnetic dichroism measurements. *Rev. Sci. Instrum.* **76**, 083908.

Arenholz, E., G. van der Laan, R. V. Chopdekar and Y. Suzuki (2007). Angle-Dependent Ni^{2+} X-Ray Magnetic linear Dichroism: Interfacial Coupling Revisited. *Phys. Rev. Lett.* **98**, 197201.

Asamitsu, A., Y. Moritomo, Y. Tomioka, T. Arima *et al.* (1995). A structural phase transition induced by an external magnetic field. *Nature* **373**, 407.

Attwood, D. (1999). *Soft X-rays and Extreme Ultraviolet Radiation*. Cambridge University Press, Cambridge.

Auger, P. (1925). Sur l'Effect Photoélectrique Composé. *Le Journal de Physique et le Radium* **6**, 205.

Badie, J. M. (1978). Phases and transitions at high temperature in the system Sc_2O_3-Ln_2O_3 (Ln = lanthanide and yttrium). *Rev. Int. Hautes Temp. Refract.* **15**, 183.

Bagus, P. S., A. J. Freeman and F. Sasaki (1973). Prediction of New Multiplet Structure in Photoemission Experiments. *Phys. Rev. Lett.* **30**, 850.

Banach, G. and W. M. Temmerman (2004). Delocalization and charge disproportionation in $La_{(1-x)}Sr_xMnO_3$. *Phys. Rev. B* **69**, 054427.

Bang, B. K., T. Kouh and C. S. Kim (2008). Magnetic property and charge ordering effect in polycrystalline $LuFe_2O_4$. *J. Appl. Phys.* **103**, 07E307.

Beach, R. S., J. A. Borchers, A. Matheny, R. W. Erwin *et al.* (1993). Enhanced Curie temperatures and magnetoelastic domains in Dy/Lu superlattices and films. *Phys. Rev. Lett.* **70**, 3502.

Becquerel, J. (1929). Einleitung in eine Theorie der magneto-optischen Erscheinungen in Kristallen. *Z. Physik* **58**, 205.

Berglund, C. N. and W. E. Spicer (1964). Photoemission Studies of Copper and Silver: Theory. *Physical Review* **136**, A1030.

Bertaut, E. F. (1968). Representation analysis of magnetic structures. *Acta. Cryst.* **A24**, 217.

Bethe, H. (1929). Termaufspaltung in Kristallen. *Ann. Physik* **395**, 133.

Bethe, H. (1930). Zur Theorie des Zeemaneffektes an den Salzen der seltenen Erden. *Z. Physik A* **60**, 218.

Biegalski, M. D., J. H. Haeni, S. Troiler-Mckinstry, D. G. Schlom *et al.* (2005). Thermal expansion of the new perovskite substrates $DyScO_3$ and $GdScO_3$. *J. Mater. Res.* **20**, 952.

Bilc, D. I., R. Orlando, R. Shaltaf, G.-M. Rignanese *et al.* (2008). Hybrid exchange-correlation functional for accurate prediction of the electronic and structural properties of ferroelectric oxides. *Phys. Rev. B* **77**, 165107.

Binek, C. and B. Doudin (2005). Magnetoelectronics with magnetoelectrics. *J. Phys. Cond. Mat.* **17**, L39.

Blaha, P., K. Schwarz, G. K. H. Madsen, D. Kvasnicka *et al.* (2001). *An Augmented Plane Wave + Local Orbitals Program for Calculating CrystalProperties*. Karlheinz Schwarz, Techn. Universität Wien, Austria.

Bonrath, H., K. H. Hellwege, K. Nicolay and G. Weber (1966). Antiferromagnetische Umwandlung von Dy_2O_3, Er_2O_3 und Yb_2O_3 im Temperaturbereich von 1,1 bis 4,2 K . *Z. Physik B Condensed Matter* **4**, 382.

Booth, C. H., F. Bridges, G. H. Kwei, J. M. Lawrence *et al.* (1998). Lattice Effects in LCMO: distortions, charge distribution and magnetism. *Phys. Rev. B* **57**, 10440.

Borstel, G. (1985). Theoretical aspects of photoemission. *Applied Physics A* **38**, 193.

Bowen, M., M. Bibes, A. Barthélémy, J.-P. Contour *et al.* (2003). Nearly total spin polarization in $La_{2/3}Sr_{1/3}MnO_3$ from tunneling experiments. *Appl. Phys. Lett.* **82**, 233.

Bozovic, I., G. Logvenov, I. Belca, B. Narimbetov *et al.* (2002). Epitaxial strain and superconductivity in $La_{2-x}Sr_xCuO_4$ thin films. *Phys. Rev. Lett.* **89**, 107001.

Brundle, C. R. and A. D. Baker (1979). *Electron Spectroscopy: Theory, Techniques and Applications*. John Willey & Sons, Bristol.

Bukowski, Z., J. Dabrowski, J. Mais, P. W. Klamut *et al.* (2000). Effect of oxygen stoichiometry on properties of $La_{0.815}Sr_{0.185}MnO_{3+d}$. *J. Appl. Phys.* **87**, 5031.

Canedy, C. L., H. Li, S. P. Alpay, L. A. Salamanca-Riba *et al.* (2000). Dielectric properties in heteroepitaxial $Ba_{0.6}Sr_{0.4}TiO_3$ thin films: Effect of internal stresses and dislocation-type defects. *Appl. Phys. Lett.* **77**, 1695.

Carra, P., B. T. Thole, M. Altarelli and X. Wang (1993). X-ray circular dichroism and local magnetic fields. *Phys. Rev. Lett.* **70**, 694.

Catalan, G., A. Janssens, G. Rispens, S. Csiszar *et al.* (2006). Polar Domains in Lead Titanate Films under Tensile Strain. *Phys. Rev. Lett.* **96**, 127602.

Chaneliere, C., J. L. Autran, R. A. B. Devine and B. Balland (1998). Tantalum pentoxide (Ta_2O_5) thin films for advanced dielectric applications. *Mater. Sci. Eng. R.* **22**, 269.

Chastain, J. (1992). *Handbook of X-ray Photoelectron Spectroscopy*. Perkin Elmer Coorporation , Eden Prairie.

Chen, C. T., Y. U. Idzerda, H.-J. Lin, N. V. Smith *et al.* (1995). Experimental Confirmation of the X-Ray Magnetic Circular Dichroism Sum Rules for Iron and Cobalt. *Phys. Rev. Lett.* **75**, 152.

Choi, K. J., M. Biegalski, Y. L. Li, A. Sharan *et al.* (2004). Enhancement of Ferroelectricity in Strained $BaTiO_3$ Thin Films. *Science* **306**, 1005.

Chu, Y.-H., L. W. Martin, M. B. Holcomb, M. Gajek *et al.* (2008). Electric-field control of local ferromagnetism using a magnetoelectric multiferroic. *Nature materials* **7**, 478.

Chu, Y. H., Q. Zhan, L. W. Martin, M. P. Cruz *et al.* (2006). Nanoscale Domain Control in Multiferroic $BiFeO_3$ thin Films. *Adv. Mater.* **18**, 2307.

Chuang, Y. D., A. D. Gromko, D. S. Dessau, T. Kimura *et al.* (2001). Fermi surface nesting and nanoscale fluctuating charge/orbital ordering in colossal magnetoresistive oxides. *Science* **292**, 1509.

Cicerella, E. (2006). Dielectric functions and optical bandgaps of high-K dielectrics by far ultraviolet spectroscopic ellipsometry. Ph.D. thesis, OGI School of Science & Engeneering at Oregon Health & Science University.

Cohen, R. E. (1992). Origin of ferroelectricity in perovskite oxides. *Nature* **358**, 136.

Cohen, R. E. (2000). Theory of ferroelectrics: a vision for the next decade and beyond. *J. Phys. Chem. solids* **61**, 139.

Da Silva, J. L. F., M. V. Ganduglia-Pirovano, J. Sauer, V. Bayer *et al.* (2007). Hybrid functionals applied to rare-earth oxides: The example of ceria. *Phys. Rev B* **75**, 045121.

Dabrowski, B., X. Xiong, Z. Bukowski, R. Dybzinski *et al.* (1999). Structure-properties phase diagram for $La_{1-x}Sr_xMnO_3$ ($0.1 \leq x \leq 0.2$). *Phys. Rev. B* **60**, 7006.

Dawber, M., K. M. Rabe and J. F. Scott (2005). Physics of thin-film ferroelectric oxides. *Rev. Mod. Phys.* **77**, 1083.

de Groot, F. M. F. (2004). Multiplet effects in X-ray spectroscopy. *Coor. Chem. Rev.* **249, (1-2)**, 31.

De Teresa, J. M., M. R. Ibarra, P. A. Algarabel, C. Ritter *et al.* (1997). Evidence for magnetic polarons in the magnetoresistive perovskites. *Nature* **386**, 256.

Delugas, P., V. Fiorentini, A. Filippetti and G. Pourtois (2007). Cation charge anomalies and high-k dielectric behavior in $DyScO_3$: Ab initio density-functional and self-interaction-corrected calculations. *Phys. Rev. B* **75**, 115126.

Derks, C. (2008). *Electronic and magnetic properties of high k materials and multiferroics*. Diploma Thesis, Universität Osnabrück.

Devonshire, A. F. (1954). Theory of ferroelectrics. *Phil. Mag. Suppl.* **3**, 85.

Dong, C. L., C. Persson, L. Vayssieres, A. Augustsson *et al.* (2004). Electronic structure of nanostructured ZnO from x-ray absorption and emission spectroscopy and the local density approximation. *Phys. Rev. B* **70**, 195325.

Ederer, C. and N. A. Spaldin (2006). $BaNiF_4$: an electric field-switchable weak antiferromagnet. *Phys. Rev. B.* **74**, 1.

Einstein, A. (1905). Über einen die Erzeugung und Verwandlung des Lichtes betreffenden heuristischen Gesichtspunkt. *Annalen der Physik* **17**, 132.

Eisenbeiser, K., J. M. Finder, Z. Yu, J. Ramdani *et al.* (2000). Field effect transistors with $SrTiO_3$ gate dielectric on Si. *Appl. Phys. Lett.* **76**, 1324.

Endoh, Y., K. Hirota, S. Ishihara, S. Okamoto *et al.* (1999). Transition between Two Ferromagnetic States Driven by Orbital Ordering in $La_{0.88}Sr_{0.12}MnO_3$. *Phys. Rev. Lett* **82**, 4328.

Fadley, C. S. and D. A. Shirley (1970). Multiplet splitting of metal-atom electron binding energies. *Phys. Rev. A* **42**, 1109.

Fennie, C. J. and K. M. Rabe (2005). Ferroelectric transition in $YMnO_3$ from first principles. *Phys. Rev. B* **72**, 100103(R).

Fleming, R. M., D. V. Lang, C. D. W. Jones, M. L. Steigerwald *et al.* (2000). Defect dominated charge transport in amorphous Ta_2O_5 thin films. *J. Appl. Phys.* **88**, 850.

Fu, H. and R. E. Cohen (2000). Polarization rotation mechanism for ultrahigh electromechanical response in single-crystal piezoelectrics. *Nature (London)* **403**, 281.

Fujimori, A. and F. Minami (1984). Valence-band photoemission and optical absorption in nickel compounds. *Phys. Rev. B* **30**, 957.

Fujimori, A., F. Minami and S. Sugano (1984). Multielectron satellites and spin polarization in photoemission from Nicompounds. *Phys. Rev. B* **29**, 5225.

Gan, Q., R. A. Rao, C. B. Eom, J. L. Garrett *et al.* (1998). Direct measurement of strain effects on magnetic and electrical properties of epitaxial $SrRuO_3$ thin films. *Appl. Phys. Lett.* **72**, 978.

Gerken, F. (1983). Calculated photoemission spectra of the 4f states in the rare-earth metals. *J. Phys. F: Met. Phys.* **13**, 703.

Guirado-López, R. A., J. Dorantes-Dávila and G. M. Pastor (2003). Orbital Magnetism in Transition-Metal Clusters: From Hund's Rules to Bulk Quenching. *Phys. Rev. Lett.* **90, 22**, 226402.

Gusev, E. P., M. Copel, E. Cartier, I. J. R. Baumvol *et al.* (2000). High-resolution depth profiling in ultrathin Al_2O_3 films on Si. *Appl. Phys. Lett.* **76**, 176.

Haeni, J. H., P. Irvin, W. Chang, R. Uecker *et al.* (2004). Room-temperature ferroelectricity in strained $SrTiO_3$. *Nature (London)* **430**, 758.

Halilov, S. V., M. Fornari and D. J. Singh (2004). Lattice instabilities and ferroelectricity in $A ScO_3$ perovskite alloys. *Phys. Rev. B* **69**, 174107.

Hallwachs, W. (1888). Über den Einfluß des Lichtes auf elektrostatisch geladene Körper. *Wiedemannsche Annalen* **33**, 301.

Hamada, N., H. Sawada and K. Terakura (1995). Electronic band structure of $La_{1-x}Ba_xMnO_3$. *J. Phys. and Chem. of Solids* **56**, 1719.

Hedin, L. and B. L. Lundqvist (1971). Explicit local exchange-correlation potentials. *J. Phys. C: Solid State Phys.* **4**, 2064.

Hertz, H. (1887). Über den Einfluß des ultravioletten Lichtes auf die elektrische Entladung. *Wiedemannsche Annalen* **31**, 983.

Hill, N. A. (2000). Why Are There so Few Magnetic Ferroelectrics? *J. Phys. Chem. B* **104**, 6694.

Hohenberg, P. and W. Kohn (1964). Inhomogenous Electron Gas. *Phys. Rev.* **136**, B864.

Houssa, M., V. V. Afanas'ev, A. Stesmans and M. M. Heyns (2000). Variation in the fixed charge density of SiO_x/ZrO_2 gate dielectric stacks during postdeposition oxidation. *Appl. Phys. Lett.* **77**, 1885.

Huang, D. J., W. B. Wu, G. Y. Guo, H.-J. Lin *et al.* (2004). Orbital Ordering in $La_{0.5}Sr_{1.5}MnO_4$ Studied by Soft X-Ray LinearDichroism. *Phys. Rev. Lett* **92**, 087202.

Hubbard, J. (1963). Electron Correlations in narrow Energy Bands. *Proc. R. Soc. London, Ser. A* **276**, 238.

Hubbard, J. (1964a). Electron Correlations in narrow Energy Bands. 2. Degenerate Band Case. *Proc. R. Soc. London, Ser. A* **277**, 237.

Hubbard, J. (1964b). Electron Correlations in narrow Energy Bands. 3. Improved Solution. *Proc. R. Soc. London, Ser. A* **281**, 401.

Hüfner, S., P. Steiner, I. Sander, M. Neumann *et al.* (1991). Photoemission on NiO. *Z. Phys. B - Condensed Matter* **83**, 185.

Iida, J., M. Tanaka, Y. Nakagawa, S. Funahashi *et al.* (1993). Magnetization and Spin Correlation of Two-Dimensional Triangular Antiferromagnet $LuFe_2O_4$. *J. Phys. Soc. Jpn.* **62**, 1723.

Ikeda, N., K. Kohn, N. Myouga, E. Takahashi *et al.* (2000). Charge Frustration and Dielectric Dispersion in $LuFe_2O_4$. *J. Phys. Soc. Jpn.* **69**, 1526.

Ikeda, N., S. Mori and K. Kohn (2005a). Charge Ordering and Dielectric Dispersion in Mixed Valence Oxides RFe_2O_4. *Ferroelectrics* **314**, 41.

Ikeda, N., S. Mori and K. Yoshi (2007). Ferroelectricity from Valence Ordering in RFe_2O_4. *Ferroelectrics* **348**, 38.

Ikeda, N., H. Ohsumi, K. Ohwada, K. Ishii *et al.* (2005b). Ferroelectricity from iron valence ordering in the charge-frustrated system $LuFe_2O_4$. *Nature London* **436**, 1136.

Ikeda, N., Y. Yamada, S. Nohdo, T. Inami *et al.* (1998). Incommensurate charge ordering in mixed valence system $LuFe_2O_4$. *Physica B* **241-243**, 820.

Imada, M., A. Fujimori and Y. Tokura (1998). Metal-insulator transitions. *Rev. Mod. Phys.* **70**, 1039.

Isobe, M., N. Kimizuka, J. Iida and S. Takekawa (1990). Structures of $LuFeCoO_4$ and $LuFe_2O_4$. *Acta. Cryst. C* **46**, 1917.

Jablonski, A. (1993). Universal energy dependence of the inelastic mean free path. *Surface and Interface Analysis* **20**, 317.

Jia, J. J., T. A. Callcott, J. Yurkas, A. W. Ellis *et al.* (1995). First experimental results from IBM/TENN/TULANE/LLNL/LBL undulator beamline at the advanced light source. *Rev. Sci. Instrum.* **66**, 1394.

Jin, S., T. H. Tiefel, M. McCormack, R. A. Fastnacht *et al.* (1994). Thousandfold Change in Resistivity in Magnetoresistive La-Ca-Mn-O Films. *Science* **264**, 413.

Jones, R. O. and O. Gunnarsson (1989). The density functional formalism, its application and prospects. *Rev. Mod. Phys.* **61**, 681.

Kaindl, G., G. Kalkowski, W. D. Brewer, B. Perscheid *et al.* (1984). M-edge x-ray absorption spectroscopy of $4f$ instabilities in rare-earth systems. *J. Appl. Phys.* **55(6)**, 1910.

Kanamori, J. (1959). Superexchange Interaction and Symmetry Properties of Electron orbitals. *J. Phys. Chem. Solids* **10**, 87.

Kawano, H., R. Kajimoto and H. Yoshizawa (1996). Ferromagnetism-induced reentrant structural transition and phase diagram of the lightly doped insulator $La_{1-x}Sr_xMnO_3$ (x¡ 0.17). *Phys. Rev. B* **53**, R14709.

Khanra, S., K. Kuepper, T. Weyhermller, M. Prinz *et al.* (2008). Star-Shaped Molecule of $Mn_4^{II}O_6$ Core with an S_t=10 High-Spin State. A Theoretical and Experimental Study with XPS, XMCD, and Other Magnetic Methods. *Inorg. Chem.* **47, 11**, 4605.

Khomskii, D. I. and K. I. Kugel (2003). Elastic interactions and superstructures in manganites and other Jahn-Teller systems. *Phys. Rev. B* **67**, 134401.

Kim, K. H., D. B. Farmer, J.-S. M. Lehn, P. Venkateswara Rao *et al.* (2006). Atomic layer deposition of gadolinium scandate films with high dielectric constant and low leakage current. *Appl. Phys. Lett.* **89**, 133512.

Kimura, T., T. Goto, H. Shintani, K. Ishizaka *et al.* (2003). Magnetic control of ferroelectric polarization. *Nature* **426**, 55.

Kizilyalli, I. C., R. Y. S. Huang and P. K. Roy (1998). MOS transistors with stacked SiO_2-Ta_2O_5 -SiO_2 gate dielectrics for giga-scale integration of CMOS technologies. *IEEE Electron Device Lett.* **19**, 423.

Klein, T. M., D. Niu, W. S. Epling, W. Li *et al.* (1999). Evidence of aluminum silicate formation during chemical vapor deposition of amorphous Al_2O_3 thin films on Si(100). *Appl. Phys. Lett.* **75**, 4001.

Kohn, W. (1999). Nobel Lecture: Electronic structure of matter–wave functions and densityfunctionals. *Rev. Mod. Phys.* **71**(5), 1253.

Kohn, W. and L. J. Sham (1965). Self-Consistent Equations including Exchange and Correlation Effects. *Phys. Rev.* **140**, A1133.

Kolodzey, J., E. A. Chowdhury, G. Qui, J. Olowolafe *et al.* (1997). The effects of oxidation temperature on the capacitancevoltage characteristics of oxidized AlN films on Si. *Appl. Phys. Lett.* **71**, 3802.

Koopmans, T. (1933). Über die Zuordnung von Wellenfunktionen und Eigenwerten zu den einzelnen Elektronen eines Atoms. *Physica* **1**, 104.

Kotani, A. and S. Shin (2001). Resonant inelastic x-ray scattering spectra for electrons in solids. *Rev. Mod. Phys.* **73**, 203.

Kramers, H. A. (1929). The paramagnetic rotation of the plane of polarization in the uniaxial crystals of the rare earths. *Proc. Acad. Sc. (Amsterdam)* **32**, 1176.

Kramers, H. A. (1930). A general theory of paramagnetic rotation in crystals. *Proc. Acad. Sc. (Amsterdam)* **33**, 959.

Kramers, H. A. (1934). The interaction of magnetogenic atoms in paramagnetic crystals. *Physica* **1**, 182.

Kuepper, K., F. Bondino, K. C. Prince, M. Zangrando *et al.* (2005). Direct Investigation of Orbital Ordering in a colossal Magnetoresistance manganite by Means of X-ray Linear Dichroism at the Mn L Edge. *J. Phys. Chem. B* **109**, 15667.

Kuepper, K., A. V. Postnikov, A. Moewes, B. Schneider *et al.* (2004). The electronic structure of $KTaO_3$: a combined x-ray spectroscopic investigation. *J. Phys.: Condens. Matter* **16**, 8213.

Kuepper, K., B. Schneider, V. Caciuc, M. Neumann *et al.* (2003). Electronic structure of $Sn_2P_2S_6$. *Phys. Rev. B* **67**, 115101.

Kuriowa, Y., S. Aoyagi, J. Harada, E. Nishibori *et al.* (2001). Evidence for Pb-O Covalency in Tetragonal $PbTiO_3$. *Phys. Rev. Lett.* **87**, 217601.

Kužel, P., F. Kadlec, J. Petzelt, J. Schubert *et al.* (2007). Highly tuneable $SrTiO_3/DyScO_3$ heterostructures for applications in the terahertz range. *Appl. Phys. Lett.* **91**, 232911.

Kwo, J., M. Hong, A. R. Kortan, K. T. Queeney *et al.* (2000). High ϵ gate dielectrics Gd_2O_3 and Y_2O_3 for silicon. *Appl. Phys. Lett.* **77**, 130.

Lang, J. K., Y. Baer and P. A. Cox (1981). Study of the $4f$ and valence band density of states in rare-earth metals. II. Experiment and results. *J. Phys. F: Metal Phys.* **11**, 121.

Larson, A. C. and R. B. Von Dreele (1994). *GSAS: General Structural Analysis System*. LANSCE, Los Alamos National Laboratory, Los Alamos, NM.

Larson, P., W. R. L. Lambrecht, A. Chantis and M. van Schilfgaarde (2007). Electronic structure of rare-earth nitrides using the LSDA+U approach: Importance of allowing $4f$ orbitals to break the cubic crystal symmetry. *Phys. Rev. B* **75**, 045114.

Li, H.-F., Y. Su, Y. G. Xiao, J. Persson *et al.* (2009). Crystal and magnetic structure of single-crystal $La_{1-x}Sr_xMnO_3$ ($x \approx 1/8$). *Eur. Phys. J. B* **67**, 149.

Liferovich, R. P. and R. H. Mitchell (2004). A structural study of ternary lanthanide orthoscandate perovskites. *Journal of Solid State Chemistry France* **177**, 2188.

Lim, S.-G., S. Kriventsov, T. N. Jackson, J. H. Haeni *et al.* (2002). Dielectric functions and optical bandgaps of high-K dielectrics for metal-oxide-semiconductor field-effecttransistors by far ultraviolet spectroscopic ellipsometry. *J. Appl. Phys.* **91,7**, 4500.

Lo, S. H., D. A. Buchanan, Y. Taur and W. Wang (1997). Quantum-mechanical modeling of electron tunneling current from the inversion layer of ultra-thin-oxide nMOSFET's. *IEEE Electron Device Lett.* **18**, 209.

Lock, J. M. (1951). Penetration of magnetic fields into superconductors. III. Measurements on thin films of tin, lead and indium. *Proc. R. Soc. Lond. A* **208**, 391.

Lopes, J. M. J., M. Roeckerath, T. Heeg, E. Rije *et al.* (2006). Amorphous lanthanum lutetium oxide thin films as an alternative high-k gate dielectric. *Appl. Phys. Lett.* **89**, 222902.

Louca, D., T. Egami, E. L. Brosha, H. Roder *et al.* (1997). Local Jahn-Teller distortion in $La_{1-x}Sr_xMnO_3$ observed by pulsed neutron diffraction. *Phys. Rev. B* **56**, R8475.

Lucovsky, G., J. G. Hong, C. C. Fulton, Y. Zou *et al.* (2004). Spectroscopic studies of metal high-k dielectrics: transition metal oxides and silicates, and complex rare earth/transition metal oxides. *phys. stat. sol. B* **241**, 2221.

Lütkehoff, S. (1997). Untersuchungen zur elektronischen Struktur Seltener Erdoxide mittels Röntgenphotoelektronenspektroskopie. Ph.D. thesis, Universität Osnabrück.

Maekawa, S., T. Tohyama, S. E. Barnes, S. Ishihara *et al.* (2004). *Physics of Transition Metal Oxides*. Springer, Berlin.

Mannella, N., C. H. Booth, A. Rosenhahn, B. C. Sell *et al.* (2008). Temperature-dependent evolution of the electronic and local atomic structure in the cubic colossal magnetoresistive manganite $La_{1-x}Sr_xMnO_3$. *Phys. Rev. B* **77**, 125134.

Mathur, N. and P. Littlewood (2003). Mesoscopic texture in manganites. *Phys. Today* **56**, 25.

Matzdorf, R., A. Gerlach, A. Goldmann, M. Fluchtmann *et al.* (1999). A comparison of photoemission matrix elements in one-step calculations with experiment. *Surf. Sci.* **421**, 167.

McKee, R. A., F. J. Walker and M. F. Chisholm (1998). Crystalline Oxides on Silicon: The First Five Monolayers. *Phys. Rev. Lett.* **81**, 3014.

Meikeljohn, W. H. and C. P. Bean (1956). New Magnetic Anisotropy. *Phys. Rev.* **102**, 1413.

Michaelson, H. B. (1977). The work function of the elements and its periodicity. *J. Appl. Phys.* **48**, 4729.

Millis, A. J. (1998). Lattice effects in magnetoresistive manganese perovskites. *Nature* **392**, 147.

Millis, A. J., P. B. Littewood and B. I. Shraiman (1995). Double Exchange Alone Does Not Explain the Resistivity of $La_{1-x}Sr_xMnO_3$. *Phys. Rev. Lett.* **74**, 5144.

Millis, A. J., B. Shraiman and R. Müller (1996). Dynamic Jahn-Teller Effect and Colossal Magnetoresistance in $La_{1-x}Sr_xMnO_3$. *Phys. Rev. Lett.* **77**, 175.

Moewes, A., A. V. Postnikov, B. Schneider, E. Z. Kurmaev *et al.* (1999). Electronic structure of $KNbO_3$: Nb $M_{4,5}$ x-ray-fluorescence measurements. *Phys. Rev. B* **60**, 4422.

Moffit, W. and C. J. Ballhausen (1956). Quantum Theory. *Annu. Rev. Phys. Chem.* **7**, 107.

Moreo, A., S. Yunoki and E. Dagotto (1999). Phase Separation Scenario for Manganese Oxides and Related Materials. *Science* **283**, 2034.

Moritomo, Y., A. Asamitsu and Y. Tokura (1997). Enhanced electron-lattice coupling in $La_{1-x}Sr_xMnO_3$ near the metal-insulator phase boundary. *Phys. Rev. B* **56**, 12190.

Murakami, Y., J. P. Hill, D. Gibbs, M. Blume *et al.* (1998a). Resonant X-ray scattering from orbital ordering in $LaMnO_3$. *Phys. Rev. Lett* **81**, 582.

Murakami, Y., H. Kawada, H. Kawata, M. Tanaka *et al.* (1998b). Direct Observation of Charge and Orbital Ordering in $La_{0.5}Sr_{1.5}MnO_4$. *Phys. Rev. Lett* **80**, 1932.

Nagano, A., M. Naka, J. Nasu and S. Ishihara (2007). Electric Polarization, Magnetoelectric Effect, and Orbital State of a Layered Iron Oxide with Frustrated Geometry. *Phys. Rev. Lett.* **99**, 217202.

Nishioka, Y., H. Shinriki and K. Mukai (1987). Influence of SiO_2 at the Ta_2O_5/Si interface on dielectric characteristics of Ta_2O_5 capacitors. *J. Appl. Phys.* **61**, 2335.

Nix, W. D. (1989). Mechanical properties of thin films. *Metall. Trans. A* **20**, 2217.

Nix, W. D. and B. M. Clemens (1999). Crystallite coalescence: A mechanism for intrinsic tensile stresses in thin films. *J. Mater. Res.* **14**, 3467.

Okada, K., A. Kotani, B. T. Thole and G. A. Sawatzky (1991). Evidence of local singlet state in $NaCuO_2$ from Cu $2p$ X-ray photoemission and photoabsorption spectra. *Solid State Commun.* **77**, 835.

Okimoto, Y., T. Katsufuji, T. Ishikawa, T. Arima *et al.* (1997). Variation of electronic structure in $La_{1-x}Sr_xMnO_3$ ($0 leq x leq 0.3$) as investigated by optical conductivity spectra. *Phys. Rev. B* **55**, 4206.

Pabst, G. W., L. W. Martin, Y. H. Chu and R. Ramesh (2007). Leakage mechanisms in $BiFeO_3$ thin film. *Appl. Phys. Lett.* **90**, 072902.

Park, J. H., C. T. Chen, S. W. Cheong, W. Bao *et al.* (1996). Electronic Aspects of the Ferromagnetic Transition in Manganese Perovskites. *Phys. Rev. Lett.* **76**, 4215.

Park, J. H., E. Vescovo, H. J. Kim, C. Kwon *et al.* (1998). Direct evidence for a half-metallic ferromagnet. *Nature* **392**, 794.

Park, J. Y., J. H. Park, Y. K. Jeong and H. M. Jang (2007). Dynamic magnetoelectric coupling in electronic ferroelectric $LuFe_2O_4$. *Appl. Phys. Lett.* **91**, 152903.

Peatman, W. B. (1997). *Gratings, Mirrors and Slits: Beamline Design for Soft X-ray Synchrotron-RadiationSources*. Gordon and Reach Science Publishers, Amsterdam.

Perdew, J. P., K. Burke and M. Ernzerhof (1996). Generalized Gradient Approximation Made Simple. *Phys. Rev. Lett.* **77**(7), 3865.

Perdew, J. P., K. Burke and M. Ernzerhof (1997). Errata: Generalized Gradient Approximation Made Simple [Phys. Rev. Lett. 77, 3865 (1996)]. *Phys. Rev. Lett.* **78**(18), 1396.

Pertsev, N. A., A. G. Zembilgotov and A. K. Tagantsev (1998). Effect of mechanical boundary conditions on phase diagrams of epitaxial ferroelectric thin films. *Phys. Rev. Lett.* **80**, 1988.

Pickett, W. E. and J. S. Moodera (2001). Half metallic magnets. *Physics Today* **54**, 39.

Pinsard, L., J. Rodriguez-Carvajal, A. H. Moudden and A. Anane (1997). Jahn-Teller effect and ferromagnetic ordering in $La_{0.875}Sr_{0.125}MnO_3$: A reentrant behaviour. *Physica B* **234-236**, 856.

Plogmann, S. (1999). Untersucheungen der elektronischen und magnetischen Eigenschaften manganhaltiger Heusler Legierungen mittels Photoelektronen- und Röntgenspektroskopie. Ph.D. thesis, Universität Osnabrück.

Portengen, T., T. Östreich and L. J. Sham (1996). Theory of electronic ferroelectricity. *Phys. Rev. B* **54**, 17452.

Qin, Y. B., H. X. Yang, Y. Zhang, H. F. Tian *et al.* (2009). The effect of Mg doping on the structural and physical properties of $LuFe_2O_4$ and $Lu_2Fe_3O_7$. *J. Phys.: Condens. Matter* **21**, 015401.

Ravindran, P., A. Kjekshus, H. Fjellvåg, A. Delin *et al.* (2002). Ground-state and excited-state properties of $LaMnO_3$ from full-potentialcalculations. *Phys. Rev. B* **65**, 064445.

Robertson, J. (2006). High dielectric constant gate oxides for metal oxide Si transistors. *Rep. Prog. Phys.* **69**, 327.

Roy, P. K. and I. C. Kizilyalli (1998). Stacked high-ϵ gate dielectric for gigascale integration of metaloxidesemiconductor technologies. *Appl. Phys. Lett.* **72**, 2835.

Ruzmetov, D., Y. Seo, L. J. Belenky, D. M. Kim *et al.* (2005). Epitaxial Magnetic Perovskite Nanostructures. *Adv. Mater.* **17**, 2869.

Sághi-Szábo, G., R. E. Cohen and H. Krakauer (1998). First-principles study of piezoelectricity in $PbTiO_3$. *Phys. Rev. Lett.* **80**, 4321.

Saitoh, T., A. E. Bocquet, T. Mizokawa, H. Namatame *et al.* (1995). Electronic structure of $La_{1-x}Sr_xMnO_3$ studied by photoemission and x-ray-absorption spectroscopy. *Phys. Rev. B* **51**, 13942.

Salamon, M. B. and M. Jaime (2001). The physics of manganites: Structure and transport. *Rev. Mod. Phys.* **73**, 583.

Sangaletti, L., P. S. Bagus and F. Parmigiani (2000). Loss structures in the photoemission spectra of MnO: A careful analysis of peak intensities. *Phys. Rev. B* **62**, R7695.

Sangaletti, L., L. E. Depero, P. S. Bagus and F. Parmigiani (1995). A proper Anderson Hamiltonian treatment of the 3s photoelectron spectraof MnO, FeO, CoO and NiO. *Chem. Phys. Lett.* **245**, 463.

Sato, H. and M. Naito (1997). Increase in the superconducting transition temperature by anisotropic strain effect in (001) $La_{1.85}Sr_{0.15}CuO_4$ thin films on $LaSrAlO_4$ substrates. *Physica C* **274**, 221.

Schlachter, A. S. and F. J. Wuilleumier (1994). *New Directions in Research with Third-Generation Soft X-Ray Synchrotron Radiation Sources*. Kluwer, Netherlands.

Schlathölter, T. (1999). Theorie der spinpolarisierten Core-Level Spektroskopie für Photo- und Auger-Elektronen. Ph.D. thesis, Universität Osnabrück.

Schlom, D. G. and J. H. Haeni (2002). A thermodynamic approach to selecting alternative gate dielectrics. *MRS Bull.* **27**, 198.

Schubert, J., O. Trithaveesak, A. Petraru, C. L. Jia *et al.* (2003). Structural and optical properties of epitaxial $BaTiO_3$ thin films grown on $GdScO_3(110)$. *Appl. Phys. Lett.* **82**, 3460.

Schütz, G., W. Wagner, W. Wilhelm, P. Kienle *et al.* (1987). Absorption of circularly polarized x-rays in iron. *Phys. Rev. Lett.* **58**, 737.

Scofield, J. H. (1976). Hartree-Slater subshell photoionization cross-sections at 1254 and 1487 eV. *J. Electron. Spectr. Rel. Phenom.* **8**, 129.

Singh, D. J. (1994). *Planewaves, pseudopotentials and the LAPW method*. Kluwer Academic Publishers, Boston.

Siratori, K., S. Funahashi, J. Iida and M. Tanaka (1992). *Ferrites, Proc. 6th Int. Conf. on Ferrites Tokyo and Kyoto* 703.

Smolenskii, G. A. and I. E. Chupis (1982). Ferroelectromagnets. *Sov. Phys. Usp.* **25**, 475.

Speck, J. S., A. C. Daykin, A. Seifert, A. E. Romanov *et al.* (1995). Domain configurations due to multiple misfit relaxation mechanisms in epitaxial ferroelectric thin films. III. Interfacial defects and domain misorientations. *J. Appl. Phys.* **78**, 1696.

Stewart, G. R., J. A. Barclay and W. A. Steyert (1979). The specific heat of C-phase Gd_2O_3. *Sol. Stat. Comm.* **29**, 17.

Stöhr, J. and H. C. Siegmann (2006). *Magnetism: from Fundamentals to Nanoscale Dynamics*. Springer-Verlag Berlin Heidelberg.

Streiffer, S. K. t. (2002). Observation of nanoscale 180° stripe domains in ferroelectric $PbTiO_3$ thin films. *Phys. Rev. Lett* **89**, 067601.

Subramanian, M. A., T. He, J. Chen, N. S. Rogado *et al.* (2006). Giant RoomTemperature Magnetodielectric Response in the Electronic Ferroelectric $LuFe_2O_4$. *Adv. Mater.* **18**, 1737.

Sugihara, T., K. Siratori, I. Shindo and T. Katsura (1978). Effect of a Finite Amplitude Wave on Electrical Conductivity. *Phys. Soc. Jpn.* **45**, 1191.

Tanaka, M., H. Iwasaki, K. Siratori and I. Shindo (1989). Mössbauer Study on the Magnetic Stracture of $YbFe_2O_4$: A Two-Dimensional Antiferromagnet on a Triangular Lattice. *J. Phys. Soc. Jpn.* **58**, 1433.

Tanuma, S., C. J. Powell and D. R. Penn (1987). Proposed formula for electron inelastic mean free paths based on calculations for 31 materials. *Surface Science* **192**, L849.

Tebano, A., C. Aruta, S. Sanna, P. G. Medaglia *et al.* (2008). Evidence of Orbital Reconstruction at Interfaces in Ultrathin $La_{0.67}Sr_{0.33}MnO_3$ Films. *Phys. Rev. Lett.* **100**, 137401.

Teramura, Y., A. Tanaka and T. Jo (1996). Effect of Coulomb Interaction of the Y-Ray Magnetic Circular Dichroism Spin Sum Rule in 3*d* Transition Elements. *J. Phys. Soc. Jap.* **65, 4**, 1053.

Thole, B. T., P. Carra, F. Sette and G. van der Laan (1992). X-ray circular dichroism as a probe of orbital magnetization. *Phys. Rev. Lett.* **68**, 1943.

Thole, B. T., G. van der Laan, J. C. Fuggle, G. A. Sawatzky *et al.* (1985). 3*d* x-ray-absorption lines and the $3d^9f^{n+1}$ multiplets of lanthanides. *Phys. Rev. B* **32, 8**, 5107.

Thole, B. T., X. D. Wang, B. N. Harmon, D. Li *et al.* (1993). Multiplet fine structure in the photoemission of the gadolinium and terbium 5*p* levels. *Phys. Rev. B* **47**, 9098.

Uecker, R., B. Velickov, D. Klimm, R. Bertram *et al.* (2008). Properties of rare-earth scandate single crystals (Re=Nd-Dy). *J. Crystal Growth* **310**, 2649.

Uhlenbrock, S. (1994). *Untersuchungen zur elektronischen Struktur einfacher Übergangsmetall-Oxide –unter besonderer Berücksichtigung des NickelOxids*. PhD Thesis, Universität Osnabrück.

Urushibara, A., Y. Moritomt, T. Arima, A. Asamitsu *et al.* (1995). Insulator-metal transition and giant magnetoresistance in $La_{1-x}Sr_xMnO_3$. *Phys. Rev. B* **51**, 14103.

van Aken, B. B., O. D. Jurchescu, A. Meetsma, Y. Tomioka *et al.* (2003). Orbital-Order-Induced Metal-Insulator Transition in $La_{1-x}Ca_xMnO_3$. *Phys. Rev. Lett* **90**, 066403.

van Aken, B. B., T. T. M. Palstra, a. Filippetti and N. A. Spaldin (2004). The origin of ferroelectricity in magnetoelectric $YMnO_3$. *Nature mater.* **3**, 164.

van den Brink, J. and D. I. Khomskii (2008). Multiferroicity due to charge ordering. *J. Phys.: Condens. Matter* **20**, 434217.

van der Laan, G., M. Surman, M. A. Hoyland, C. J. F. Flipse *et al.* (1992). Resonant photoemssion at the Ni 2*p* edge core level as a probe of electroncorrelationeffects in nickel. *Phys. Rev. B* **46**, 9336.

van Dover, R. B. (1999). Amorphous lanthanide-doped TiO_x dielectric films. *Appl. Phys. Lett.* **74**, 3041.

van Vleck, J. H. (1932). Theory of the Variations in Paramagnetic Anisotropy Among Different Salts of the Iron Group. *Phys. Rev.* **41**, 208.

van Vleck, J. H. (1934). The Dirac Vector Model in Complex Spectra. *Phys. Rev.* **45**, 405.

Velickov, B., V. Kahlenberg, R. Bertram and M. Bernhagen (2007). Crystal chemistry of $GdScO_3$, $DyScO_3$, $SmScO_3$ and $NdScO_3$. *Z. Kristallogr.* **222**, 466.

Vijayanandhini, K. and T. R. N. Kutty (2008). Random existence of charge ordered stripes and its influence on the magnetotransport properties of $La_{0.6}Sr_{0.4}MnO_3$ perovskite substituted with diamagnetic ions at Mn sublattice. *J. Appl. Phys.* **103**, 093708.

von Barth, U. and L. Hedin (1972). A local exchange-correlation potential for the spin polarized case. *J. Phys. C: Solid State Phys.* **5**, 1629.

von Helmolt, R., J. Wecker, B. Holzapfel, L. Schultz *et al.* (1993). Giant negative magnetoresistance in perovskitelike $La_{2/3}Ba_{1/3}MnO_x$ ferromagnetic films. *Phys. Rev. Lett.* **71**, 2331.

Wagner, M., T. Heeg, J. Schubert, S. Lenk *et al.* (2006). Gadolinium scandate thin films as an alternative gate dielectric prepared by electron beam evaporation. *Appl. Phys. Lett.* **88**, 172901.

Wang, J., J. B. Neaton, H. Zheng, V. Nagarajan *et al.* (2003). Epitxial $BiFeO_3$ multiferroic thin film heterostructures. *Science* **299**, 1719.

Wilk, G. D., R. M. Wallace and J. M. Anthony (2001). High-k gate dielectrics: Current status and materials properties considerations. *J. Appl. Phys.* **89**, 5243.

Winiarski, A., T. Neumann, B. Mayer, G. Borstel *et al.* (1994). XPS Study of $KTaO_3$, $KTa_{0.69}Nb_{0.31}O_3$ and $KNbO_3$ Single Crystals. *phys. stat. sol. (b)* **183**, 475.

Xiang, H. J. and M.-H. Whangbo (2007). Charge Order and the Origin of Giant Magnetocapacitance in $LuFe_2O_4$. *Phys. Rev. Lett.* **98**, 846403.

Xiong, X., B. Dabrowski, O. Chmaissem, Z. Bukowski *et al.* (1999). Correlation between coherent Jahn-Teller distortion and magnetic spin orientation in $La_{1-x}Sr_xMnO_3$. *Phys. Rev. B* **60,14**, 10186.

Yamada, Y., S. Nohdo and N. Ikeda (1997). Incommensurate Charge Ordering in Charge-Frustrated $LuFe_2O_4$ System. *J. Phys. Soc. Jpn.* **66**, 3733.

Yeo, Y. C., T. J. King and C. Hu (2002). Direct tunneling leakage current and scalability of alternative gate dielectrics. *Appl. Phys. Lett.* **81**, 2091.

Youn, S. J. and B. I. Min (1997). Effects of doping and magnetic field on the half-metallic electronic structuresof$La_{1-x}Ba_xMnO_3$. *Phys. Rev. B* **56**, 12046.

Young, A. T., E. Arenholz, S. Marks, R. Schlueter *et al.* (2002). Variable linear polarization from an X-ray undulator. *Radiat.* **9**, 270.

Yu, Z., R. Droopad, J. Ramdani, J. A. Curless *et al.* (1999). Properties of Epitaxial $SrTiO_3$ Thin Films Grown on Silicon by Molecular Beam Epitaxy . *Mater. Res. Soc. Symp. Proc.* **567**, 427.

Yu, Z., J. Ramdani, J. A. Curless, J. M. Finder *et al.* (2000a). Epitaxial perovskite thin films grown on silicon by molecular beam epitaxy. *J. Vac. Sci. Technol. B* **18**, 1653.

Yu, Z., J. Ramdani, J. A. Curless, C. D. Overgaard *et al.* (2000b). Epitaxial oxide thin films on Si(001) . *J. Vac. Sci. Technol. B* **18**, 2139.

Zener, C. (1951). Interaction between the D-shells in the Transition Metals. 2. FerromagneticCompounds of Manganese with Perovskite Structure. *Phys. Rev.* **82**, 403.

Zhang, Y., H. X. Yang, C. Ma, H. F. Tian *et al.* (2007). Charge-Stripe Order in the Electronic Ferroelectric $LuGe_2O_4$. *Phys. Rev. Lett.* **98**, 247602.

Zhao, C., T. Witters, B. Brijs, H. Bender *et al.* (2005). Ternary rare-earth metal oxide higk-k layers on silicon oxide. *Applied Physics Letters* **86**, 132903.

Zhou, J.-S., J. B. Goodenough, A. Asamitsu and Y. Tokura (1997). Pressure-Induced Polaronic to Itinerant Electronic Transition in $La_{1-x}Sr_xMnO_3$ Crystals. *Phys. Rev. Lett.* **79**, 3234.

List of Publications

- M. Raekers, K. Kuepper, C. Taubitz, M. Prinz, C. Derks, A. Postnikov, S. J. Blundell, D. Prabakharan, S. George and M. Neumann *Investigation of the electronic structure of $LuFe_2O_4$ by means of XPS, XAS, XES, XMCD and calculations*, in preparation

- M. Raekers, K. Kuepper, C. Taubitz, M. Prinz, M. Uhlarz, F. M. F. de Groot, E. Ahrenholz, V. R. Galakhov, Ya. M. Mukovskii, and M. Neumann *Magnetism of $La_{1-x}Sr_xMnO_3$ by means of XMCD and magnetometry*, in preparation

- M. Prinz, K. Kuepper, C. Taubitz, M. Raekers, B. Biswas, T. Weyhermller, M. Uhlarz, J. Wosnitza, J. Schnack, A. V. Postnikov, C. Schröder, S. J. George, M. Neumann, and Phalguni Chaudhuri *A star-shaped heteronuclear $Cr^{III}Mn^{3}_{II}$ species and its precise electronic and magnetic structure: Spin frustration studied by X-ray spectroscopic, magnetic and theoretical methods*, in preparation

- C. Taubitz, K. Kuepper, M. Raekers, V. R. Galakhov, V. Felea, V. Tsurkan and M. Neumann *Reinvestigation of the Fe, Cu and Cr valences in (FeCu)Cr_2S_4 spinels* physica status solidi (b), pssb.200945057 (2009)

- M. Raekers, K. Kuepper, S. Bartkowski, M. Prinz, A. V. Postnikov, K. Potzger, S. Zhou, A. Arulraj, N. Stüßer, R. Uecker, W. L. Yang, and M. Neumann *Electronic and magnetic structure of $RScO_3$ (R = Sm, Gd, Dy) from x–ray spectroscopies and first–principles calculations* Phys. Rev. B 79, 125114 (2009)

- M. Prinz, M. Raekers, M. Neumann, K. Kuepper, S. Khanra, T. Weyhermuller and P. Chaudhuri *Synthesis, Structure, and Valency Verification of a $Mn^{III}_6O_2$–Cluster* Z. Phys. Chem. 223, 145-155 (2009)

- K. Kuepper, M. Raekers, C. Taubitz, H. Hesse, M. Neumann, A. T. Young, C. Piamonteze, F. Bondino and K. C. Prince *Fe valence state of Sr_2FeMoO_6 probed by x-ray absorption spectroscopy: The sample age matters* J. Appl. Phys. 104, 1 (2008)

- S. Khanra, K. Kuepper, T. Weyhermüller, M. Prinz, M. Raekers, S. Voget, A. V. Postnikov, F. M. F. de Groot, S. J. George, M. Coldea, M. Neumann, P. Chaudhuri *Star-Shaped Molecule of $Mn^{II}_4O_6$ Core with an S_t=10 High-Spin State. A Theoretical and Experimental Study with XPS, XMCD, and Other Magnetic Methods* J. Appl. Phys. 104, 1 (2008)

- V. R. Galakhov, M. A. Melkozerova, T. P. Chupakhina, G. V. Bazuev, M. Raekers, M. Neumann, S. L. Molodtsov *Valence states of 3d ions in lanthanum magneto-cobaltites determined by means of X-ray spectroscopy methods* Bulletin of Russian Academy of Science: Physics 72, 10, 1483-1485 (2008)

- R. Pacurariu, M. Coldea, M. Neumann, V. Pop, O. Isnard, M. Raekers *X-ray photoelectron spectroscopy and magnetism of* $MnPd_{1-x}Sb_x$ *alloys* phys. stat. sol. (b), 244, 9, 3190 (2007)

- V. R. Galakhov, O. B. Prokhorova, S. N. Shamin, A. S. Shkvarin, A. V. Korolyov, M. Raekers, M. Prinz, A. F. Takacs, M. Neumann, G. V. Bazuev, O. I. Gyrdasova, T. P. Chupakhina, Yu. S. Dedkov *X-ray spectra and spin states of manganese and cobalt ions in complex oxides* $La_{1-x}Ca_xMn_{0.5}Co_{0.5}O_3$ Phase transitions, ordered states and novel materials 2006.11.02. P.1-3

- V. R. Galakhov, N. A. Ovechkina, A. S. Shkvarin, S. N. Shamin, E. Z. Kurmaev, K. Kuepper, A. F. Takács, M. Raekers, S. Robin, M. Neumann, G.-N. Gavrilă, A. S. Semenova, D. G. Kellerman, T. Käämbre, and J. Nordgren *Electronic structure and x-ray spectra of defective oxides* Li_xCoO_2 Phys. Rev. B **74**, 045120(6) (2006)

- M. Raekers, K. Kuepper, H. Hesse, I. Balasz, I. G. Deac, S. Constantinescu, E. Burzo, M. Valeanu, and M. Neumann *Investigation of chemical and grain boundary effects in highly ordered* Sr_2FeMoO_6*: XPS and Mössbauer studies*, J. Opt. Ad. Mat., 8, 2, 455, (2006)

- V. R. Galakhov, A. S. Shkvarin, A. F. Takács, M. Raekers, M. Prinz, M. Neumann, A. V. Korolyev, G. V. Bazuev, O. I. Gyrdasova, T. I. Chupakhina, D. V. Vyalykh, Yu. S. Dedkov, and S. L. Molodtsov *Cobalt and manganese valence states in complex oxides* $La_{0.75}Ca_{0.25}Co_{0.5}Mn_{0.5}O_3$ BESSY – Annual Report 2005, 251–253

- V. R. Galakhov, A. S. Shkvarin, S. N. Shamin, K. Kuepper, A. F. Takács, M. Raekers, S. Robin, M. Neumann, G.-N. Gavrilă, A. S. Semenova, and D. G. Kellerman *Hole localization and phase separation in cobaltites* Li_xCoO_2*: X-ray absorption and photoelectron study* BESSY – Annual Report 2004, 129–131

Eidesstattliche Erklärung

Hiermit erkläre ich an Eides Statt, die vorliegende Abhandlung selbständig und ohne unerlaubte Hilfe verfasst, die benutzten Hilfsmittel vollständig angegeben und noch keinen Promotionsversuch unternommen zu haben.

Osnabrück, 09.04.2009
Michael Räkers